Low-Complexity Equalisation and Channel Estimation over Fast Fading Channels

by

Hongyang Zhang

Thesis submitted in fulfilment of the requirements for the degree of

Doctor of Philosophy

in

Engineering

under the supervision of

Prof. Xiaojing Huang

to

School of Electrical and Data Engineering
Faculty of Engineering and Information Technology
University of Technology Sydney
Broadway, NSW 2007, Australia

June 2022

Certificate of Original Authorship

I, Hongyang Zhang declare that this thesis, is submitted in fulfilment of the requirements for the award of Doctor of Philosophy, in the Faculty of Engineering and Information Technology at the University of Technology Sydney.

This thesis is wholly my own work unless otherwise referenced or acknowledged. In addition, I certify that all information sources and literature used are indicated in the thesis.

This document has not been submitted for qualifications at any other academic institution.

This research is supported by the Australian Government Research Training Program.

Signature: Production Note:
Signature removed prior to publication.

Date: 18/10/2022

ABSTRACT

The next generation wireless communication systems aim to achieve high capacity and low latency with high-mobility scenario as an important channel condition for various new applications. With the significantly increased data rate and Doppler frequency shift, the systems' ability to cope with fast channel variations is of significant importance. This thesis develops effective and efficient solutions to improve the performance of both conventional and emerging modulations over fast fading channels.

The recently proposed orthogonal time frequency space (OTFS) modulation shows outstanding performance over fast fading channels. However, existing research on OTFS is mostly focused on its delay-Doppler domain structure. In this thesis, channel and system models in different signal domains are firstly derived in both continuous and discrete forms, providing the basis for exploiting the full potential of OTFS with low complexity. Particularly, a circular stripe diagonal structure in the frequency-Doppler domain channel matrix for arbitrary multipath delays and Doppler shifts is identified through analyses and simulations, paving the way for low-complexity techniques to be adopted to combat fast channel fading.

Exploiting the circular stripe diagonal nature of the frequency-Doppler channel matrix, a low-complexity frequency-domain minimum mean-square-error (MMSE) equalisation for OTFS systems with long signal frames and fully resolvable Doppler spreads is then formulated. It is also demonstrated that the proposed MMSE equalisation is applicable to conventional modulations with short signal frames and partially resolvable Doppler spreads.

The diversity performance analyses for OTFS are further provided under both maximum likelihood and linear equalisations. Inspired by the frequency-domain precoding structure, an adaptive transmission scheme with frequency-domain precoding matrix composed of the eigenvectors of the channel matrix is proposed to improve the system performance under MMSE equalisation, and its optimised performance is derived with simple analytical expressions. Considering two extreme channel conditions, the lower and upper bounds for the diversity performance of the adaptive transmission scheme are also derived. The derived performance bounds can serve as performance benchmarks for OTFS and other precoded OFDM systems.

Based on the re-formulation of OTFS as precoded-OFDM, three variants of the original OTFS system for low-complexity channel estimation over fast fading channels are finally proposed in this thesis. They enable one-dimensional channel estimation and corresponding equalisation to be applied in either frequency or time domain. Simulation results demonstrate that the proposed frequency-domain pilot aided OTFS scheme is the most effective transmission technique for high-mobility wireless communications in terms of diversity performance, signalling overhead, and power efficiency.

ACKNOWLEDGMENTS

First of all, I would like to express my deepest gratitude to my supervisor Prof. Xiaojing Huang for his constant guidance and support. Along this journey, his kindness and sincerity keep warming and encouraging my life. Meanwhile, his patience, knowledge, and ingenuity show a remarkable example for my future work.

I would also like to thank my co-supervisor A/Prof. J. Andrew Zhang for his valuable suggestions and guidance. He is the man who always stands behind and is eager to help. I also want to thank Prof. Jay Guo for sharing experience and knowledge during my study.

I wish to extend my appreciation to excellent mentors and friends in GBDTC: Dr. Hao Zhang, Dr. Anh Tuyen Le, Dr. Yijiang Nan, Dr. Peiyuan Qin, Dr. Can Ding, Dr. Ting Zhang, Dr. Wei Lin, Dr. He Zhu, and Dr. Shulin Chen. Collaborating with them is the happiest and luckiest thing in my life.

Finally, I would like to show endless gratitude to my family: my father Shizhong Zhang, my mother Dexin Song, and my love Xinzhu Li. Their constant love, trust, accompany, and encouragement make it happen. I love you all!

Hongyang Zhang

June 2022

List of Publications

Journal Papers

J-1. **H. Zhang**, X. Huang and J. A. Zhang, "Adaptive Transmission With Frequency-Domain Precoding and Linear Equalization Over Fast Fading Channels," in IEEE Transactions on Wireless Communications, vol. 20, no. 11, pp. 7420-7430, Nov. 2021, doi: 10.1109/TWC.2021.3083652.

J-2. **H. Zhang**, X. Huang and J. A. Zhang, "Low-Overhead OTFS Transmission with Frequency or Time Domain Channel Estimation," submitted to IEEE Transactions on Wireless Communications.

J-3. **H. Zhang**, X. Huang and J. A. Zhang, "Low-Complexity Frequency Domain Equalization over Fast Fading Channels," submitted to IEEE Wireless Communications Letters.

Conference Papers

C-1. **H. Zhang**, X. Huang and J. A. Zhang, "Comparison of OTFS Diversity Performance over Slow and Fast Fading Channels," 2019 IEEE/CIC International Conference on Communications in China (ICCC), 2019, pp. 828-833, doi: 10.1109/ICCChina.2019.8855898.

C-2. **H. Zhang**, X. Huang, J. A. Zhang and Y. J. Guo, "Adaptive Transmission Based on MMSE Equalization over Fast Fading Channels," 2020 IEEE 92nd Vehicu-

lar Technology Conference (VTC2020-Fall), 2020, pp. 1-5, doi: 10.1109/VTC2020-Fall49728.2020.9348563.

C-3. **H. Zhang**, X. Huang and J. A. Zhang, "Frequency Domain Pilot-Aided Channel Estimation for OTFS over Fast Fading Channels," 2021 IEEE 94th Vehicular Technology Conference (VTC2021-Fall), 2021, pp. 1-5, doi: 10.1109/VTC2021-Fall52928.2021.9625551.

TABLE OF CONTENTS

Certificate of Original Authorship **i**

Abstract **iii**

Acknowledgments **v**

List of Publications **vii**

List of Figures **xiii**

List of Tables **xvii**

Abbreviations **xix**

Notations **xxiii**

List of Symbols **xxv**

1 Introduction **1**

1.1 Background 1

1.1.1 Use Cases for Next Generation Network 1

1.1.2 Challenges for Practical Applications 2

1.1.3 Affection of Fast Fading Channels 4

1.2 Challenges for Fast Fading Channels 4

1.3 Thesis Organisation 7

2 Analyses on Channel and System Models **9**

2.1 Introduction and Literature Review 9

2.2 Fast Fading Channel Representations 10

2.3 Signal Models in Time and Frequency Domains 12

2.3.1 Continuous Signal Models 13

2.3.2 Discrete Signal Models 14

2.4 Simulation Results 22

2.5 Conclusions 24

3 Low-Complexity Equalisation Techniques over Fast Fading Channels **27**

3.1 Introduction and Literature Review 27

3.1.1 Conventional Modulation over Fast Fading Channels 27

3.1.2 OTFS over Fast Fading Channels 28

3.1.3 Existing Equalisation Techniques of OTFS 28

3.1.4 Chapter Structure 30

3.2 Low-Complexity MMSE Equalisation 30

3.2.1 MMSE Equalisation with Fully Resolvable Doppler Spread 30

3.2.2 MMSE Equalisation with Partially Resolvable Doppler Spread . . 33

3.3 Equalisation Performance Analysis 35

3.3.1 Input-Output Relationships 35

3.3.2 Output SNR Analysis 37

3.4 Simulation Results 40

3.5 Conclusions 44

4 Adaptive Transmission with Frequency-Domain Precoding **47**

4.1 Introduction and Literature Review 47

4.1.1 Existing Diversity Study of OTFS 47

4.1.2 Chapter Structure 48

4.2 OTFS as Precoded OFDM 49
4.3 Diversity with ML Equalisation 52
4.4 Adaptive Transmission and BER Bounds 53
4.4.1 Adaptive Transmission 54
4.4.2 BER Bounds and Analysis 56
4.5 Simulation Results 59
4.5.1 Adaptive Transmission Performance and Comparison 59
4.5.2 BER Bound Validation 63
4.6 Conclusions 65

5 Low-Overhead OTFS Transmission with Frequency or Time Domain Channel Estimation 67

5.1 Introduction and Literature Review 67
5.1.1 Existing Channel Estimation techniques of OTFS 67
5.1.2 Chapter Structure 68
5.2 OTFS Variants and Channel Estimation 69
5.2.1 Frequency-Domain Pilot-Aided Scheme 69
5.2.2 Time-Domain Pilot-Aided Scheme 72
5.2.3 Time-Domain Training Sequence Scheme 75
5.3 Performance Analysis 77
5.3.1 MSE Analysis for FD-PA-OTFS 78
5.3.2 MSE Analysis for TD-PA-OTFS 79
5.3.3 MSE Analysis for TD-TS-OTFS 79
5.4 Simulation Results 81
5.5 Conclusions 85
5.6 Appendix 86

6 Conclusions and Future Work 89

6.1 Summary of Contributions 89
6.2 Future Work 91
6.2.1 Extension to MIMO Systems 92
6.2.2 Application in Joint Radar Communication (JRC) 92
6.2.3 Further System Complexity Reduction 93

Bibliography **95**

Appendix **113**

Appendix A 113
Appendix B 114

List of Figures

Figure **Page**

2.1 Relationships among different continuous channel representations. 12

2.2 Construction of delay-time domain channel matrix. 17

2.3 Construction of frequency-Doppler domain channel matrix. 19

2.4 An example demonstrating the process of forming the delay-time domain and frequency-Doppler domain channel matrices. 20

2.5 Relationships among channel matrices in different domains. 23

2.6 Power delay profiles of TDL-A (a) and TDL-D (b) channel models. 25

2.7 Frequency-time domain representation of fast fading channels. 25

2.8 Frequency-Doppler domain channel matrix over fast fading channels. 26

3.1 Comparison between long and short signal frames. 33

3.2 Performance comparison in LOS channel. 41

3.3 Performance comparison in NLOS channel. 42

3.4 BER versus velocity variation rate for detection with outdated CSI in LOS channel at SNR = 15 dB. 43

3.5 Performance comparison between MMSE and MP equalisations. 44

3.6 Performance comparison with LDPC coding. 45

4.1 Time domain transmitted signal frame of original OTFS system. 50

4.2 Frequency domain transmitted signal frame of OTFS as precoded OFDM form. 51

4.3 OTFS system block diagram in precoded OFDM form: (a) transmitter and (b) receiver. S/P and P/S stand for serial-to-parallel and parallel-to-serial conversions respectively, and CP stands for cyclic prefix. 52
4.4 Adaptive transmission system block diagram: transmitter (a) and receiver (b). 55
4.5 Comparison of various modulation schemes in LOS channels using 4-QAM. . 60
4.6 Comparison of various modulation schemes with and without channel estimation error in NLOS channels using 4-QAM. 61
4.7 Comparison of various modulation schemes with 16-QAM under both LOS and NLOS channels. 62
4.8 Lower bounds of MMSE equalisation performance under different multipath diversity orders without Doppler frequency shifts. The curves from right to left correspond to $P = 1,2,4,8,16,32,64,128,1024$, and asymptotic ∞. 64
4.9 Upper bounds of MMSE equalisation performance under different Doppler frequency diversity orders with $P = M \times N$. The curves from left to right correspond to $K_{\max} = 1,4,64$, and asymptotic ∞. 65
4.10 BER comparison under adaptive transmission when $K_{\max} = 1,4,16,64$ in high SNR region. 66

5.1 FD-PA-OTFS frequency-domain transmission frame construction with pilots. 70
5.2 FD-PA-OTFS channel estimation process. 71
5.3 Time-domain transmission frame constructions of (a) TD-PA-OTFS and (b) TD-TS-OTFS. 74
5.4 Channel estimation performance comparison among FD-PA-OTFS, TD-PA-OTFS and TD-TS-OTFS. 83
5.5 BER performance comparison among FD-PA-OTFS, TD-PA-OTFS and TD-TS-OTFS with estimated CSIs. 84
5.6 BER performance comparison between FD-PA-OTFS and original OTFS. . . . 85

5.7 BER performance of FD-PA-OTFS under different maximum speeds. 86

5.8 BER performance of TD-TS-OTFS under different maximum speeds. 87

1 Illustration of Gaussian elimination. 114

List of Tables

Table		Page
1	Signals, Channel Representations and System Parameters	xxiii
2	Signals, Channel Representations and System Parameters	xxv
3	Matrices and Vectors	xxvii
2.1	Simulation Parameters	24
5.1	Overhead of Different Transmission Schemes	82

Abbreviations

1G - first generation

2D - two-dimensional

3GPP - 3rd generation partnership project

4G - fourth generation

5G - fifth generation

6G - sixth generation

ADC - analog-to-digital converter

ADS - autonomous driving system

AR - augmented reality

AWGN - additive white Gaussian noise

BER - bit error rate

CDSC - continuous-Doppler-spread channel

CFO - carrier frequency offset

CP - cyclic prefix

CSI - channel state information

DAC - digital-to-analog converter

DFS - Doppler frequency shift

DFT - discrete Fourier transform

eMBB - enhanced mobile broadband

ETSI - European telecommunications standards institute

FBMC - filter bank multicarrier

FD-PA - frequency-domain pilot aided

FT - Fourier transform

Gbps - Gigabit per second

GFDM - generalized frequency division multiplexing

H2H - human to human

HD - high-definition

IAI - inter antenna interference

ICI - inter-carrier interference

IDFT - inverse discrete Fourier transform

IDI - inter Doppler interference

IFT - inverse Fourier transform

ISFFT - inverse symplectic finite Fourier transform

ISTNs - integrated space and terrestrial networks

JRC - joint radar communication

LDPC - low-density parity-check

LOS - line-of-sight

LTE - long term evolution

M2M - machine to machine

MAP - maximum A Posteriori probability

MCMC - Markov chain Monte Carlo

MIMO - multiple-input multiple-output

ML - maximum-likelihood

MLSE - maximum likelihood sequence estimation

MMSE - minimum mean square error

mMTC - massive machine type communication

mmWave - millimeter-wave

MP - message passing

MSE - mean-square-error

NLOS - non-line-of-sight

OFDM - orthogonal frequency division multiplexing

OTFS - orthogonal time frequency space

PA - power amplifiers

PAPR - peak to average power ratio

PDF - probability density function

QAM - quadrature amplitude modulation

RHS - right-hand-side

SC-FDE - single carrier frequency domain equalisation

SFFT - symplectic finite Fourier transform

SISO - single-input single-output

SNR - signal-to-noise ratio

TDL - tapped delay line

TD-PA - time-domain pilot aided

TD-TS - time-domain training sequence

TF - time-frequency

UAV - unmanned aerial vehicle

UMa - urban macrocell

uRLLC - ultra-reliable and low latency communication

V2V - vehicle-to-vehicle

VR - virtual reality

ZC - Zadoff Chu

ZF - zero forcing

NOTATIONS

Table 1: Signals, Channel Representations and System Parameters

Expressions	**Definitions**
Bold letters	Matrices and vectors signal
$(.)^{\mathbf{T}}$	Transpose operation
$(.)^{*}$	Conjugate operation
$(.)^{\mathbf{H}}$	Conjugate transpose operation
$\mathbf{X}_{m\times n}$	m by n matrix
$\mathbf{I}_{m}$	m by m identity matrix
$\mathbf{F}_{m}$	m-point normalised DFT matrix
$\mathbf{1}_{m\times n}$	m by n matrices with all 1 elements
$\mathbf{0}_{m\times n}$	m by n matrices with all 0 elements
$vec(\cdot)$	Vectorisation operation
$diag\{\mathbf{X}\}$	Extracting the diagonal elements from matrix $\mathbf{X}$
$diag\{\mathbf{x}\}$	Forming a diagonal matrix with vector $\mathbf{x}$
$\odot$	Hadamard product
$\otimes$	Kronecker product
$(\cdot)_{M}$	Modulo M operation
$\lceil\cdot\rceil$	Ceiling operation
$\lfloor\cdot\rfloor$	Flooring operation
$\mathbf{X}(i,:)$	i-th row of $\mathbf{X}$
$\mathbf{X}(:,j)$	j-th column of $\mathbf{X}$

List of Symbols

Table 2: Signals, Channel Representations and System Parameters

Symbols	**Definitions**
$s(t)$	Time domain continuous transmitted signal
$r(t)$	Time domain continuous received signal
$w(t)$	Time domain continuous noise
$S(f)$	Frequency domain continuous transmitted signal
$R(f)$	Frequency domain continuous received signal
$W(f)$	Frequency domain continuous noise
$s[i]$	Time domain discrete transmitted signal
$r[i]$	Time domain discrete received signal
$w[i]$	Time domain discrete noise
$S[i]$	Frequency domain discrete transmitted signal
$R[i]$	Frequency domain discrete received signal
$W[i]$	Frequency domain discrete noise
h_i, τ_i, and ν_i	The path gain, delay and Doppler shift of the i-th path in sparse P-path channel model
P	Number of multipaths in sparse P-path channel model.
τ	Delay
ν	Doppler frequency shift
t	Time variables
f	Frequency variables
$h(\tau,\nu)$	Continuous delay-Doppler channel representation
$h_t(\tau,t)$	Continuous delay-time channel representation
$H_\nu(f,\nu)$	Continuous frequency-Doppler channel representation
$H(f,t)$	Continuous time-frequency channel representation
M	Number of subcarriers
N	Number of OFDM/SC-FDE Symbols

Symbols	**Definitions**
M_1	Number of pilot sections in frequency domain for FD-PA-OTFS
N_1	Number of precoded data symbols in frequency domain in each pilot section for FD-PA-OTFS
M_2	Number of precoded data symbols in time domain in each pilot or training sequence section for TD-PA-OTFS or TD-TS-OTFS
N_2	Number of pilot or training sequence sections in time domain for TD-PA-OTFS or TD-TS-OTFS
d_r	Delay resolution
f_r	Doppler resolution
T	Duration of OFDM symbol
L	Length of channel impulse response
$L_{\max}$	Maximum number of resolvable multipaths
$K_{\max}$	Maximum number of resolvable Doppler frequency shifts
L_{cp}	Length of CP
T_{cp}	Duration of CP
σ_x^2	Time domain data symbol power
σ_s^2	Time domain signal power (the same as σ_x^2)
σ_w^2	Time domain noise power
σ_S^2	Frequency domain signal power
σ_W^2	Frequency domain noise power
γ_{in}	Input SNR before equalisation
γ_{out}	Output SNR after equalisation

Table 3: Matrices and Vectors

Symbols	**Definitions**	**Dimensions**
$\mathbf{r}$	Time domain received sequence	MN by 1
$\mathbf{s}$	Time domain transmitted sequence	MN by 1
$\mathbf{w}$	Time domain noise sequence	MN by 1
$\mathbf{H}_t$	Delay-time channel matrix	MN by MN
$\mathbf{R}$	Frequency domain received sequence	MN by 1
$\mathbf{S}$	Frequency domain transmitted sequence	MN by 1
$\mathbf{W}$	Frequency domain noise sequence	MN by 1
$\mathbf{H}_v$	Frequency-Doppler channel matrix	MN by MN
$\mathbf{h}$	Discrete version of $h(\tau, v)$	MN by MN
$\mathbf{H}$	Discrete version of $H(f, t)$	MN by MN
$\mathbf{h}_t$	Discrete version of $d_r h_t(\tau, t)$	MN by MN
$\mathbf{h}_v$	Discrete version of $f_r H_v(f, v)$	MN by MN
$\hat{\mathbf{s}}$	Estimate of $\mathbf{s}$	MN by 1
$\hat{\mathbf{S}}$	Estimate of $\mathbf{S}$	MN by 1
$\mathbf{G}_t$	Time domain MMSE matrix	MN by MN
$\mathbf{G}_v$	Frequency domain MMSE matrix	MN by MN
$\mathbf{X}$	Data symbol matrix for original OTFS	M by N
$\mathbf{x}$	Data symbol vector	MN by 1
$\mathbf{y}$	Received signal after MMSE equalisation	MN by 1
$\mathbf{X_1}$	Data symbol matrix for FD-PA-OTFS	M_1 by N_1
$\mathbf{X}_2$	Data symbol matrix for TD-PA-OTFS and TD-TS-OTFS	M_2 by N_2
$\mathbf{S}_{data}$	Precoded data matrix in frequency domain for FD-PA-OTFS	M_1 by N_1
$\mathbf{s}_{data}$	Precoded data matrix in time domain for TD-PA-OTFS and TD-TS-OTFS	M_2 by N_2

Symbols	**Definitions**	**Dimensions**
$\boldsymbol{\Theta}$	Frequency domain interpolation matrix	MN by N_1
$\boldsymbol{\Psi}$	Time domain interpolation matrix	N_2 by MN
$\boldsymbol{\Phi}$	Doppler domain phase shifting matrix	$L_{max}+1$ by MN
$\mathbf{E}$	Doppler domain phase shifting matrix composed of columns from $\boldsymbol{\Phi}$	$L_{max}+1$ by N_2
$\mathbf{z}$	ZC sequence	$L_{max}+1$ by 1
$\mathbf{q}$	Toeplitz-form matrix composed of ZC sequence	$L_{max}+1$ by $L_{max}+1$
$\mathbf{Q}$	Unitary matrix composed of eigenvectors of $\mathbf{H}_v^{\mathbf{H}}\mathbf{H}_v$	MN by MN
$\mathbb{Q}$	Diagonal matrix composed of rows from $\mathbf{q}$	$L_{max}+1$ by $(L_{max}+1)^2$
Λ	Diagonal matrix composed of eigenvalues of $\mathbf{H}_v^{\mathbf{H}}\mathbf{H}_v$	MN by MN
$\mathbf{V}$	Modulation matrix in general	Dimensions vary for different modulations

CHAPTER 1

INTRODUCTION

1.1 Background

1.1.1 Use Cases for Next Generation Network

From the first generation (1G) to the fourth generation (4G) mobile networks, different modulation technologies are adopted to support communications and applications with the data transfer speed increased from 2.4 Kbps to 100 Mbps [1–3]. Nowadays, the fifth generation (5G) systems have become reality and sixth generation (6G) concepts have been proposed to meet the demand for better quality, stability, higher data rate and low latency [4–8]. A future communication system is described as the one which can access and share data everywhere for everyone and everything at any time [9]. According to the 3rd Generation Partnership Project (3GPP), ultra-reliable and low latency communication (uRLLC), massive machine type communication (mMTC), enhanced mobile broadband (eMBB) are the major use cases in 5G [1, 10, 11] with eMBB mainly targeting the enhanced data rate and capacity in mobile networks, especially in moving vehicles and high-speed trains. eMBB applications include augmented reality (AR) and virtual reality (VR) for continuous and stable high-definition (HD) video streaming in

education, game, and even industry sectors [12]. They also include real-time information exchange in autonomous driving [13]. For example, the total operating mileage of the high speed railway (HSR) has already reached 29700 kilometres by 2015, but the widely used communication technology under HSR scenarios, such as GSM-R, can only support a low rate in order of kbps [14, 15]. Novel techniques is required to achieve a better balance between data rate and performance in high mobility. The uRLLC focuses on stability and low latency, which are significant for applications such as intelligent transportation, vehicle-to-vehicle (V2V) communication, remote manufacturing, and surgery. For a future V2V system, the millimetre-wave (mmWave) band is employed to ensure the data rate and network capacity [16]. The Doppler effect and high penetration loss at higher frequencies are extraordinary challenges in such high-mobility channels [17–19]. The mMTC is proposed for the evolution from human to human (H2H) communication to machine to machine (M2M) communication [1]. Higher connection density and wider coverage will be outstanding features in mMTC [20, 21]. It is seen that all of the above three use cases involve a critical scenario, high mobility channel. However, the ability to cope with the Doppler effect in high mobility channels is exactly the weakness of existing techniques.

1.1.2 Challenges for Practical Applications

With the development of radio detection and sensor technologies, one of the most popular application scenarios for 5G is the autonomous driving system (ADS) [22]. ADS can significantly alleviate traffic congestion through collision avoidance, route plan and driver assistance [23]. IEEE 802.11p has formally specified the spectrum and physical layer used in the vehicular environment, as well as significant changes from traditional channels in terms of symbol duration, bandwidth and Doppler shifts [24, 25]. Despite moving transmitters and receivers, there are more moving obstacles in V2V channels, making the channel estimation and signal recovery much more complex than those

in traditional channels. Besides the difference in channels, the data amount is also increasing. Currently, the number of sensors in an ADS vehicle is around 100, and this number could double in the near future [26]. To avoid the collision, a huge amount of collected data from sensors is exchanged rapidly among vehicles, demanding a data rate for ADS in the order of gigabit per second (Gbps) [27]. However, most of the current adopted standards, such as IEEE 802.11p/DSRC and ITS-G5/DSRC, can only support a maximum realistic data rate at about 6 Mbps [17, 27–29]. As such, the data rate and bandwidth of current common 4G wireless system have limited the development of ADS. Meanwhile, a real-time and stable network covering wider ranges is also an emerging challenge for existing systems.

Challenges mentioned in ADS also appear in other applications. Due to the limited coverage of fibre and base stations, more than 70% of the region on the planet is not covered by terrestrial networks, making it difficult to realise applications in 5G use cases [30]. In order to develop a massive-connected, high-speed, and low-latency network, integrated space and terrestrial networks (ISTNs) are proposed, providing wide coverage for people, machines, and vehicles from the land to the air and from the urban to the rural areas [31–33]. ISTNs will form a future communication ecology, involving space-based satellite networks, air-based aircraft networks, and ground-based mobile networks [34]. To achieve the purpose of connecting everything together, ISTNs are of significant importance. However, the Doppler frequency shift is an inevitable problem in ISTNs, as network topologies among satellites, aircrafts, and vehicles are time-varying due to changes of relative speeds and angles of communication platforms, which introduce large carrier frequency offset (CFO) to a receiver and form fast fading channels [35]. Previously introduced ADS can serve as a part of ISTNs, in which channel conditions experience fast fading. Therefore, the ability to cope with fast channel variation is critically important for ISTNs and other future communication systems.

1.1.3 Affection of Fast Fading Channels

With the ever increasing demands for data rate in next generation systems, the communication spectrum is shifting to higher frequency bands such as the mmWave band and the Doppler effect shows even greater disruption to the signal, especially for the most popular technique, orthogonal frequency division multiplexing (OFDM). The Doppler effect can destroy the special orthogonal carrier design of OFDM and cause inter-carrier interference (ICI) [36]. Meanwhile, OFDM also suffers from the high peak-to-average power ratio (PAPR) problem [37]. Some novel approaches such as the recently proposed orthogonal time frequency space (OTFS) modulation shows outstanding performance over fast fading channels, but its high-complexity equalisation and estimation techniques make it difficult to be applied in practice [38]. Therefore, it is of high urgency to develop low-complexity equalisation and estimation techniques for both existing and emerging modulations with improved resistance to fast fading channels.

1.2 Challenges for Fast Fading Channels

To achieve low-complexity estimation and equalisation over fast fading channels, there are some challenges that should be overcome due to the channel's time-varying characteristics.

- *Challenge 1:* **Doppler Frequency Shifts in Multipaths**

  In the conventional transmission systems and channel models, the carrier frequency is much lower than that in 5G and beyond 5G systems, and the motion of obstacles in multipaths are relatively slow. With a relatively short signal frame length, the channel during a frame can be regarded as static [39–41]. In this case, the Doppler frequency shift is mainly caused by the relative motion between the

transmitter and receiver. Simple channel estimation and equalisation techniques such as one-tap equalisers in OFDM-type systems can be applied to recover transmitted signals [42, 43]. However, in 5G cases, the frequency offset is more notable because of the changes in system parameters and Doppler frequency shifts caused by the motions of obstacles in propagation are greatly increasing [44]. As such, channel gains, time delays, and Doppler frequency shifts are all different in different paths, making it difficult to calculate and extract channel state information (CSI). It means that, besides the traditional delay dimension, the Doppler shift introduces another dimension to be solved, which greatly increases the complexity of signal detection. How to extract the complete CSI and recover the signal accurately is an inevitable challenge for all the communication systems over fast fading channels.

- *Challenge 2:* **Power Efficiency**

  Over the past decades, OFDM has played an important role in the communication systems for its advantages in the capacity of simple frequency-domain equalisation, whereas it is also well-known for the high peak to average power ratio (PAPR). Signals with large PAPR will seriously reduce the energy efficiency as the power amplifiers (PAs) have to be operated with larger power back-off [45, 46]. Meanwhile, high PAPR also raises a requirement for high-resolution data converters, such as analog-to-digital converter (ADC) and digital-to-analog converter (DAC) [37]. Since OFDM has been employed in the 5G systems for backward compatibility, it is necessary to solve the PAPR issue. To alleviate the in-band signal distortion and out-of-band radiation caused by high PAPR, many alternative approaches have been proposed, such as generalised frequency division multiplexing (GFDM), single carrier modulation, and filter bank multicarrier (FBMC) [47–49]. For example, the single carrier frequency domain equalisation (SC-FDE) utilises a single carrier

instead of the multiple carriers used in OFDM, allowing PA with a smaller linear range to be applied and reducing the peak power backoff [50, 51]. Benefited from similar reduced-complexity advantage and performance to those of OFDM, SC-FDE has been adopted for uplink multiple access schemes in the Long Term Evolution (LTE) of 3GPP [52].

- *Challenge 3:* **Diversity Performance**

  Existing work has demonstrated that the performance of OTFS is much better than that of OFDM in high mobility scenarios [38, 53]. However, the study on OTFS diversity performance and bit error rate (BER) bound is still very limited. The capability that an OTFS system can fully achieve both frequency and time diversity offered by fast fading channels is yet to be proven. With reduced-complexity equalisations, the realistic performance bounds of an OTFS system need also to be available for system design and benchmarking. OTFS is commonly interpreted as a two dimensional (2D) delay-Doppler domain modulation [53–55]. However, with rectangular pulse shaping, it can be also considered as a precoded multicarrier modulation. As such, conventional one dimensional (1D) time or frequency approach can be developed to facilitate fast fading channel estimation without compromise on diversity performance.

- *Challenge 4:* **System Complexity**

  With the data symbols in an OTFS system arranged in the delay-Doppler domain, the delay dimension contains the same number of data symbols as those in a comparable OFDM system and the Doppler dimension has to be large enough to ensure sufficient resolution for Doppler spread [38]. This signal structure makes the length of an OTFS transmission frame much longer than that of an OFDM system, significantly increasing the complexity of equalisation and estimation as well as processing delay. Moreover, most of the equalisation methods proposed

for OTFS are based on iterative algorithms, such as message passing (MP) and Markov chain Monte Carlo (MCMC) algorithm [53, 56]. Such equalisers are a heavy burden to the system and hence difficult to be applied in practice. The long frame length of OTFS also prevents some linear equalisations such as minimum mean square error (MMSE) equalisation from being applied due to the large size matrix inversion. Therefore, developing a low-complexity system which can achieve improved performance over fast fading channels is of significant importance for future high mobility wireless applications.

1.3 Thesis Organisation

This thesis is organised as follows.

Chapter 2 presents the channel and system models under high mobility scenarios. It starts with the channel representations among different 2D domains over fast fading channels, followed by the time and frequency domain system models in both continuous and discrete forms, allowing one-dimensional time and frequency equalisation and channel estimation techniques to be adopted in OTFS and other modulations. Especially, the concise frequency-domain structure inspires low-complexity equalisation and channel estimation methods in the following chapters. Finally, simulation results are provided to demonstrate the properties of channel matrices in different domains.

Chapter 3 presents a low-complexity frequency-domain equalisation method for OTFS and conventional modulations. It starts with the MMSE equalisation scheme for long frame modulations with fully resolvable Doppler spread such as OTFS followed by the scheme for short frame modulations with partially resolvable Doppler spread such as OFDM and SC-FDE. The theoretical output SNR and BER analyses for MMSE equalisation are then performed. Finally, simulation results are provided to demonstrate the efficiency and effectiveness of MMSE equalisation over fast fading channels for

various modulations.

Chapter 4 presents a study on the diversity performance of OTFS and proposes an adaptive transmission over fast fading channels. It starts with the matrix form representation of the OTFS system which is further reformulated as a precoded OFDM. Then, the theoretical diversity performance analyses are conducted assuming maximum likelihood equalisations. An adaptive transmission scheme is proposed to optimise the system performance with the knowledge of CSI. The BER lower bound and upper bound are also derived for the proposed adaptive transmission under two extreme channel conditions, taking into consideration of significantly large numbers of multipaths and Doppler frequency shifts. Finally, simulation results are provided to compare the performance between the adaptive transmission and conventional OTFS.

Chapter 5 presents multiple one-dimensional channel estimation techniques for low-overhead OTFS variants in both time and frequency domains. It starts with the frequency-domain pilot-aided scheme followed by the time-domain pilot-aided and training-sequence-aided schemes. The theoretical mean-square-error (MSE) analyses are then performed for all these variants. Finally, simulation results are provided to demonstrate the performance and overhead of the proposed channel estimation schemes in practical channel models.

Chapter 6 summarises the main contributions of this thesis and discusses some research directions for future work.

CHAPTER 2

ANALYSES ON CHANNEL AND SYSTEM MODELS

2.1 Introduction and Literature Review

The Doppler frequency shift (DFS) in channels can be addressed in two conditions in practice. The first condition is when the channel multipaths are assumed to be fixed and the relative motion only exists between the transmitter and receiver [57]. In this condition, if the channel information is accurately obtained from estimation, the received signal can be recovered by resampling, and then the system can be transformed into a pseudo-static channel [58]. For a multipath wireless communication system, all the paths share the same Doppler scaling factor in this channel [59, 60]. This treatment improves the performance significantly for point-to-point single carrier systems [61]. In another condition, the relative motion between transceivers is not the only source of time variation. There are other moving vehicles or trains existing as obstructions [62, 63]. Therefore, the DFS in every path differs from each other, which needs more complex channel estimation and equalisation strategy. With the increase in carrier frequency and data rate, the DFS in the second condition will be more serious and common in wireless systems.

With the deployment of high-speed trains, autonomous vehicles, and unmanned aerial vehicles (UAV), the high mobility scenario plays an important role in the 5G and future generation wireless communication systems [64]. According to the field tests in high mobility scenarios, the current existing 4G wireless communication system can only support a maximum data rate on the order of 2-4 Mbps, which is much lower than the requirements in 5G applications [65]. The most notable difference between high-mobility and conventional communication systems is the fast time-varying fading caused by the Doppler spread [66]. Since the speed variation at the receiver affects all CSI factors, the non-stationary properties of the fast fading channel raise a great challenge for accurate modelling of high mobility channels.

In this chapter, the channel model analysis over fast fading channels is first presented and then the continuous and discrete signal models between the transceivers are obtained in both time and frequency domains. The relationships among the channel representations in different domains are also disclosed in both continuous and discrete forms with proofs. The analyses in this chapter are fundamental for low-complexity equalisations and channel estimations in the following chapters. Finally, the simulation presented verifies the characteristics of the fast fading channel based on practical channel models.

2.2 Fast Fading Channel Representations

Regardless of specific modulation or demodulation process, various existing representations of the fast fading channel are first revisited considering a single-input single-output (SISO) system. The analyses are all performed on baseband signals. Assuming that the continuous signal waveform transmitted over the channel is $s(t)$, the received signal can be modelled as

$$r(t) = \int_{-\infty}^{+\infty} \int_{-\infty}^{+\infty} h(\tau, \nu) s(t-\tau) e^{\mathbf{j}2\pi\nu t} d\tau d\nu + w(t), \tag{2.1}$$

where $h(\tau,\nu)$ is called the *delay-Doppler spreading function*, $\mathbf{j}=\sqrt{-1}$ and $w(t)$ is the additive white Gaussian noise (AWGN). For a sparse P-path channel, $h(\tau,\nu)$ is defined as

$$h(\tau,\nu)=\sum_{i=1}^{P}h_i\delta(\tau-\tau_i)\delta(\nu-\nu_i), \tag{2.2}$$

where h_i, τ_i, and ν_i are the path gain, delay and Doppler shift of the i-th path, respectively, and $\delta(\cdot)$ denotes the Dirac delta function satisfying

$$\int_{-\infty}^{+\infty}\delta(x)dx=1. \tag{2.3}$$

In addition to the *delay-Doppler* representation, the fast fading channel can also be expressed in different domains. Applying the inverse Fourier transform (IFT) to $h(\tau,\nu)$ with respect to the Doppler frequency ν, the *delay-time* representation is obtained as

$$h_t(\tau,t)=\int_{-\infty}^{+\infty}h(\tau,\nu)e^{\mathbf{j}2\pi\nu t}d\nu. \tag{2.4}$$

Similarly, applying Fourier transform (FT) to $h(\tau,\nu)$ with respect to the delay τ, we obtain the *frequency-Doppler* representation as

$$H_\nu(f,\nu)=\int_{-\infty}^{+\infty}h(\tau,\nu)e^{-\mathbf{j}2\pi f\tau}d\tau. \tag{2.5}$$

Applying both IFT and FT to $h(\tau,\nu)$ with respect to ν and τ respectively, the *frequency-time* representation, also called time-frequency (TF) transfer function, is obtained as

$$H(f,t)=\int_{-\infty}^{+\infty}\int_{-\infty}^{+\infty}h(\tau,\nu)e^{\mathbf{j}2\pi\nu t}e^{-\mathbf{j}2\pi f\tau}d\tau d\nu. \tag{2.6}$$

The relationship between $h_t(\tau,t)$ and $H_\nu(f,\nu)$ can be expressed as

$$H_\nu(f,\nu)=\int_{-\infty}^{+\infty}\int_{-\infty}^{+\infty}h_t(\tau,t)e^{-\mathbf{j}2\pi f\tau}e^{-\mathbf{j}2\pi\nu t}d\tau dt. \tag{2.7}$$

It is seen that $H_\nu(f,\nu)$ is the 2D FT of $h_t(\tau,t)$. Fig. 2.1 shows the relationships among the various fast fading channel representations, which characterise the same fast fading channel in different ways.

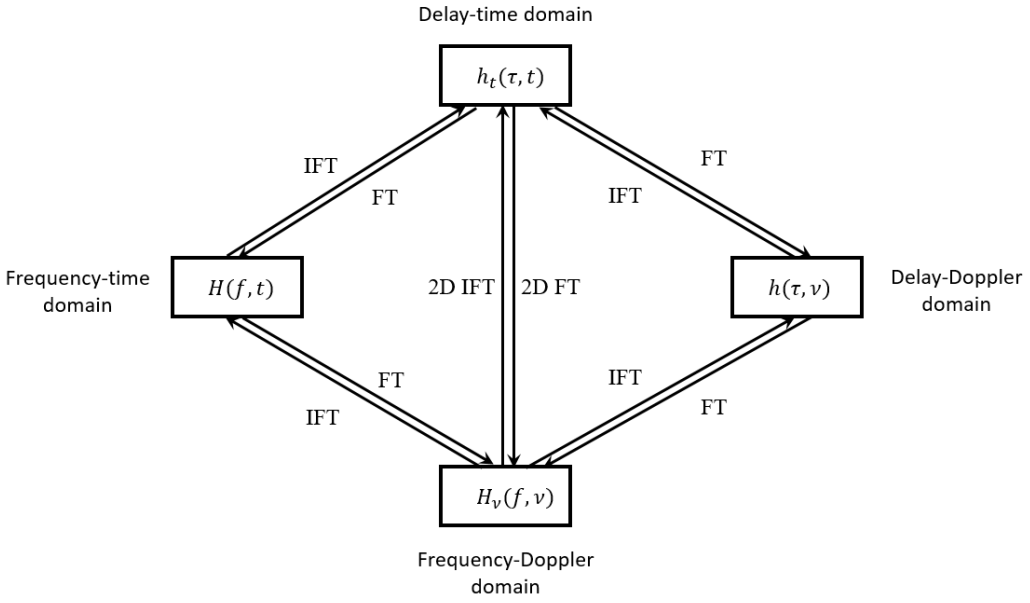

Figure 2.1: Relationships among different continuous channel representations.

Note that the signal model adopted in most of existing studies on OTFS systems, e.g., [53, 67, 68] is presented in the time domain with the following form

$$\begin{aligned} r(t) &= \int_{-\infty}^{+\infty}\int_{-\infty}^{+\infty} h(\tau,\nu)s(t-\tau)e^{\mathbf{j}2\pi\nu(t-\tau)}d\tau d\nu + w(t) \\ &= \int_{-\infty}^{+\infty}\int_{-\infty}^{+\infty} h'(\tau,\nu)s(t-\tau)e^{\mathbf{j}2\pi\nu t}d\tau d\nu + w(t), \end{aligned} \tag{2.8}$$

where $h'(\tau,\nu) = h(\tau,\nu)e^{-\mathbf{j}2\pi\nu\tau}$.

With this model, the relationships illustrated in Fig. 2.1 are no longer valid since the phase term $e^{-\mathbf{j}2\pi\nu\tau}$ is imposed on the delay-Doppler spreading function. As a result, the previous studies on OTFS seldom consider frequency-domain analysis [54–56, 67–71].

2.3 Signal Models in Time and Frequency Domains

In this section, continuous and discrete signal models are derived in both time and frequency domains respectively and the relationships among them are obtained. Note that a cyclic prefix (CP) or zero-padded suffix with length longer than the maximum

multipath delay is inserted in any OTFS frame. This converts the linear convolution between the transmitted signal and the channel to a circular convolution.

2.3.1 Continuous Signal Models

With the delay-time domain and frequency-Doppler domain representations of the fast fading channel, the continuous received signal models can be derived in time domain and frequency domain respectively. Substituting (2.4) into (2.1) and letting $\tau' = t - \tau$, it can be obtained as

$$r(t) = \int_{-\infty}^{+\infty} h_t(t-\tau', t)s(\tau')d\tau' + w(t), \tag{2.9}$$

which is the time domain received signal model over the considered fast fading channel. It is seen that the time domain received signal is a convolution of the time domain transmitted signal with the time-varying impulse response $h_t(\tau, t)$ in terms of delay τ.

On the other hand, representing the transmitted signal in the frequency domain as $S(f)$ and substituting it into (2.1), it can be obtained as

$$\begin{aligned} r(t) &= \int_{-\infty}^{+\infty}\int_{-\infty}^{+\infty}\int_{-\infty}^{+\infty} h(\tau,\nu)S(f)e^{\mathbf{j}2\pi f(t-\tau)}e^{\mathbf{j}2\pi\nu t}d\tau d\nu df + w(t) \\ &= \int_{-\infty}^{+\infty}\int_{-\infty}^{+\infty} h_t(\tau,t)S(f)e^{\mathbf{j}2\pi f(t-\tau)}d\tau df + w(t) \\ &= \int_{-\infty}^{+\infty} H(f,t)S(f)e^{\mathbf{j}2\pi f t}df + w(t). \end{aligned} \tag{2.10}$$

Applying FT to $r(t)$, the frequency domain received signal can be modelled as

$$\begin{aligned} R(f) &= \int_{-\infty}^{+\infty} r(t)e^{-\mathbf{j}2\pi f t}dt + W(f) \\ &= \int_{-\infty}^{+\infty}\int_{-\infty}^{+\infty} H(f',t)e^{-\mathbf{j}2\pi(f-f')t}dtS(f')df' + W(f) \\ &= \int_{-\infty}^{+\infty} H_\nu(f', f-f')S(f')df' + W(f), \end{aligned} \tag{2.11}$$

where $W(f)$ is the AWGN in the frequency domain. The channel frequency response at Doppler frequency ν, $H_\nu(f,\nu)$, can also be interpreted as a frequency-dependent Doppler

response. It is seen that the frequency domain received signal is a convolution of the frequency domain transmitted signal with the frequency-dependent Doppler response in terms of Doppler frequency ν.

The time-varying impulse response and frequency-dependent Doppler response of the fast fading channel can be used to fully describe the input-output relationships of the fast fading channel in time domain and frequency domains, respectively. To further explore their connection in addition to (2.7), let $\nu = f' - f$ and rewrite Eq. (2.7) as

$$\begin{aligned} H_\nu(f, f'-f) &= \int_{-\infty}^{+\infty}\int_{-\infty}^{+\infty} h_t(\tau,t) e^{-\mathbf{j}2\pi f\tau} e^{-\mathbf{j}2\pi(f'-f)t} d\tau dt \\ &= \int_{-\infty}^{+\infty}\int_{-\infty}^{+\infty} h_t(\tau,t) e^{\mathbf{j}2\pi f(t-\tau)} e^{-\mathbf{j}2\pi f' t} d\tau dt. \end{aligned} \tag{2.12}$$

Substituting $t-\tau$ with a new variable τ', $\tau = t - \tau'$ and hence $d\tau = -d\tau'$ at any given t. Then, Eq. (2.12) is further expressed as

$$H_\nu(f, f'-f) = \int_{-\infty}^{+\infty}\int_{-\infty}^{+\infty} h_t(t-\tau',t) e^{\mathbf{j}2\pi f\tau'} e^{-\mathbf{j}2\pi f' t} d\tau' dt. \tag{2.13}$$

Finally, interchanging the variables f and f', we have

$$H_\nu(f', f-f') = \int_{-\infty}^{+\infty}\int_{-\infty}^{+\infty} h_t(t-\tau',t) e^{\mathbf{j}2\pi f'\tau'} e^{-\mathbf{j}2\pi f t} d\tau' dt. \tag{2.14}$$

It suggests that given the delay-time and frequency-Doppler representations of a fast fading channel, $h_t(\tau,t)$ and $H_\nu(f,\nu)$, its time-varying impulse response can be expressed as $h_t(t-\tau',t)$, where the delay is defined as $\tau = t - \tau'$ referenced at time τ'. Meanwhile, its frequency-Doppler response can be expressed as $H_\nu(f', f-f')$, where the Doppler frequency is defined as $\nu = f - f'$ referenced at frequency f'. $H_\nu(f', f-f')$ is the IFT and FT of $h_t(t-\tau',t)$ in terms of τ' and t, respectively.

2.3.2 Discrete Signal Models

It is assumed that the discrete-time transmitted signal $s[i]$ is a sequence of sampled continuous time signal $s(id_r)$ where d_r denotes the sampling period which is also termed

as the delay resolution. Further assume that the maximum channel multipath delay is $d_{\max}$ and the maximum Doppler frequency is $f_{\max}$. Hence, the maximum number of resolvable multipaths is $L_{\max} = \lceil d_{\max}/d_r \rceil$, where $\lceil \cdot \rceil$ denotes the ceiling function that obtains the rounded up number, provided that the channel has a minimum bandwidth $1/d_r$, and the maximum number of resolvable Doppler frequencies (positive or negative side) is $K_{\max} = \lceil f_{\max}/f_r \rceil$, where f_r is the *Doppler resolution*. Assuming that MN is the total number of samples in a frame, f_r equals to $1/(MNd_r)$.

Under the above assumptions and according to Eq. (2.9), the discrete delay-time representation of the fast fading channel can be obtained as

$$\begin{aligned} h_t[i,j] = h_t(id_r, jd_r) &= \int_{-1/2d_r}^{1/2d_r} H(f, jd_r) e^{\mathbf{j}2\pi f i d_r} df \\ &= \frac{1}{d_r} \sum_{l=1}^{P} h_l e^{\mathbf{j}2\pi \nu_l d_r j} \mathrm{sinc}(i - \frac{\tau_l}{d_r}), \end{aligned} \tag{2.15}$$

where $\mathrm{sinc}(x) = \frac{sin(\pi x)}{\pi x}$ is the normalised sinc function. In deriving (2.15), the sparse P-path channel expressed in Eq. (2.2) is assumed and its TF transfer function can be expressed as

$$H(f,t) = \sum_{i=1}^{P} h_i e^{-\mathbf{j}2\pi f \tau_i} e^{\mathbf{j}2\pi \nu_i t}. \tag{2.16}$$

The discrete received signal sequence, the transmitted signal sequence, and the noise sequence can be denoted as vectors $\mathbf{r} = [r[0], r[1], ..., r[MN-1]]^T$, $\mathbf{s} = [s[0], s[1], ..., s[MN-1]]^T$, and $\mathbf{w} = [w[0], w[1], ..., w[MN-1]]^T$ respectively, where $r[i] \triangleq r(id_r)$, $s[i] \triangleq s(id_r)$, and $w[i] \triangleq w(id_r)$ for $i = 0, 1, ..., MN-1$. With the use of CP, we have $s[-i] = s[MN-i]$, $i = 1, 2, ..., L_{cp}$, where L_{cp} is the number of samples in a CP. Equivalently, assuming a periodical extension of $h_t(\tau, t)$ from (2.9), the discrete time domain received signal model can be expressed as

$$r[i] = d_r \sum_{j=0}^{MN-1} h_t((i-j)d_r, id_r) s[j] + w[i], \tag{2.17}$$

which is equivalent to a circular convolution of $h_t[i,j]$ with $s[j]$ with respect to the delay index j multiplied by a scaling factor d_r plus $w[i]$.

From Eq. (2.17), the discrete time domain received signal model can be expressed in the matrix form as

$$\mathbf{r} = \mathbf{H}_t \mathbf{s} + \mathbf{w}, \tag{2.18}$$

where $\mathbf{H}_t$ is the delay-time channel matrix and defined as

$$\mathbf{H}_t = d_r \begin{bmatrix} h_t[0,0] & h_t[MN-1,0] & \cdots & h_t[1,0] \\ h_t[1,1] & h_t[0,1] & \cdots & h_t[2,1] \\ \vdots & \vdots & \ddots & \vdots \\ h_t[MN-1,MN-1] & h_t[MN-2,MN-1] & \cdots & h_t[0,MN-1] \end{bmatrix}. \tag{2.19}$$

With the use of CP, the above delay-time domain channel matrix is constructed from a periodically extended $h_t(\tau,t)$ as illustrated in Fig. 2.2, where the shaded squares with different grey levels indicate different discrete values of $h_t[i,j]$. It is seen that the coordinate transformation $\tau = t - \tau'$ maps the parallelogram enclosed by the dashed lines in τ-t coordinates onto a squared area in the t-τ' coordinates. It is also interesting to see that when the channel is time-invariant, $\mathbf{H}_t$ becomes a circulant matrix composed of the channel's impulse response.

Note that, different to conventional models, the delay-time domain channel matrix $\mathbf{H}_t$ can be constructed for any multipath delay τ_i and Doppler shift ν_i through the TF transfer function as shown in Eqs. (2.15) and (2.16). Referring to the conventional discrete-time domain signal model used in most of the recent works [53, 56, 68], an effective channel matrix can be constructed as a product of many permutation matrices (representing the circular shifts of input signal samples) and phase-only diagonal matrices (representing the Doppler shifts) [55]. Though the effective channel matrix demonstrates some sparsity, it is channel-dependent and lacks the explicit time-varying convolution nature. In addition, such effective channel matrix is only valid for on-grid multipath delays and Doppler shifts.

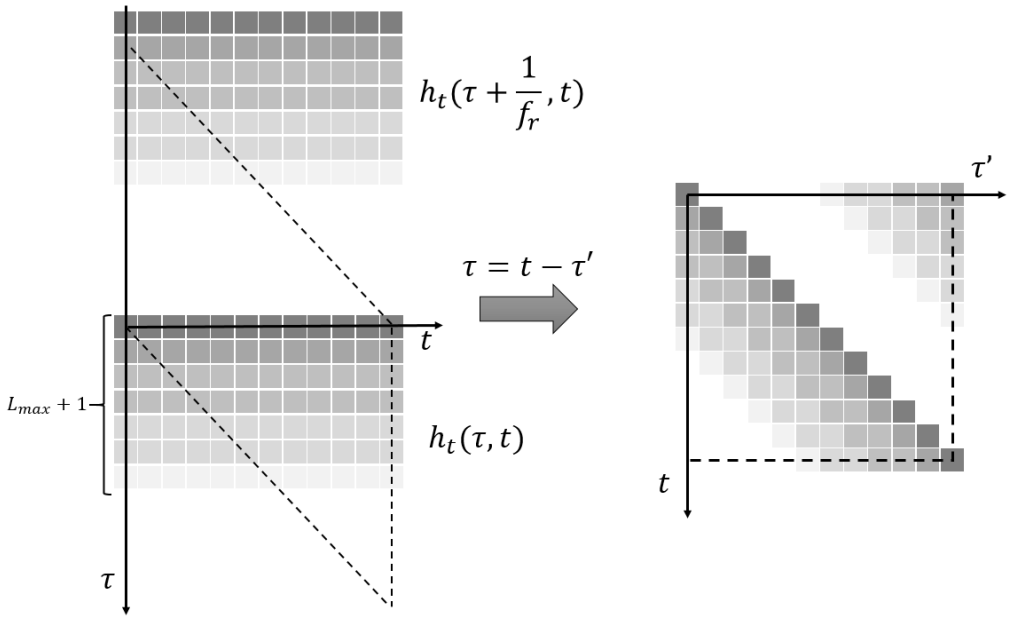

Figure 2.2: Construction of delay-time domain channel matrix.

On the other hand, the discrete frequency-Doppler representation of the fast fading channel is linked to the TF transfer function as

$$\begin{aligned} H_v[i,j] = H_v(if_r, jf_r) &= \int_0^{1/f_r} H(if_r, t) e^{-\mathbf{j}2\pi j f_r t} dt \\ &= \frac{1}{f_r} \sum_{l=1}^{P} h_l e^{-\mathbf{j}2\pi\tau_l f_r i} e^{-\mathbf{j}\pi(j-\frac{\nu_l}{f_r})} \mathrm{sinc}(j - \frac{\nu_l}{fr}), \end{aligned} \tag{2.20}$$

for $-\frac{MN}{2} \le i, j \le \frac{MN}{2} - 1$.

Note that it has been assumed that the frequency representation H_v is band-limited. It is known that the discrete spectrum repeats at the sampling frequency when a time-domain continuous signal is sampled and discretised. Therefore, the discrete version of $H_v(f, v)$ becomes a periodic function in the discrete frequency domain with the period of $1/d_r$. Accordingly, the discrete frequency-Doppler representation of the fast fading channel is defined as one period of discretised $H_v(f, v)$. In this way, $H_v[i, j]$ can be periodically extended as one period of $H_v(f, v)$ with all positive indices i and j, which is equivalent to circularly shifting the function values defined in (2.20) from $[-\frac{MN}{2}, -1]$ to $[\frac{MN}{2}, MN - 1]$.

The discrete frequency domain received signal model can then be expressed as

$$R[i] = f_r \sum_{j=0}^{MN-1} H_v(if_r,(j-i)f_r)S[j] + W[i], \tag{2.21}$$

which is equivalent to a generalised circular convolution of $H_v[j,i]$ with $S[j]$ with respect to the Doppler index j multiplied by a scaling factor f_r plus $W[i]$.

With all positive indices, the discrete frequency domain received signal sequence, the transmitted signal sequence, and the noise sequence can be denoted as vectors $\mathbf{R} = [R[0],R[1],...,R[MN-1]]^T$, $\mathbf{S} = [S[0],S[1],...,S[MN-1]]^T$, and $\mathbf{W} = [W[0],W[1],...,W[MN-1]]^T$. It is easy to see that $\mathbf{R}$, $\mathbf{S}$ and $\mathbf{W}$ are the discrete Fourier transform (DFT) of $\mathbf{r}$, $\mathbf{s}$ and $\mathbf{w}$, respectively.

From (2.21), the discrete frequency domain received signal model can be expressed in the matrix form as

$$\mathbf{R} = \mathbf{H}_v\mathbf{S} + \mathbf{W}, \tag{2.22}$$

where $\mathbf{W}$ denotes the frequency domain noise vector and $\mathbf{H}_v$ is the frequency-Doppler channel matrix defined as

$$\mathbf{H}_v = f_r \begin{bmatrix} H_v[0,0] & H_v[1,MN-1] & \cdots & H_v[MN-1,1] \\ H_v[0,1] & H_v[1,0] & \cdots & H_v[MN-1,2] \\ \vdots & \vdots & \ddots & \vdots \\ H_v[0,MN-1] & H_v[1,MN-2] & \cdots & H_v[MN-1,0] \end{bmatrix}. \tag{2.23}$$

The frequency-Doppler channel matrix $\mathbf{H}_v$ can also be regarded as being constructed from a periodically extended $H_v(f,v)$ as illustrated in Fig. 2.3, where the shaded squares with different gray levels indicate different discrete values of $H_v[i,j]$. It is also seen that the coordinate transformation $v = f - f'$ maps the parallelogram enclosed by the dashed lines in v-f' coordinates onto a squared area in f-f' coordinates.

To better understand the constructions of the above two channel matrices, a simple channel delay-Doppler spreading function $h(\tau,v)$, its associated channel delay-time representation $h_t(\tau,t)$ and frequency-Doppler representation $H_v(f,v)$ are shown in Fig.

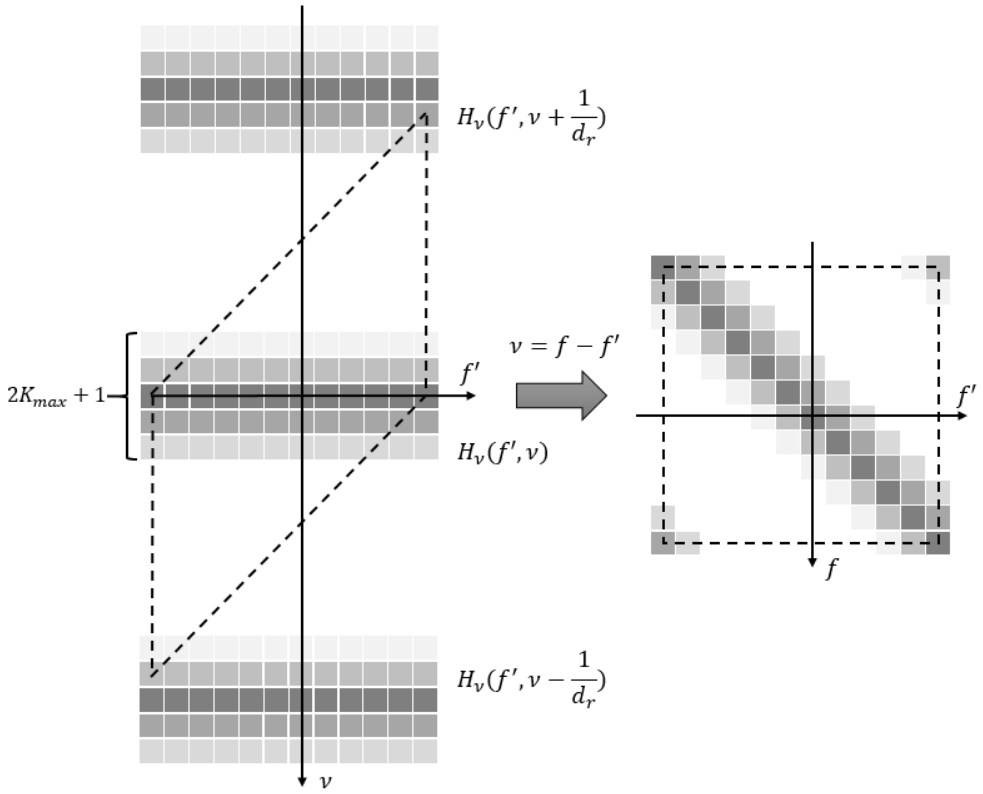

Figure 2.3: Construction of frequency-Doppler domain channel matrix.

2.4 in discrete form. Their respective delay-time domain and frequency-Doppler domain channel matrices are also illustrated in Fig. 2.4 according to the processes shown in Figs. 2.2 and 2.3 respectively.

Remark 1. Similar discrete-frequency signal models demonstrating the circular stripe diagonal property in their channel matrices can be found in the literature [72] for OFDM systems. However, such signal models do not consider the resolvability of the channel Doppler spread, and are also only valid for on-grid multipath delays and Doppler shifts. Due to the relatively short frame length of the OFDM symbols, the actual Doppler shifts incurred in the fast fading channel may not be fully resolvable. On the contrary, the proposed frequency-Doppler domain channel matrix $\mathbf{H}_v$ can be constructed for any multipath delay τ_i and Doppler shift ν_i through the TF transfer function as shown in Eqs. (2.20) and (2.16).

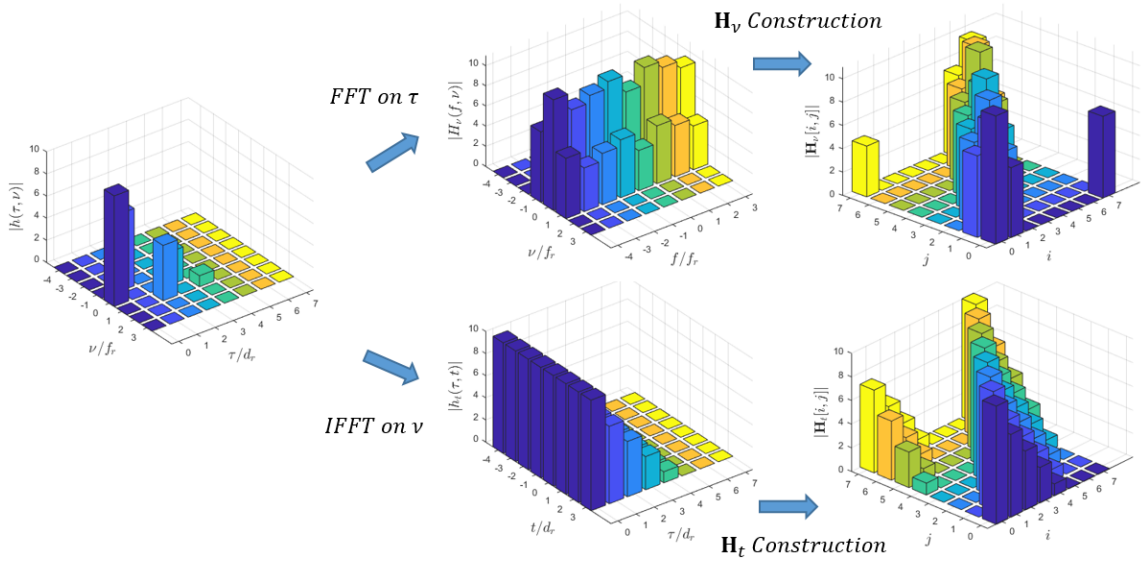

Figure 2.4: An example demonstrating the process of forming the delay-time domain and frequency-Doppler domain channel matrices.

To explore the relationship between discrete time and frequency signal models, let's start from discretising the channel representations expressed in Eq. (2.7). From the above analysis, the discrete frequency domain response $H_\nu(if_r, jf_r)$ is periodic with a period of $1/d_r$ due to the sampling and discretisation, though the continuous domain response $h_t(\tau,t)$ and $H_\nu(f,\nu)$ are aperiodic and band-limited. Hence $H_\nu(f,\nu)$ can be extended to a periodic function with period $1/d_r$ along both frequency and Doppler dimensions as

$$\begin{aligned}
\widetilde{H}_\nu(f,\nu) &= \sum_{j=-\infty}^{\infty}\sum_{i=-\infty}^{\infty} H_\nu(f+i/d_r, \nu+j/d_r) \\
&= \sum_{j=-\infty}^{\infty}\sum_{i=-\infty}^{\infty}\int_{-\infty}^{+\infty}\int_{-\infty}^{+\infty} h_t(\tau,t)e^{-\mathbf{j}2\pi(f+i/d_r)\tau}e^{-\mathbf{j}2\pi(\nu+j/d_r)t}d\tau dt \\
&= \int_{-\infty}^{+\infty}\int_{-\infty}^{+\infty}\Big(\sum_{j=-\infty}^{\infty}\sum_{i=-\infty}^{\infty} e^{-\mathbf{j}2\pi i\tau/d_r}e^{-\mathbf{j}2\pi jt/d_r}\Big)h_t(\tau,t)e^{-\mathbf{j}2\pi f\tau}e^{-\mathbf{j}2\pi\nu t}d\tau dt \\
&= \int_{-\infty}^{+\infty}\int_{-\infty}^{+\infty}\Big(d_r^2\sum_{m=-\infty}^{\infty}\sum_{n=-\infty}^{\infty}\delta(\tau-md_r)\delta(t-nd_r)h_t(\tau,t)e^{-\mathbf{j}2\pi f\tau}e^{-\mathbf{j}2\pi\nu t}d\tau dt \\
&= d_r^2\sum_{m=-\infty}^{\infty}\sum_{n=-\infty}^{\infty} h_t(md_r,nd_r)e^{-\mathbf{j}2\pi fmd_r}e^{-\mathbf{j}2\pi\nu nd_r},
\end{aligned} \tag{2.24}$$

which is the 2D Fourier transform of the discretised $h_\nu(\tau,t)$ with sampling period d_r.

When deriving (2.24), the equality $\sum_{n=-\infty}^{\infty} e^{-j2\pi fTn} = \frac{1}{T}\sum_{k=-\infty}^{\infty}\delta(f-k/T)$ and (2.3) are applied. Further discretising $\widetilde{H}_v(f,\nu)$ in one period with Doppler resolution f_r, which is equivalent to $H_v(kf_r, lf_r)$, we have

$$\begin{aligned}\widetilde{H}_v(kf_r, lf_r) &= d_r^2 \sum_{m=-\infty}^{\infty}\sum_{n=-\infty}^{\infty} h_t(md_r, nd_r) e^{-\mathbf{j}2\pi kf_r md_r} e^{-\mathbf{j}2\pi lf_r nd_r} \\ &= d_r^2 \sum_{m=0}^{MN-1}\sum_{n=0}^{MN-1} \widetilde{h}_t(md_r, nd_r) e^{-\frac{\mathbf{j}2\pi km}{MN}} e^{-\frac{\mathbf{j}2\pi ln}{MN}}, \end{aligned} \tag{2.25}$$

where $e^{-j2\pi f_r d_r km}$ and $e^{-j2\pi f_r d_r ln}$ are periodic about m and n, respectively, with the same period $1/(f_r d_r) = MN$, $\widetilde{h}_t(\tau,t) = \sum_{i=-\infty}^{\infty}\sum_{j=-\infty}^{\infty} h_t(\tau + i/f_r, t + j/f_r)$ is the periodically extended $h_t(\tau,t)$ with period $1/f_r$ in both delay and time dimensions. It is seen that one period of $\tilde{H}_v(kf_r, lf_r)$ is the 2D discrete Fourier transform of one period of $\tilde{h}_t(md_r, nd_r)$ which is equivalent to $h_t[m,n]$ multiplied by a scaling factor d_r^2.

Then, let $lf_r = (k'-k)f_r$ and Eq. (2.25) can be expressed as

$$\begin{aligned}\widetilde{H}_v(kf_r, (k'-k)f_r) &= d_r^2 \sum_{m=0}^{MN-1}\sum_{n=0}^{MN-1} \widetilde{h}_t(md_r, nd_r) e^{-\frac{\mathbf{j}2\pi km}{MN}} e^{-\frac{\mathbf{j}2\pi(k'-k)n}{MN}} \\ &= d_r^2 \sum_{m=0}^{MN-1}\sum_{n=0}^{MN-1} \widetilde{h}_t(md_r, nd_r) e^{\frac{\mathbf{j}2\pi k(n-m)}{MN}} e^{-\frac{\mathbf{j}2\pi k'n}{MN}}. \end{aligned} \tag{2.26}$$

Substituting $n-m$ with a new variable m', we have $m = n - m'$. Multiplying f_r to both sides of Eq. (2.26), we have

$$\begin{aligned} f_r\widetilde{H}_v(kf_r, (k'-k)f_r) &= f_r d_r^2 \sum_{m'=1-MN}^{MN-1}\sum_{n=0}^{MN-1} \widetilde{h}_t((n-m')d_r, nd_r) e^{\frac{\mathbf{j}2\pi km'}{MN}} e^{-\frac{\mathbf{j}2\pi k'n}{MN}} \\ &= \frac{1}{MN}\sum_{m'=0}^{MN-1}\sum_{n=0}^{MN-1} d_r \widetilde{h}_t((n-m')d_r, nd_r) e^{\frac{\mathbf{j}2\pi km'}{MN}} e^{-\frac{\mathbf{j}2\pi k'n}{MN}}, \end{aligned} \tag{2.27}$$

where $1/MN = f_r d_r$ is the normalisation factor of the 2D discrete Fourier transform.

Expressing Eq. (2.27) in a matrix form, the relationship between the frequency-Doppler channel matrix $\mathbf{H}_\nu$ and the delay-time channel matrix $\mathbf{H}_t$ can be found as

$$\mathbf{H}_\nu = \mathbf{F}_{MN}\mathbf{H}_t\mathbf{F}_{MN}^{\mathbf{H}}, \tag{2.28}$$

where $(\cdot)^{\mathbf{H}}$ denotes the conjugate and transpose of a matrix, $\mathbf{F}_{MN}$ denotes the length MN DFT matrix, and $\mathbf{F}_{MN}^{\mathbf{H}}$ denotes the inverse DFT (IDFT) matrix. $\mathbf{F}_{MN}\mathbf{F}_{MN}^{\mathbf{H}} = \mathbf{F}_{MN}^{\mathbf{H}}\mathbf{F}_{MN} = \mathbf{I}_{MN}$, where $\mathbf{I}_{MN}$ is the identity matrix of order MN.

Eq. (2.28) reveals a generalised relationship between time domain and frequency domain channel models which is the discrete version of (2.14). For the conventional time-invariant channel, $\mathbf{H}_t$ is a circulant matrix composed of the channel's impulse response, and $\mathbf{H}_v$ is a diagonal matrix composed of $\mathbf{H}_t$'s eigenvalues which represent the channel's frequency response. However, for time-varying channels, $\mathbf{H}_v$ is not a diagonal matrix any more but a stripe diagonal matrix with the stripe width $2K_{\max}+1$ as shown in Fig. 2.3.

Finally, denoting the discrete versions of $h(\tau,v)$ and $H(f,t)$ over a signal frame of length MN as MN-by-MN matrices $\mathbf{h}$ and $\mathbf{H}$ respectively, $d_r h_t[i,j]$ as $\mathbf{h}_t$, and $f_r H_v[i,j]$ as $\mathbf{h}_v$, the relationships among the different channel representations in matrix form are summarised in Fig. 2.5. Note that the scaling factors after applying the DFT and IDFT matrices are different from those defined in DFT and IDFT.

2.4 Simulation Results

In this thesis, the European Telecommunications Standards Institute (ETSI) tapped delay line (TDL) models, which are valid for frequency range from 0.5 GHz to 100 GHz with a maximum bandwidth of 2 GHz, are adopted as the multipath channel models [73]. TDL channel models define the time delay over line-of-sight (LOS) and non-line-of-sight (NLOS) channels in different scenarios. The simulation parameters are listed in Table 2.1. Note that each TDL channel model defines several application scenarios with different time delay spreads. However, as has been reported in [74], very similar performance is achieved in different scenarios. As such, only the urban macrocell (UMa) channels are taken as examples in the following up simulations. Throughout this thesis, both LOS and

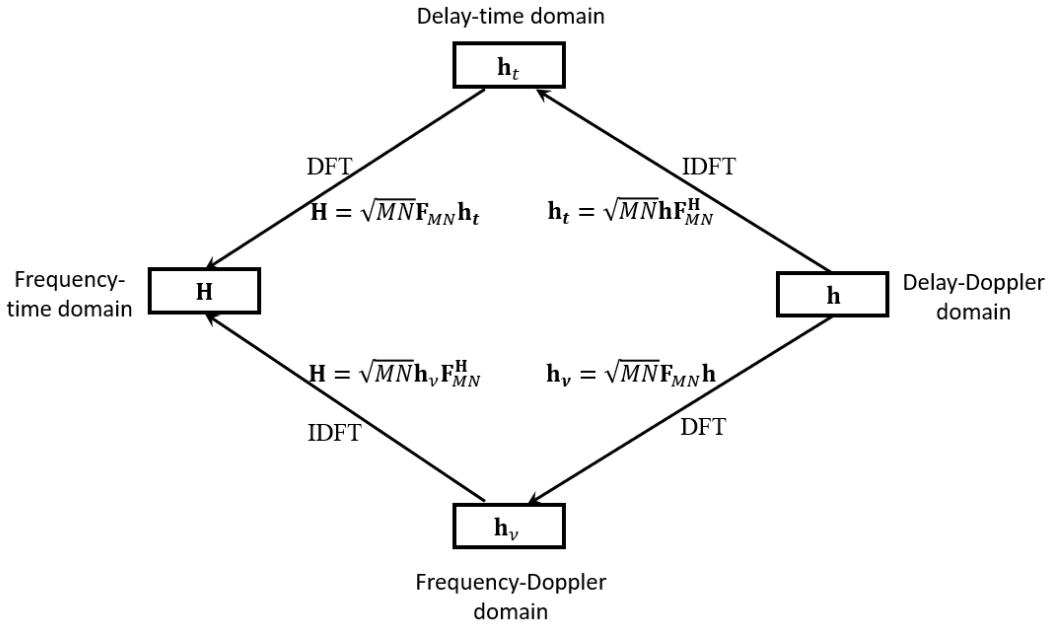

Figure 2.5: Relationships among channel matrices in different domains.

NLOS channels are simulated with TDL-D and TDL-A models respectively. Accordingly, the maximum multipath delays $d_{\max}$ are 4.55 μs and 3.51 μs for LOS and NLOS channels respectively. The channel power delay profiles for TDL-A and TDL-D channel model are shown in Fig. 2.6. The Doppler frequency shifts are added to all paths, which vary in every channel realisation and obey uniform distribution over $[-K_{\max}, K_{\max}]$.

Fig. 2.7 plots one realisation of the frequency-time representation of the fast fading TDL-D LOS channel, and the channel variation with time is clearly shown in the figure. Fig. 2.8 shows the frequency-Doppler channel matrix $\mathbf{H}_\nu$ derived from $H(f,t)$ with full Doppler resolution. It is seen that the non-zero elements appear in a narrow stripe along the diagonal lines and other elements are all zeros, allowing low-complexity algorithms to be developed in the following chapter. According to the parameters shown in Table 2.1, the width of the stripe is $2K_{\max}+1=7$, and is very small compared with the 8192×8192 matrix size. The circular stripe diagonal nature of $\mathbf{H}_\nu$ allows for more efficient matrix inversion operation.

Table 2.1: Simulation Parameters

Carrier Frequency (f_c)	No. of Subcarriers (M)	No. of OFDM/SC-FDE Symbols (N)	Subcarrier Spacing (f_Δ)
6 GHz	256	32	30 KHz
Bandwidth ($W = Mf_\Delta$)	Duration of OFDM/SC-FDE Symbol ($T = M/W$)	Delay Resolution ($d_r = 1/W$)	Doppler Resolution ($f_r = 1/NT$)
7.68 MHz	33.33 μs	130.21 ns	937.5 Hz
Maximum Speed ($v_{\max}$)	Maximum Doppler Frequency ($f_{\max} = f_c \frac{v_{\max}}{v_c}$, $v_c = 3 \times 10^8\ m/s$)	No. of Doppler Shifts (Positive or Negative) ($K_{\max} = \left\lceil \frac{f_{\max}}{f_r} \right\rceil$)	No. of Multipaths ($L_{\max} = \left\lceil \frac{d_{\max}}{d_r} \right\rceil$)
500 Km/h	2777.8 Hz	≥ 3	≥ 35(LOS), 27(NLOS)

2.5 Conclusions

In this chapter, continuous and discrete channel representations in different domains and their relationships have been derived and proved through simulation, offering some alternative ways in addition to the conventional delay-Doppler approach for characterising the fast fading channels. Especially, the concise structure of frequency domain channel matrix will be very useful to develop low-complexity equalisation and estimation techniques in the frequency domain. The signal models proposed in this chapter will be very useful to overcome the challenge of complex channel conditions caused by Doppler frequency shifts in multipaths, paving the way for low-complexity equalisations to be developed.

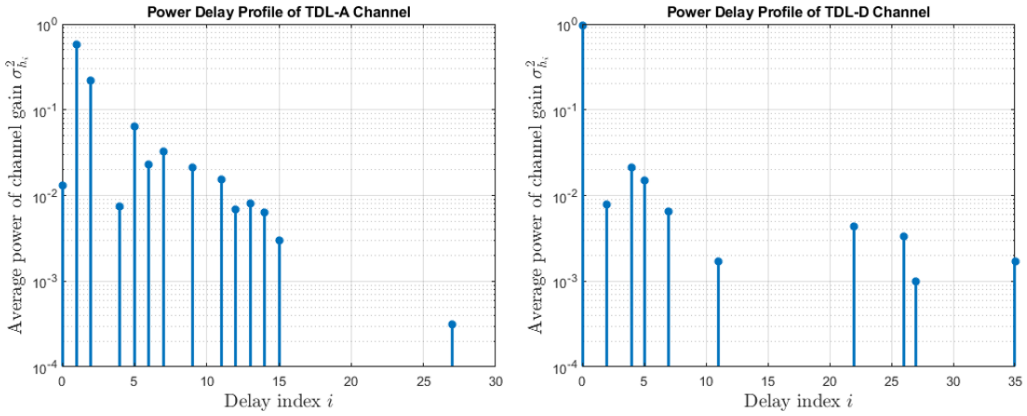

(a) (b)

Figure 2.6: Power delay profiles of TDL-A (a) and TDL-D (b) channel models.

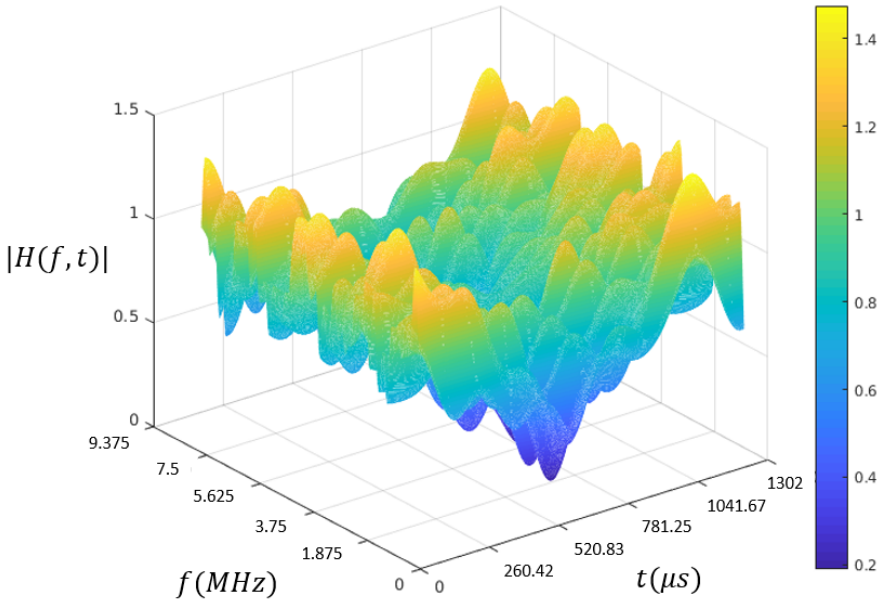

Figure 2.7: Frequency-time domain representation of fast fading channels.

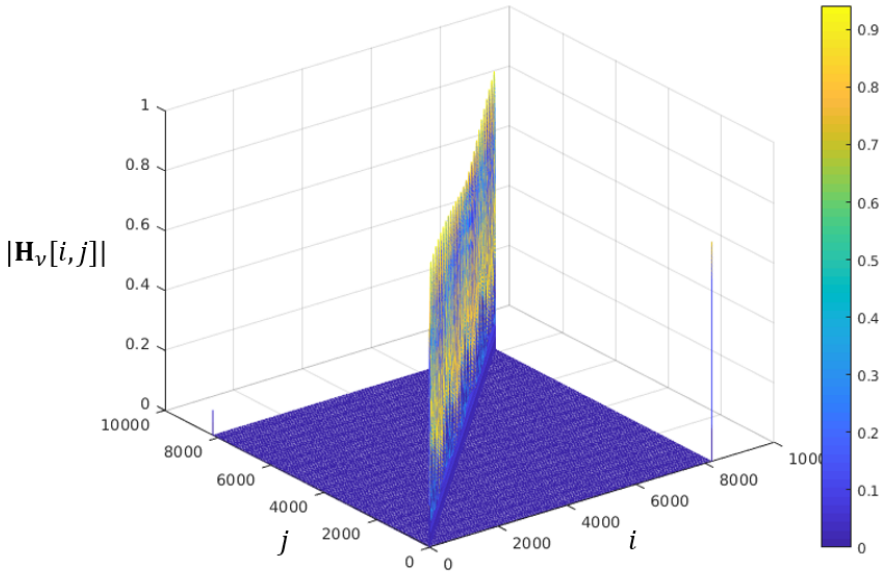

Figure 2.8: Frequency-Doppler domain channel matrix over fast fading channels.

CHAPTER 3

LOW-COMPLEXITY EQUALISATION TECHNIQUES OVER FAST FADING CHANNELS

3.1 Introduction and Literature Review

3.1.1 Conventional Modulation over Fast Fading Channels

Conventional multicarrier transmission schemes, such as OFDM, are prone to ICI caused by the Doppler effect in fast fading channels [75]. Short frames of transmitted signals are usually used such that the channel fading can be assumed constant within a frame and the variation of the channel with time can be tracked from frame to frame. As such, the time-varying channel is treated as slow fading when the channel coherence time is large relative to the frame length. However, the channel variation cannot be treated as constant in fast fading channels where the channel coherence time is much smaller than the frame length [76]. Therefore, ICI mitigation techniques are necessary, and previous work for conventional schemes can be classified into two categories. The first category focuses on OFDM transmitter design, such as the ICI self cancellation techniques [77, 78]. The other category is ICI cancellation at the receiver, including the

efforts on channel estimation and equalisation. Kalman filter [79, 80], Bayesian methods [81–83] and maximum-likelihood (ML) detection [84] have been adopted for channel tracking and estimation. Besides, optimised equalisations are also proposed using soft-Kalman filter [85] and MMSE methods [71]. However, when the Doppler frequency shift is significant and channel coherent time becomes much smaller than the signal frame length, disadvantage on time diversity limits the performance of conventional modulations in such fast fading channels.

3.1.2 OTFS over Fast Fading Channels

The recently proposed OTFS modulation shows outstanding performance in fast fading channels [38] [86], with advantages of both high spectral efficiency and relatively low PAPR [69]. OTFS is formulated in a 2D data plane and its signals are represented in both delay-Doppler domain and frequency-time domain [87]. Using a long signal frame, this modulation technique can overcome the difficulty in equalising signals with multiple Doppler frequency shifts and multipath fading, and hence can exploit the diversity in both time and frequency domains. OTFS offers a new approach for next generation wireless systems to deal with the fast fading channels. Existing works on OTFS have been devoted to various aspects such as system structures, diversity analysis, estimation, and equalisation algorithms [54–56, 67–71]. However, most of them are based on delay-Doppler domain analysis and demonstrate high computational complexity, which makes them difficult to be applied in practice [67]. Despite these drawbacks, OTFS modulation still offers great entry point to solve fast fading problems.

3.1.3 Existing Equalisation Techniques of OTFS

A brief review of the existing research on OTFS is provided as follows. Firstly, as the structures of OTFS and OFDM are highly related, some research interests are placed in connecting them to form new transmission schemes. In [88], the Symplectic

Finite Fourier Transform (SFFT) and inverse SFFT (ISFFT) processes are combined with OFDM modulation/demodulation to significantly reduce the computing complexity compared with that of the original OTFS. In [89], this OFDM-based OTFS is analysed in a multiple-input multiple-output (MIMO) system. Unfortunately, this method has not been proved either via simulation or in practical system. Hence, further research is needed to prove its performance over fast fading channels. Secondly, diversity performance is analysed in [68, 70, 90] assuming that ML equalisation is adopted in the system. However, all these works are based on simple channels with no more than four multipaths. Meanwhile, the study on low-complexity or more practical linear equalisers for OTFS is still very limited, not to mention further analytical performance characterisation for these equalisers. Thirdly, embedded pilot-aided channel estimation is proposed for OTFS in [91]. In particular, a 3D-structured orthogonal matching pursuit algorithm based channel estimation technique is proposed to solve the challenge of a large number of base station antennas [92, 93]. Finally, more work has been focused on developing more efficient equalisation techniques to fully exploit channel diversity, such as MCMC in [94] and linear MMSE in [67, 95]. Note that an equalisation based on MP algorithm is proposed in [53, 54], and shows outstanding performance among these equalisers. A simple sparse input-output model is proposed in [55] based on MP, and a more general form derived from OTFS is given in [69], which is called asymmetric OFDM. It is observed that OTFS shows the same performance as OFDM in static channels, but has the capability of adapting to fast fading channels. However, the above mentioned equalisation techniques have some drawbacks. For example, authors in [53] apply iterative algorithms to recover the signal, which greatly increases the computational complexity. The classical MMSE equalisation also introduces high complexity to the OTFS system since the equalisation requires matrix inversion which is prohibitively complicated due to the large size of the channel matrix.

3.1.4 Chapter Structure

In this chapter, a low-complexity frequency domain MMSE equalisation algorithm for OTFS is proposed to combat fast fading channels based on the circular stripe diagonal nature of the frequency-Doppler channel matrix. The discrete received signal models for conventional systems are then derived where the Doppler spread incurred in the fast fading channel is only partially resolvable. Using the new discrete signal models, it is shown that MMSE equalisation can also be applied in systems with conventional modulations, such as OFDM and SC-FDE, to improve their performance over fast fading channels. Finally, the theoretical performance of MMSE equalisation is analysed, which establishes the relationships among the output SNR, the fast fading channel, and the signal modulation through eigenvalue decomposition of the channel matrix. Simulation results using OTFS, OFDM, and SC-FDE modulations under both LOS and NLOS fast fading channels are provided to validate the theoretical analysis and demonstrate the performance of the proposed MMSE equalisation.

3.2 Low-Complexity MMSE Equalisation

3.2.1 MMSE Equalisation with Fully Resolvable Doppler Spread

Given the multipath and Doppler frequency resolutions d_r and f_r, the transmission system requires a minimum bandwidth of $1/d_r$ and the transmitted signal requires a minimum length of $1/f_r$. Under these conditions, the received signal can be modelled in the discrete time and frequency domains as shown in (2.18) and (2.22) respectively. Further assume that the channel matrices are known. The transmitted signal in either the time or frequency domain can be recovered under the MMSE criterion. In the discrete time domain, an estimate of the transmitted signal after MMSE equalisation can be

expressed as

$$\hat{\mathbf{s}} = \mathbf{G}_t \mathbf{r}, \tag{3.1}$$

where $\mathbf{G}_t$ can be derived, following a well established process, as

$$\mathbf{G}_t = \mathbf{H}_t^{\mathbf{H}} (\mathbf{H}_t \mathbf{H}_t^{\mathbf{H}} + \frac{1}{\gamma_{in}} \mathbf{I}_{MN})^{-1}, \tag{3.2}$$

and the term γ_{in} denotes the input signal-to-noise ratio (SNR) at the receiver [96].

In the discrete frequency domain, according to [96], an estimate of the transmitted signal after MMSE equalisation can be expressed as

$$\hat{\mathbf{S}} = \mathbf{G}_v \mathbf{R}, \tag{3.3}$$

where $\mathbf{G}_v$ is similarly derived as

$$\mathbf{G}_v = \mathbf{H}_v^{\mathbf{H}} (\mathbf{H}_v \mathbf{H}_v^{\mathbf{H}} + \frac{1}{\gamma_{in}} \mathbf{I}_{MN})^{-1}. \tag{3.4}$$

The mean square error after MMSE equalisation can be expressed as $tr(\mathbf{I}_{MN} - \mathbf{G}_t \mathbf{h}_t) = tr(\mathbf{I}_{MN}) - tr(\mathbf{G}_t \mathbf{h}_t)$ in the time domain or $tr(\mathbf{I}_{MN} - \mathbf{G}_v \mathbf{H}_v) = tr(\mathbf{I}_{MN}) - tr(\mathbf{G}_v \mathbf{H}_v)$ in the frequency domain, as $tr(\mathbf{G}_v \mathbf{H}_v) = tr(\mathbf{G}_t \mathbf{H}_t)$ according to (2.28). This means that the time domain and frequency domain MMSE equalisers produce the same mean square error under the same channel condition.

Note that, due to the different constructions of the delay-time channel matrix and the frequency-Doppler channel matrix, the computational complexity involved in the calculation of the equalisation matrix is different. According to the ETSI channel model adopted in Chapter 2, the number of resolvable Doppler frequencies is much smaller than that of resolvable multipath taps/delays in the time domain . Therefore, performing MMSE equalisation in the frequency domain has a significant advantage in terms of receiver complexity. This is similar to the case that conventional frequency domain one-tap equalisation is less complicated than the time domain linear equalisation over a

time-invariant channel. In general, the following remark can be obtained regarding the MMSE equalisation complexity.

Remark 2. The computational complexity of the frequency domain MMSE equalisation is $O((1+4K_{\max})^2 MN)$ in terms of the number of complex multiplications and divisions, where MN is the length of the signal frame and $K_{\max}$ is the number of positive (or negative) Doppler frequencies. The inversion of a circular stripe diagonal matrix is well-understood and the detailed proofs for the computational complexity of such channel matrix are shown in Appendix A [97].

Note that if conventional MMSE equalisation is used without exploring the structure of the frequency-Doppler domain channel matrix, the computational complexity will be $O((MN)^3)$. An example is provided here to demonstrate the advantage of frequency-domain MMSE equalisation. In a practical scenario as defined in the ETSI 5G channel models (for more details see Table 2.1 in Chapter 2), we have $M = 256$, $N = 32$, $L_{\max} = 35$ (LOS) and $K_{\max} = 3$. With frequency domain MMSE equalisation, the number of complex multiplications/divisions is in the order of 1.4×10^6, whereas with time domain MMSE equalisation it is 5.5×10^{11}. Also note that $K_{\max}$ may be larger than $L_{\max}$ in some channel conditions. Alternative time-domain equalisation techniques such as [67] and [98] can be applied to achieve a lower complexity in this case. Since the same MMSE algorithm is adopted, the performance is similar among the proposed scheme and other time-domain schemes. However, the computation complexities are different. The complex multiplications in [67] is $O(L_{\max}^2 + L_{\max})MN$, and hence the complexity is highly dependent of the delay spread $L_{\max}$. Comparatively, the complexity of the proposed scheme mainly depends on the Doppler spread which is generally much smaller than the delay spread, in terms of their respective quantised values. For example, with the channel model shown in Table 2.1, the complexity of [67] would be in the order of 10^7, which is still higher than that of the proposed frequency-domain scheme.

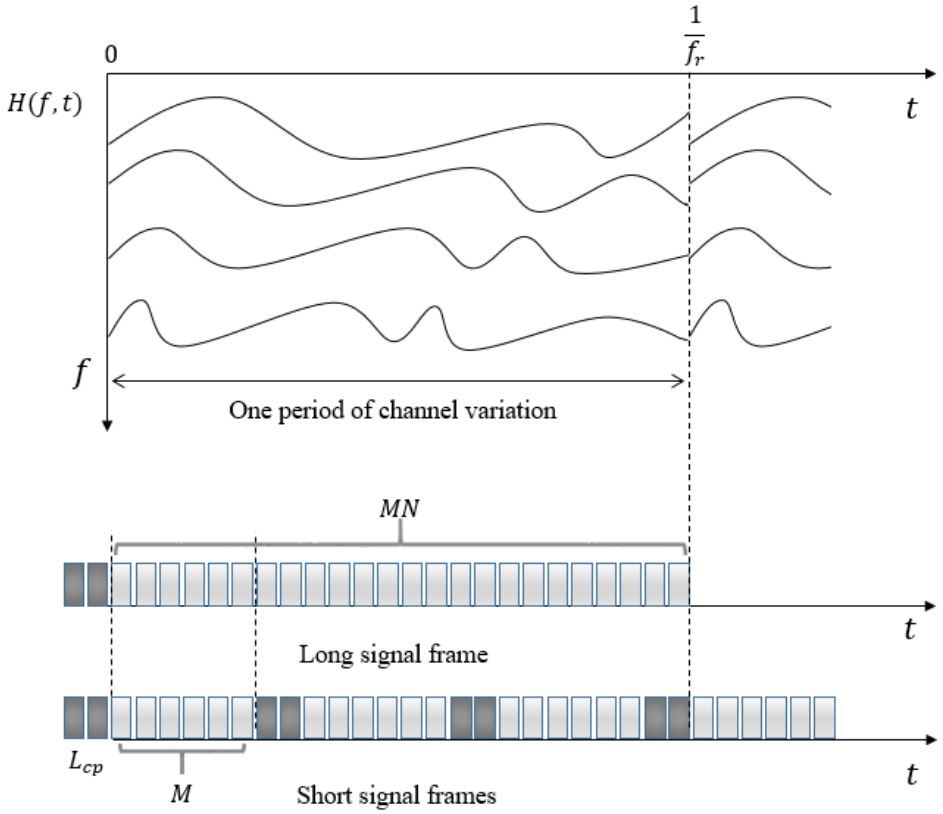

Figure 3.1: Comparison between long and short signal frames.

3.2.2 MMSE Equalisation with Partially Resolvable Doppler Spread

If the signal frame is shorter than $1/f_r$, the received signal will not be able to resolve all the Doppler frequencies. This is the case for many existing systems. Without loss of generality, it is assumed that the short signal frame has M samples with length $T = Md_r$ whereas the long signal frame has MN samples with length NT. It is also assumed that the CPs have the same length $T_{cp} = L_{cp}d_r$ for both the long and short signal frames. Fig. 3.1 provides a comparison between long and short signal frames. Given the Doppler resolution f_r, one period of the frequency-time domain representation of the fast fading channel is also illustrated to show the channel variation. It is seen that the short signal frame only experiences a part rather than a full period of the channel variation.

Suppose that the first short signal frame is aligned with the long signal frame. After passing through the same fast fading channel, the n-th received short-frame signal, $n = 0, 1, ...N-1$, can be expressed in the time domain as

$$\mathbf{r}^{(n)} = \mathbf{H}_t^{(n)}\mathbf{s}^{(n)} + \mathbf{w}^{(n)}, \tag{3.5}$$

where $\mathbf{s}^{(n)}$ and $\mathbf{w}^{(n)}$ are the n-th transmitted signal vector and noise vector respectively, and $\mathbf{H}_t^{(n)}$ is the $M \times M$ delay-time channel matrix which can be constructed similar to Eq. (2.19) and is shown in Fig. 2.2 except that the size of the matrix is $M \times M$ and the delay-time channel representation for the n-th short signal frame is now $h_t^{(n)}(\tau, t) = h_t(\tau, t + n(T + T_{cp}))$ for $0 \le t < T$. In the frequency domain, the n-th short-frame received signal can be expressed as

$$\mathbf{R}^{(n)} = \mathbf{H}_\nu^{(n)}\mathbf{S}^{(n)} + \mathbf{W}^{(n)}, \tag{3.6}$$

where $\mathbf{S}^{(n)}$ and $\mathbf{W}^{(n)}$ are the n-th frequency domain transmitted signal vector and noise vector respectively, and $\mathbf{H}_\nu^{(n)}$is the $M \times M$ frequency-Doppler channel matrix which can be constructed similar to Eq. (2.23), with reference to Fig. 2.3. However, the discrete frequency-Doppler channel representation for the n-th short signal frame should now be calculated as

$$H_\nu^{(n)}[i, j] = \sum_{j'=-K_{\max}}^{K_{\max}} e^{\frac{\mathbf{j}2\pi(M+L_{cp})nj'}{MN}} H_\nu[iN, j']\phi(\frac{2\pi}{MN}(jN - j')), \tag{3.7}$$

where $0 \le i, j \le M-1$ and $\phi(w)$ is the Fourier transform of a discrete rectangular window function defined as

$$\phi(\omega) = \frac{\sin(\omega M/2)}{M\sin(\omega/2)} e^{-\mathbf{j}\omega(M-1)/2}. \tag{3.8}$$

The calculation expressed in Eq. (3.7) can be explained as follows. In order to calculate the discrete frequency-Doppler representation of the fast fading channel during the n-th short signal frame, its frequency-time representation which is a time shifted version of

$H(f,t)$ advanced by $n(T+T_{cp})$ is needed, i.e., $H^{(n)}(f,t) = H(f,t+n(T+T_{cp}))$ for $0 \le t < T$, and then weighted by a rectangular window function of width T. The windowing becomes a convolution in the frequency-Doppler representation. Eq. (3.7) is the discrete version of such convolution. The result is finally down-sampled by N times as the frequency and Doppler resolution is reduced by N times.

Similar to Eq. (2.28), we have $\mathbf{H}_v^{(n)} = \mathbf{F}_M \mathbf{H}_t^{(n)} \mathbf{F}_M^{\mathbf{H}}$, where $\mathbf{F}_M$ and $\mathbf{F}_M^{\mathbf{H}}$ are the DFT and IDFT matrices, respectively, satisfying $\mathbf{F}_M \mathbf{F}_M^{\mathbf{H}} = \mathbf{F}_M^{\mathbf{H}} \mathbf{F}_M = \mathbf{I}_M$ and $\mathbf{I}_M$ is the identity matrix of order M.

Given the discrete signal models in both the time and frequency domains shown in (3.5) and (3.6), the MMSE equalisation methods for the short signal frames can be derived accordingly similar to (3.2) and (3.4), and the same equalisation performance can be achieved in either time or frequency domain. Due to the reduced frame length, the equalisation complexity is also reduced.

Remark 3. Though the signal model expressed in (3.6) is similar to those found in the literature, e.g., [72] and those mentioned in Remark 2, the frequency-Doppler channel matrix $\mathbf{H}_v^{(n)}$ has different meanings, i.e., each line in the diagonal stripe of the matrix does not represent a resolvable Doppler frequency, but the convolution of the frequency-Doppler transfer function with the Fourier transform of a windowing function which reflects the shorter signal frame length. In addition, considering a full period of channel time variation given the Doppler resolution, the location of the short signal frame also has an impact on $\mathbf{H}_v^{(n)}$, which is reflected by the phase factor in (3.7).

3.3 Equalisation Performance Analysis

3.3.1 Input-Output Relationships

Three modulation schemes, OTFS, OFDM and SC-FDE, are considered here. Regarding Doppler resolution, OTFS can fully resolve all the Doppler frequencies due to its long

signal frame, whereas OFDM and SC-FDE can only resolve part of them due to shorter signal frames.

Assume that the total number of data symbols to be transmitted is MN, and the data has been modulated with quadrature amplitude modulation (QAM), denoted by $x[i]$, $i = 0, 1, ..., MN-1$. In the matrix form, the data symbol set can be expressed as an $M \times N$ matrix $\mathbf{X} = [\mathbf{x}_0, \mathbf{x}_1, ..., \mathbf{x}_{N-1}]$ where

$$\mathbf{x}_n = (x[nM], x[nM+1], ..., x[nM+M-1])^T, n = 0, 1, ..., N-1, \tag{3.9}$$

is a column vector and $(\cdot)^T$ denotes the transpose of a matrix.

After the ISFFT, Heisenberg transform and pulse shaping, CP is prepended to the signal frame. The modulated OTFS signal is then transmitted over a fast fading channel and a time-domain sequence $r[i], i = 0, 1, ...MN-1$, is received. According to [55] and the channel model (2.22), the received signal can be expressed in the matrix form

$$\mathbf{R} = \mathbf{H}_v \mathbf{F}_{MN} (\mathbf{F}_N^{\mathbf{H}} \otimes \mathbf{I}_M)\mathbf{x} + \mathbf{W}, \tag{3.10}$$

where $\mathbf{F}_N^{\mathbf{H}}$ denotes the N-point IFFT matrix, $\otimes$ denotes Kronecker product, $\mathbf{x} = \text{vec}(\mathbf{X})$ is the vectorised form of matrix $\mathbf{X}$ and $\mathbf{W}$ is the noise vector. The received data symbols after MMSE equalisation can be expressed as

$$\mathbf{y} = (\mathbf{F}_N \otimes \mathbf{I}_M)\mathbf{F}_{MN}^{\mathbf{H}} \mathbf{G}_v \mathbf{H}_v \mathbf{F}_{MN} (\mathbf{F}_N^{\mathbf{H}} \otimes \mathbf{I}_M)\mathbf{x} + (\mathbf{F}_N \otimes \mathbf{I}_M)\mathbf{F}_{MN}^{\mathbf{H}} \mathbf{G}_v \mathbf{W}. \tag{3.11}$$

Similarly, letting $\mathbf{x}^{(n)}$ denote the n-th transmitted OFDM or SC-FDE data symbol vector, the n-th received OFDM data symbol vector after MMSE equalisation can be expressed as

$$\mathbf{y}^{(n)} = \mathbf{G}_v^{(n)} \mathbf{H}_v^{(n)} \mathbf{x}^{(n)} + \mathbf{G}_v^{(n)} \mathbf{W}, \tag{3.12}$$

where $\mathbf{G}_v^{(n)}$ denotes the frequency domain equalisation matrix for the n-th OFDM symbol. Assuming SC-FDE has the same frame structure, the n-th received data symbol vector

for SC-FDE can be expressed as

$$\mathbf{y}^{(n)} = \mathbf{F}_M^{\mathbf{H}} \mathbf{G}_v^{(n)} \mathbf{H}_v^{(n)} \mathbf{F}_M \mathbf{x}^{(n)} + \mathbf{F}_M^{\mathbf{H}} \mathbf{G}_v^{(n)} \mathbf{W}. \tag{3.13}$$

Note that the received data symbol expressions for OTFS, OFDM and SC-FDE have some similarity. Hence, a general representation can be written as

$$\mathbf{y} = \mathbf{V}^{\mathbf{H}} \mathbf{F}^{\mathbf{H}} \mathbf{G}_v \mathbf{H}_v \mathbf{F} \mathbf{V} \mathbf{x} + \mathbf{V}^{\mathbf{H}} \mathbf{F}^{\mathbf{H}} \mathbf{G}_v \mathbf{W}, \tag{3.14}$$

where $\mathbf{V}$ and $\mathbf{V}^{\mathbf{H}}$ denote the signal modulation and demodulation matrix respectively, satisfying $\mathbf{V}\mathbf{V}^{\mathbf{H}} = \mathbf{V}^{\mathbf{H}}\mathbf{V} = \mathbf{I}_{MN}$ or $\mathbf{I}_M$. For example, $\mathbf{V}$ is $\mathbf{F}_N^{\mathbf{H}} \otimes \mathbf{I}_M$ for OTFS, $\mathbf{F}_M^{\mathbf{H}}$ for OFDM, and $\mathbf{I}_M$ for SC-FDE. Note that for different modulations, the size of $\mathbf{G}_v$, $\mathbf{H}_v$, $\mathbf{x}$ and $\mathbf{y}$ may be different. The size of both $\mathbf{G}_v$ and $\mathbf{H}_v$ is $MN \times MN$ for OTFS with $MN \times 1$ signal vectors $\mathbf{x}$ and $\mathbf{y}$, whereas the size of $\mathbf{G}_v$ and $\mathbf{H}_v$ are $M \times M$ for OFDM and SC-FDE with $M \times 1$ signal vectors $\mathbf{x}$ and $\mathbf{y}$.

3.3.2 Output SNR Analysis

In the following analysis, the general representation with frequency domain MMSE equalisation in (3.14) is utilised to determine the output SNR after equalisation, assuming the data matrix size is $M \times N$. The output SNR will be the same if frequency domain MMSE equalisation is used. The same analysis can also be applied to OFDM and SC-FDE but with smaller channel matrix dimensions. For simplicity, $\mathbf{A} = \mathbf{V}^{\mathbf{H}} \mathbf{F}_{MN}^{\mathbf{H}} \mathbf{G}_v \mathbf{H}_v \mathbf{F}_{MN} \mathbf{V}$ and $\mathbf{B} = \mathbf{V}^{\mathbf{H}} \mathbf{F}_{MN}^{\mathbf{H}} \mathbf{G}_v$ are also defined. Assuming that the data symbols are independent of each other with the average power σ_x^2, i.e., $E\{\mathbf{x}\mathbf{x}^{\mathbf{H}}\} = \sigma_x^2 \mathbf{I}_{MN}$ and the noise power is σ_w^2, i.e., $E\{\mathbf{W}\mathbf{W}^{\mathbf{H}}\} = \sigma_w^2 \mathbf{I}_{MN}$, where $E\{\cdot\}$ denotes ensemble expectation, the covariance matrix of $\mathbf{y}$ can be derived as

$$\begin{aligned} E\{\mathbf{y}\mathbf{y}^{\mathbf{H}}\} &= \mathbf{A} E\{\mathbf{x}\mathbf{x}^{\mathbf{H}}\} \mathbf{A}^{\mathbf{H}} + \mathbf{B} E\{\mathbf{W}\mathbf{W}^{\mathbf{H}}\} \mathbf{B}^{\mathbf{H}} \\ &= \mathbf{C}\sigma_x^2 + \mathbf{D}\sigma_w^2, \end{aligned} \tag{3.15}$$

where $\mathbf{C}$ and $\mathbf{D}$ denote $\mathbf{AA^H}$ and $\mathbf{BB^H}$ respectively. To detect the $(nM+m)$-th data symbol at the m-th row and the n-th column in $\mathbf{X}$, the useful signal power after equalisation is

$$|\mathbf{A}[nM+m, nM+m]|^2 \sigma_x^2 = q_0[m,n], \tag{3.16}$$

where $\mathbf{A}[i,j]$ denotes the element of $\mathbf{A}$ at the i-th row and the j-th column.

The average total power of the $(nM+m)$-th element in $\mathbf{y}$ can also be expressed from (3.15) as

$$\mathbf{C}[nM+m, nM+m]\sigma_x^2 + \mathbf{D}[nM+m, nM+m]\sigma_w^2 = q_1[m,n]. \tag{3.17}$$

For simplicity, let $a_{m,n}$, $c_{m,n}$ and $d_{m,n}$ denote $\mathbf{A}[nM+m, nM+m]$, $\mathbf{C}[nM+m, nM+m]$ and $\mathbf{D}[nM+m, nM+m]$ respectively. Then, the output SNR after equalisation can be expressed as

$$\gamma_{out}[m,n] = \frac{q_0[m,n]}{q_1[m,n] - q_0[m,n]} = \frac{1}{1 - \frac{|a_{m,n}|^2}{c_{m,n} + \frac{1}{\gamma_{in}} d_{m,n}}} - 1, \tag{3.18}$$

where the input SNR is defined as $\gamma_{in} = \sigma_x^2 / \sigma_w^2$.

Eq. (3.18) evaluates the output SNR directly based on the equalised data symbol vector expression (3.14), where the impact of channel condition and signal modulation on the output SNR is not explicitly shown. To demonstrate how the output SNR is affected by the channel and the signal modulation, $\mathbf{A}$ can be expressed as

$$\begin{aligned}
\mathbf{A} &= \mathbf{V^H F_{MN}^H H_v^H} (\mathbf{H_v H_v^H} + \frac{1}{\gamma_{in}} \mathbf{I}_{MN})^{-1} \mathbf{H_v F_{MN} V} \\
&= \mathbf{V^H F_{MN}^H} (\mathbf{I}_{MN} + \frac{1}{\gamma_{in}} (\mathbf{H_v^H H_v})^{-1})^{-1} \mathbf{F_{MN} V} \\
&= \mathbf{V^H} (\mathbf{I}_{MN} + \frac{1}{\gamma_{in}} (\mathbf{F_{MN}^H H_v^H H_v F}_{MN})^{-1})^{-1} \mathbf{V} \\
&= (\mathbf{I}_{MN} + \frac{1}{\gamma_{in}} (\mathbf{V^H F_{MN}^H H_v^H H_v F_{MN} V})^{-1})^{-1}.
\end{aligned} \tag{3.19}$$

Here, $\mathbf{H_v^H H_v}$ is a Hermitian matrix and can be expressed through eigenvalue decomposition as $\mathbf{H_v^H H_v} = \mathbf{Q} \Lambda \mathbf{Q^H}$, where $\mathbf{Q}$ is a square $MN \times MN$ unitary matrix and Λ is

a diagonal matrix with the i-th diagonal element λ_i for $i = 0,1,...,MN-1$. Further denoting $\mathbf{U} = \mathbf{V^H F^H_{MN} Q}$, $\mathbf{A}$ can be simplified as $\mathbf{I}_{MN} - \mathbf{U}\text{diag}\{\frac{1}{\gamma_{in}\lambda_i+1}\}\mathbf{U^H}$, where diag$\{x_i\}$ denotes a diagonal matrix with the i-th diagonal element x_i. According to the MMSE equalisation principle, the normalised noise power for the $(nM+m)$-th equalised data symbol can be expressed as

$$\begin{aligned} J_{nM+m} &= 1 - \mathbf{A}[nM+m, nM+m] \\ &= \sum_{i=0}^{MN-1} \frac{1}{\gamma_{in}\lambda_i + 1} |\mathbf{U}[nM+m, i]|^2. \end{aligned} \tag{3.20}$$

Therefore, the output SNR after equalisation can be expressed as

$$\gamma_{out}[m,n] = \frac{1 - J_{nM+m}}{J_{nM+m}} = \frac{1}{J_{nM+m}} - 1. \tag{3.21}$$

Similarly, the SNR analysis can be performed based on the eigenvalue decomposition of $\mathbf{H_t^H H_t}$, which produces the same eigenvalues as those of $\mathbf{H_v^H H}_v$ but without Fourier transformed eigenvectors.

From (3.20) and (3.21), the output SNR is determined by the eigenvalues of $\mathbf{H_v^H H}_v$, which characterise the channel fading condition, as well as the matrix $\mathbf{U}$ that is related to the signal modulation. This relationship can help us understand why OTFS can gain both frequency and time diversity. Applying the same analysis to OFDM and SC-FDE, it is also seen why OFDM cannot exploit frequency diversity but SC-FDE can.

Based on $\gamma_{out}[m,n]$ and assuming QAM modulation for data symbols, the average BER probability P_b for a given channel realisation can be evaluated for various modulation levels [96][99][100]. Averaging over all possible fading channel realisations, the ergodic BER for the fast fading channel is expressed as $E_h\{P_b\}$, where $E_h\{\cdot\}$ denotes the ensemble average over all delay-Doppler channel realisations.

3.4 Simulation Results

In this section, the BER performance of the frequency domain MMSE equalisation is compared over fast fading channels among OTFS, OFDM and SC-FDE with uncoded 4-QAM modulation. The same ETSI TDL models are adopted as shown in Chapter 1 and the parameters can be found in Table 2.1. $M = 256$ and $N = 32$ are adopted as the delay and Doppler grids of OTFS, containing the same transmitted data in total as OFDM and SC-FDE but exploring full time diversity. The DFT and IDFT sizes for OFDM and SC-FDM are set as 256 equalling the number of subcarriers.

The simulated BER performance of OTFS, OFDM and SC-FDE in fast fading LOS channel is shown in Fig. 3.2. It is observed that systems with the proposed frequency domain MMSE equalisation perform significantly better than those with the conventional one-tap frequency domain equalisation method. The performance of OTFS is the best, achieving 10^{-4} BER at about 14 dB SNR. In comparison, at the same BER, SC-FDE has only less than 1 dB performance degradation, while OFDM has a large 4 dB degradation due to the lack of frequency diversity. It is also seen that the theoretical BER curves perfectly match the simulation results. Since a perfect CSI can not be achieved in practice, the performance when imperfect channel estimation is applied in the channel equalisation is also simulated. The imperfect channel is simulated by adding a random error matrix obeying zero-mean Gaussian distribution into the estimated channel matrix, where the variance of the channel error is assumed to be inversely proportional to the SNR [101]. The BERs of OTFS, OFDM and SC-FDE with practically imperfect CSI in the LOS channel are also shown in Fig. 3.2, labelled as OTFS (practical), OFDM (practical), and SC-FDE (practical) respectively. It is seen that the impact of channel estimation error on the performance is significant only at a lower SNR but tends to be minor at a higher SNR.

Fig. 3.3 shows the BER performance in fast fading NLOS channels. It is observed

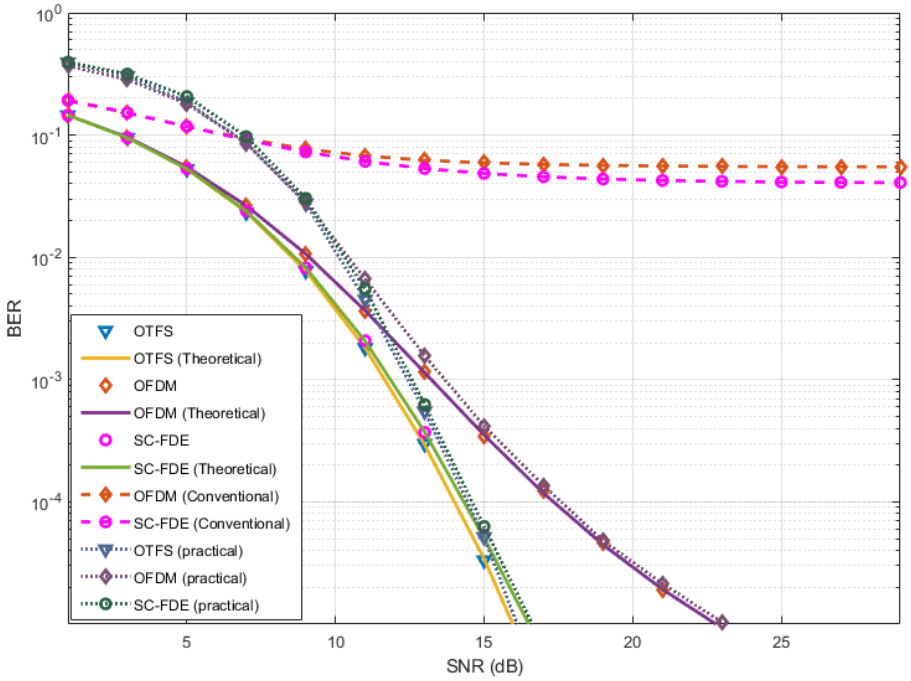

Figure 3.2: Performance comparison in LOS channel.

that OTFS performs much better than the other two. The performance of SC-FDE is degraded as compared with OTFS but is better than that of OFDM. Overall, the proposed MMSE equalisation improves the performance of OFDM and SC-FDE in fast fading channel significantly under both LOS and NLOS conditions. SC-FDE performs very well, especially in LOS channels. The impact of imperfect channel estimation on equalisation performance is also investigated in NLOS channel conditions and shown in Fig. 3.3, where the practical results demonstrate a similar trend as shown in the LOS channel. These results verify that the proposed equalisation algorithm is feasible for coping with fast fading channel in practice.

The effect of outdated CSI caused by user velocity variation is also considered. Assuming that the user velocity is 500 Km/h at the time of channel estimation and it changes at the time of signal detection, the outdated CSI is used to detect the received signal in LOS channel condition with 15 dB SNR and the results are shown in Fig. 3.4

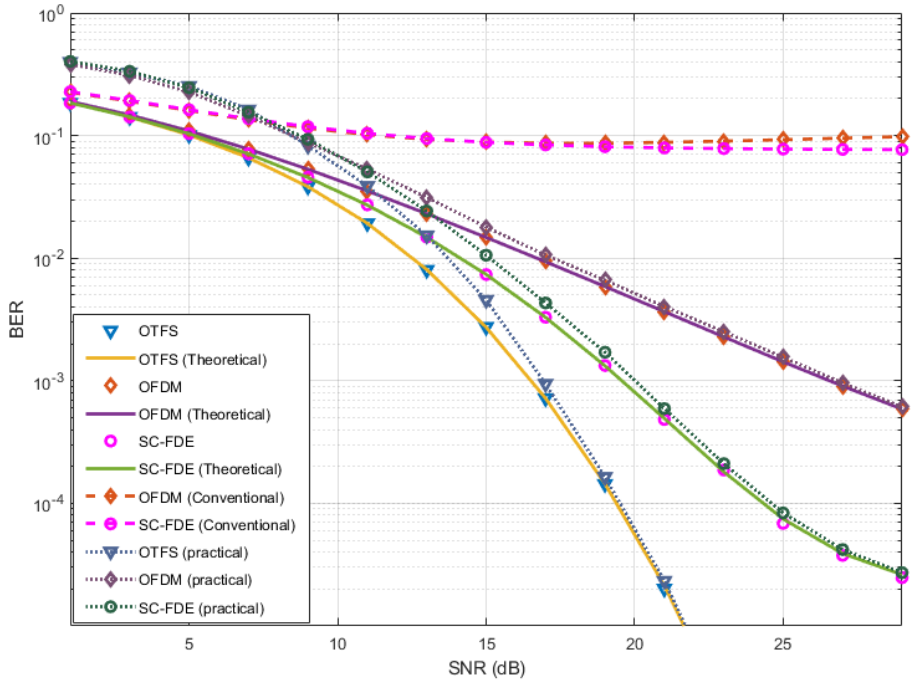

Figure 3.3: Performance comparison in NLOS channel.

as a BER versus velocity variation rate curve. For comparison, the BERs with perfect CSI at SNR = 7, 9, 11, and 13 dB are also plotted. It is seen that up to 2% variation in velocity can be tolerated with small BER increase. A further velocity variation will lead to significant performance degradation. For example, at ±3%, ±4% and ±5% velocity variations, the degradations are about 4 dB, 6 dB and 8 dB respectively. Therefore, an accurate and timely channel estimation is of significant importance for fast fading channels.

The proposed low-complexity frequency domain equalisation method is further compared with the popular MP algorithm proposed in [54]. Based on the same parameter settings, the BER performance over NLOS channels is simulated and compared. Note that the MP equalisation requires a number of iterations that affect both the computational complexity and the BER performance. The BER performance for MMSE and MP equalisation is compared in Fig. 3.5, where the number of iterations is selected as

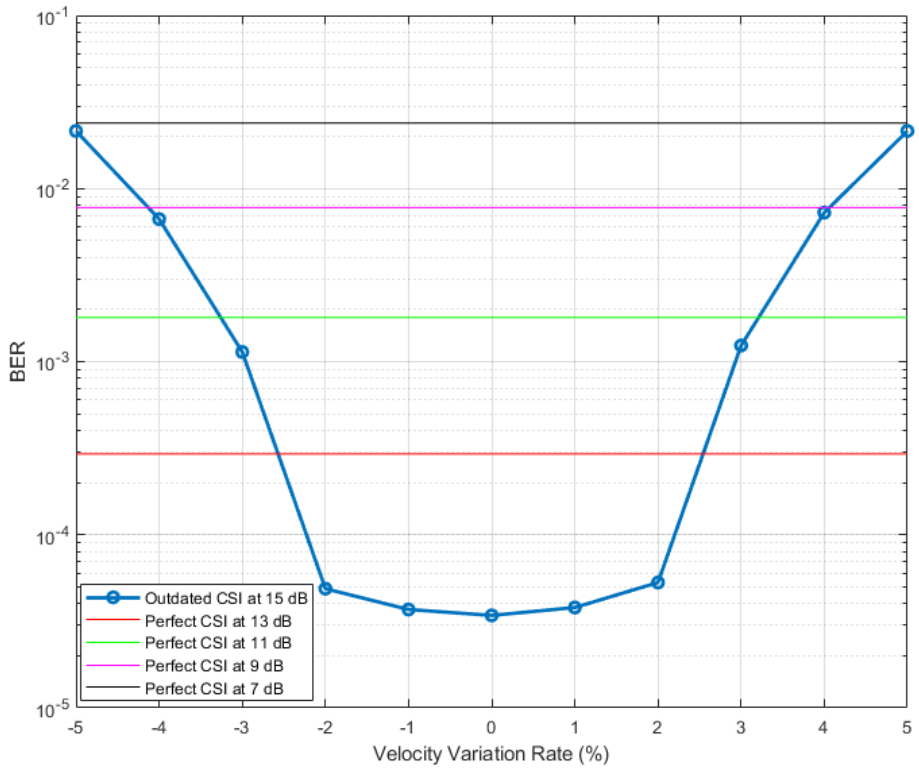

Figure 3.4: BER versus velocity variation rate for detection with outdated CSI in LOS channel at SNR = 15 dB.

10, 20, 30, 40 and 50 for MP equalisation. The BER performance under MP is better than that of MMSE in low SNR region. However, MMSE outperforms MP in high SNR region. It is also observed that there are error floors for MP even with a large number of iterations. To demonstrate the significant complexity reduction achieved by MMSE, the computational complexity is compared by counting the number of arithmetic operations (multiplication, division and logarithm). Under the ETSI NLOS channels shown in Table 2.1 with $K_{\max} = 3$ and $L_{\max} = 27$, the computational complexity for MMSE equalisation is around $O(169 \times MN)$, while the computational complexity for MP is around $O(2700 \times MN \times n_{iter})$, where n_{iter} is the number of iterations [53]. It is evident that the MMSE equalisation is superior to MP in terms of complexity and hence is more suitable for practical applications.

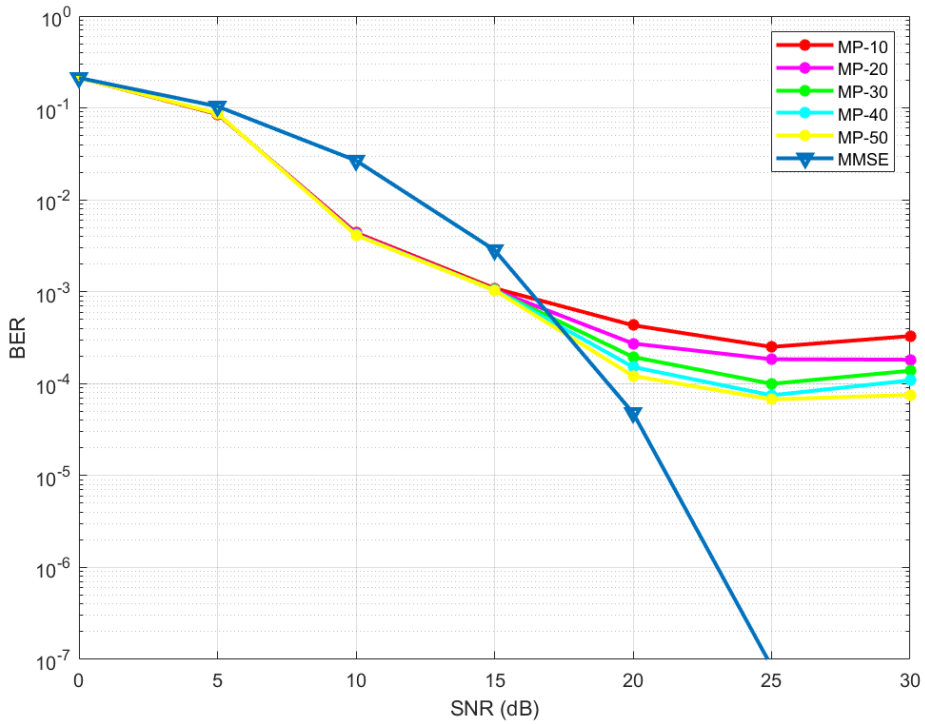

Figure 3.5: Performance comparison between MMSE and MP equalisations.

Finally, considering the impact of the channel coding on the performance, Fig. 3.6 shows a comparison among OTFS, OFDM, and SC-FDE with Low-density parity-check (LDPC) coding in LOS channel. The LDPC code with code rate 1/2 from the Digital Video Broadcasting standard DVB-S.2 is used [102, 103]. The block length of the code is 64,800. It is seen that the LDPC coding with code rate 1/2 significantly improves the performance of all the modulations and leads to similar BER performance. Though, with advanced channel coding, conventional modulations can produce competitive performance with OTFS, this is only achieved at the cost of significantly increased system overhead.

3.5 Conclusions

In this chapter, through formulating the frequency-Doppler channel matrix as a circular stripe diagonal matrix, it is demonstrated that low-complexity MMSE equalisation

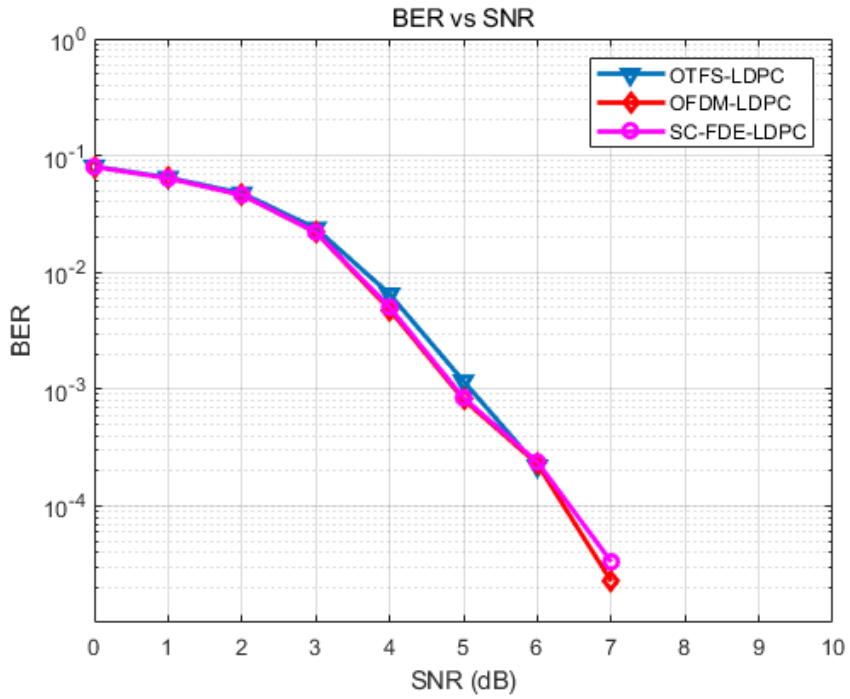

Figure 3.6: Performance comparison with LDPC coding.

becomes feasible for systems operating in fast fading channels. The signal models are also derived and the corresponding MMSE equalisation is proposed for the condition that the Doppler spread is partially-resolvable, which enables effective application of conventional modulations with short signal frames in fast fading channels. In addition, the theoretical equalisation performance is analysed via channel matrix eigenvalue decomposition, providing a useful tool for characterising the influence of channel conditions and signal modulations on the output SNR after equalisation. The simulated BER performance validates that the proposed MMSE equalisation can effectively exploit the time diversity with low complexity in fast fading channels for OTFS, OFDM and SC-FDE. The ability of achieving full time and frequency diversity makes OTFS outperform others. It is demonstrated that the performance of SC-FDE approaches that of OTFS since it can exploit full frequency diversity and partial time diversity, and OFDM performs the worst due to the lack of frequency diversity though partial time diversity can be achieved

with the proposed MMSE equalisation. The performance with imperfect channel estimation and outdated CSI is also simulated. All the results prove the feasibility of the proposed MMSE equalisation in practice. The methods proposed in this chapter provide efficient and effective means to overcome the challenge of system complexity caused by conventional iterative and time-domain equalisations.

CHAPTER 4

ADAPTIVE TRANSMISSION WITH FREQUENCY-DOMAIN PRECODING

4.1 Introduction and Literature Review

4.1.1 Existing Diversity Study of OTFS

Recent studies show that OTFS outperforms conventional modulations such as OFDM and SC-FDE through simulations and experiments in high-speed vehicular communication, underwater acoustic communications, mmWave communications, and radar systems [86, 87, 104–107]. However, the existing study on diversity performance and BER performance bounds are very limited [54–56, 67–71]. In [68], the authors show that the asymptotic diversity order of conventional OTFS for ideal bi-orthogonal waveforms is one and propose a phase rotation scheme for the OTFS to extract full diversity in the delay-Doppler domain. However, the authors in [90] indicate this analysis is not valid for practical waveforms and show that with sufficient parameter settings, the OTFS system can achieve full effective diversity without any precoding schemes. The performance bounds analysis is of significant importance for the transmission system

design and needs to be clarified. On the other hand, existing studies only indicate that OTFS can be regarded as adding precoding and postcoding processing to the conventional OFDM system without clear proof [68].

4.1.2 Chapter Structure

In this chapter, an adaptive transmission system is proposed based on frequency-domain precoding and MMSE equalisation, which can be used as a general solution to communicate over fast fading channels, including OTFS, and detailed performance analyses of it are conducted. Based on the representations of fast fading channels in different domains, the frequency-domain received signal model is adopted due to its concise stripe diagonal structure of the frequency-Doppler domain channel matrix. OTFS is first formulated as a more general precoded OFDM system so that the low-complexity frequency-domain approach can be applied to analyse its performance. Note that many conventional modulations can also be regarded as a kind of precoded OFDM, such as the SC-FDE. Although OTFS can achieve full diversity in both time and frequency domains using ML equalisation, the high complexity of ML algorithm makes it infeasible in practical applications. Therefore, the more practical frequency-domain MMSE equalisation with much lower computational complexity is introduced as demonstrated in Chapter 3. To optimise the system performance, the precoding matrix based on the eigenvalue decomposition of the channel matrix is designed so that an adaptive transmission system is obtained. Simulation results demonstrate that even with imperfect CSI feedback, the adaptive transmission still achieves better performance than OTFS evaluated under both 4-QAM and 16-QAM schemes. The BER lower bound and upper bound are also derived for the proposed adaptive transmission under two extreme channel conditions, taking into consideration of significantly large numbers of multipaths and Doppler frequency shifts.

4.2 OTFS as Precoded OFDM

In the original OTFS system, the data symbols after constellation mapping are arranged in a 2D $M \times N$ matrix $\mathbf{X}$ [38], where M denotes the number of elements in delay dimension, N denotes the number of elements in Doppler dimension, and $\mathbf{X} \in \mathbb{C}^{M \times N}$. In vector form, the data symbols to be transmitted can be expressed as $\mathbf{x} = \text{vec}(\mathbf{X})$. After ISFFT, Heisenberg transform and the pulse shaping, the time-domain signal is transmitted through the fast fading channel. Assuming the pulse shaping operation is a rectangular window function, the signal matrix to be sent into the channel can be expressed as

$$\mathbf{D} = \mathbf{F}_M^{\mathbf{H}}(\mathbf{F}_M \mathbf{X} \mathbf{F}_N^{\mathbf{H}}) = \mathbf{X}\mathbf{F}_N^{\mathbf{H}}, \tag{4.1}$$

where $\mathbf{D}$ is an $M \times N$ matrix, $\mathbf{F}_N$ denotes N-point FFT matrix [69]. The time-domain signal to be transmitted is the vectorised data matrix $\mathbf{D}$ expressed as

$$\mathbf{s} = \text{vec}(\mathbf{D}) = (\mathbf{F}_N^{\mathbf{H}} \otimes \mathbf{I}_M)\mathbf{x}, \tag{4.2}$$

where $\mathbf{s}$ is an $MN \times 1$ vector, $\otimes$ denotes Kronecker product.

It is seen that the transmitted signal frame of the original OTFS system with rectangular pause shaping can be constructed by applying N-point IDFT to the data matrix along Doppler dimension, which transforms the data matrix from DD domain to delay-time domain, and then vectorising it column-wise as shown in Fig. 4.1. Compared with traditional OFDM system, which applies IDFT to a whole data vector of length M, OTFS system applies an IDFT to every M spaced data set of length N.

From (2.22) and (4.2), the received frequency-domain signal can be expressed as

$$\mathbf{R} = \mathbf{H}_v \mathbf{F}_{MN}(\mathbf{F}_N^{\mathbf{H}} \otimes \mathbf{I}_M)\mathbf{x} + \mathbf{W}. \tag{4.3}$$

According to the Cooley-Tukey general factorisation, the MN-point DFT $\mathbf{F}_{MN}$ can be

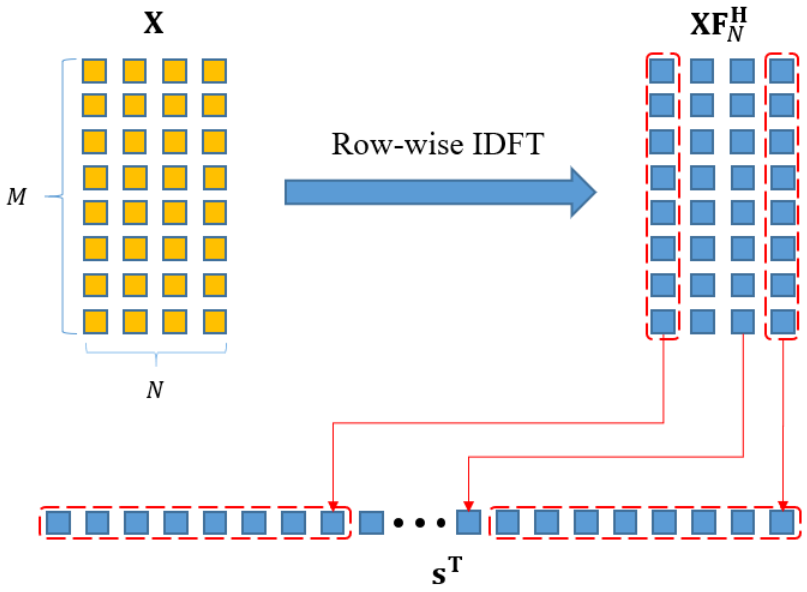

Figure 4.1: Time domain transmitted signal frame of original OTFS system.

factorised as two smaller DFTs in terms of sizes M and N, which can be expressed as

$$\mathbf{F}_{MN} = \mathbf{P}(\mathbf{I}_N \otimes \mathbf{F}_M)\text{diag}\{e^{-\mathbf{j}\frac{2\pi}{MN}(i)_M \lfloor \frac{i}{M} \rfloor}\}(\mathbf{F}_N \otimes \mathbf{I}_M), \tag{4.4}$$

where $(\cdot)_M$ denotes modulo M operation, $\lfloor \cdot \rfloor$ denotes flooring operation and $\mathbf{P}$ denotes a permutation matrix of dimension $MN \times MN$. The permutation matrix equivalently performs the interleaving operation that reads the elements in the matrix column-wise and stacks them to a matrix row-wise. Therefore, based on (4.3) and (4.4), the received frequency-domain signal becomes

$$\mathbf{R} = \mathbf{H}_v\mathbf{P}(\mathbf{I}_N \otimes \mathbf{F}_M)\text{diag}\{e^{-\mathbf{j}\frac{2\pi}{MN}(i)_M \lfloor \frac{i}{M} \rfloor}\}\mathbf{x} + \mathbf{W} \tag{4.5}$$

and the OTFS system can be transformed into a precoded OFDM system, where $(\mathbf{I}_N \otimes \mathbf{F}_M)$ is the precoding matrix, which is also an unitary matrix, and $\tilde{\mathbf{x}} = \text{diag}\{e^{-\mathbf{j}\frac{2\pi}{MN}(i)_M \lfloor \frac{i}{M} \rfloor}\}\mathbf{x}$ is the twiddled signal vector. Note that the twiddling will only affect the phase of the symbol, and will not affect the signal detection or the BER performance after de-twiddling at the receiver. Therefore, the construction of a precoded OFDM transmitted signal frame in the frequency domain is shown in Fig. 4.2. The precoding process is achieved by applying

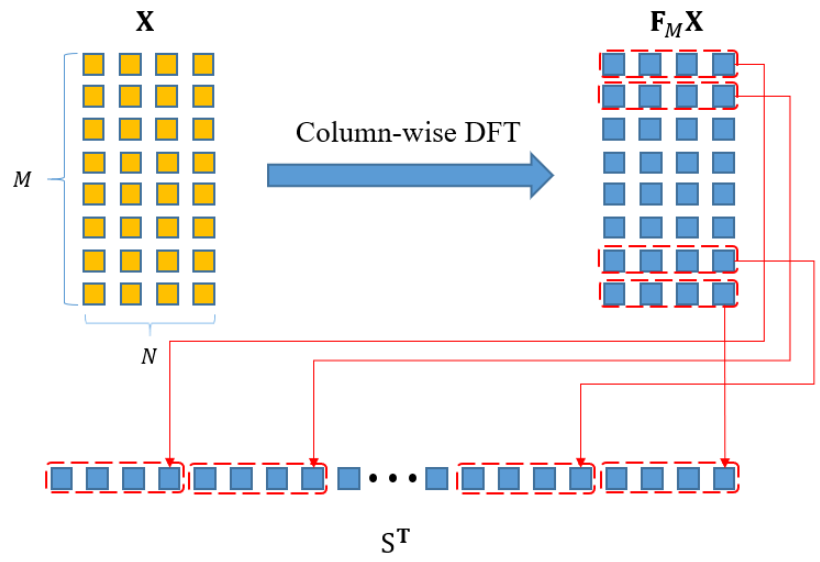

Figure 4.2: Frequency domain transmitted signal frame of OTFS as precoded OFDM form.

M-point DFT to every column of the data matrix, and it also transforms the data matrix from DD domain to frequency-Doppler domain. After interleaving, i.e., taking out data symbols from the precoded data matrix row-wise, the frequency domain transmitted signal frame is formed.

Excluding the twiddling at the transmitter and the de-twiddling at the receiver, Fig. 4.3 shows a typical precoded OFDM system [96]. The similarity between these two modulations allows us to use well-developed methods in the diversity and performance bound analyses, which can be equally applied to both OTFS and precoded OFDM. Note that the precoded OFDM has demonstrated superb frequency diversity over frequency-selective slow fading channels in previous research works, but its performance over fast fading channels has not been explored yet. The analysis in the following section will show that the precoded OFDM, or similarly the OTFS, is also capable of achieving full time diversity.

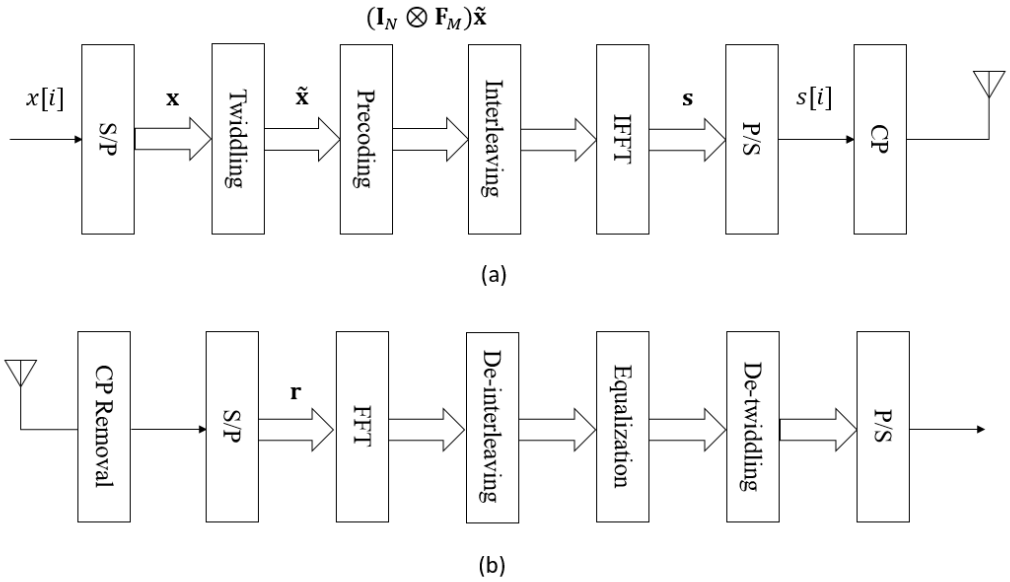

Figure 4.3: OTFS system block diagram in precoded OFDM form: (a) transmitter and (b) receiver. S/P and P/S stand for serial-to-parallel and parallel-to-serial conversions respectively, and CP stands for cyclic prefix.

4.3 Diversity with ML Equalisation

To recover the signal at the receiver, two main categories of equalisation techniques can be adopted. The first class is the maximum likelihood sequence estimation (MLSE), which is based on Viterbi algorithm and the Maximum *A Posteriori* Probability (MAP) detection. It is the optimal equalisation method to recover the corrupted signals, but it has significant computational complexity exponential to the channel memory length. The second class is the linear equalisation such as zero forcing (ZF) and MMSE, which has much lower complexity but the performance is also degraded. The performance analysis for linear equalisation can be found in previous Chapter 3.3, and the diversity analysis for ML equalisation is demonstrated in this section.

Assuming the CSI is perfectly known at the receiver, the ML estimate of the data

symbol $\mathbf{x}$ can be obtained by minimising

$$(\mathbf{R}-\mathbf{H}_v\mathbf{F}_{MN}(\mathbf{F}_N^{\mathbf{H}}\otimes\mathbf{I}_M)\hat{\mathbf{x}})^{\mathbf{H}}(\mathbf{R}-\mathbf{H}_v\mathbf{F}_{MN}(\mathbf{F}_N^{\mathbf{H}}\otimes\mathbf{I}_M)\hat{\mathbf{x}}), \tag{4.6}$$

through exhaustive search from all possible data vectors $\hat{\mathbf{x}}$ [99]. The results in [68, 70, 90] show that OTFS can achieve full diversity through symbol rotation. Here, the diversity from another perspective is characterised. Assuming the received signal in the time-domain at the receiver is $\mathbf{y}$, the received SNR through separately analysing the signal and noise powers in $\mathbf{E}\{\mathbf{y}\mathbf{y}^{\mathbf{H}}\}$ can be obtained. Except for a constant scaling factor, the received SNR can be expressed as

$$\gamma \propto \sum_{l=0}^{L-1}\sum_{k=-K_{\max}}^{K_{\max}} |h[l,k]|^2 \cdot \frac{\sigma_s^2}{\sigma_w^2}. \tag{4.7}$$

where σ_s^2 is the transmitted signal power, σ_w^2 is the noise power, $h[l,k]$ is the discrete-time form of $h(\tau,\nu)$, sampled at $\tau = ld_r$ and $\nu = kf_r$ for $l = 0,1,...,L-1$, $k = -K_{\max},...,K_{\max}$. The derivation is provided in Appendix B.

Therefore, the received SNR is proportional to the sum of $L\times(2K_{\max}+1)$ random variables $|h[l,k]|^2$, from which it can be deduced that OTFS has the potential to achieve full diversity in both time and frequency domain if all the random variables are independent.

4.4 Adaptive Transmission and BER Bounds

Based on previous diversity analysis in chapter 4.3, although MLSE equalisation can achieve optimal performance, its complexity restricts its practical application [108]. Since linear equalisation can be implemented with low complexity in the frequency-domain, it is preferable in practice. In this section, a novel adaptive transmission scheme is proposed based on frequency-domain precoding and MMSE equalisation. Then, the BER upper and lower bounds are analysed under different extreme channel conditions.

4.4.1 Adaptive Transmission

As can be seen from Eq.(3.20), after frequency-domain MMSE equalisation, the normalised noise power for each data symbol is generally different from each other and affected by the modulation matrix $\mathbf{V}$ and the unitary matrix $\mathbf{Q}$ obtained from channel matrix eigenvalue decomposition. Assuming that the CSI can be fed-back to the transmitter, the modulation matrix $\mathbf{V}$ based on the channel conditions can adaptively be determined to reduce the normalised noise power and hence the output SNR of the equalisation can be improved, resulting in an adaptive transmission system. This can be achieved by constructing the modulation matrix $\mathbf{V}$ such that $\mathbf{U}$ satisfies

$$|\mathbf{U}[nM+m,i]|^2 = \frac{1}{MN}, \tag{4.8}$$

and the normalised noise power for the equalised data symbol becomes

$$J = \frac{1}{MN}\sum_{i=0}^{MN-1}\frac{1}{\gamma_{in}\lambda_i+1}, \tag{4.9}$$

which is the same for all the data symbols. Therefore, the optimised output SNR can be simplified as

$$\gamma_{out}^{*} = \frac{1}{\frac{1}{MN}\sum_{i=0}^{MN-1}\frac{1}{\gamma_{in}\lambda_i+1}} - 1. \tag{4.10}$$

For a general precoded OFDM system, Eqs. (3.20) and (3.21) show that the output SNR is related to the input SNR, eigenvalues of the channel, and the parameter $\mathbf{U}$, which can be affected by the modulation method $\mathbf{V}$ and unitary matrix $\mathbf{Q}$ of the channel. However, after applying the adaptive transmission, $\mathbf{U}$ is transformed to an IFFT matrix with constant magnitude elements as shown in (4.8), and the output SNR is simplified as shown in (4.10). Under this adaptive modulation, only the input SNR and eigenvalues of the channel can affect the output SNR. Moreover, note that the denominator of (4.10) is a sum of $\frac{1}{\gamma_{in}\lambda_i+1}$, because MMSE equaliser instead of zero forcing is used here. Even if some

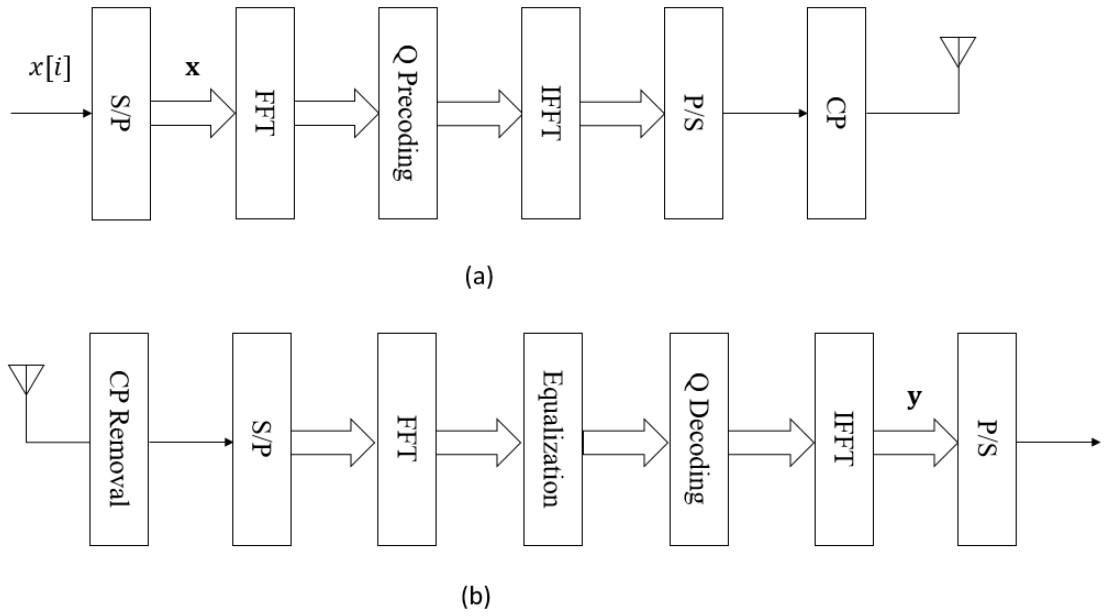

Figure 4.4: Adaptive transmission system block diagram: transmitter (a) and receiver (b).

channels have some zero eigenvalues, no singularity will happen and the performance will not break down. Therefore, the adaptive transmission is feasible under all channel conditions.

Letting $\mathbf{V} = \mathbf{F}_{MN}^{\mathbf{H}} \mathbf{Q} \mathbf{F}_{MN}$ and substituting it into $\mathbf{U}$, we have

$$\mathbf{U} = \mathbf{F}_{MN}^{\mathbf{H}} \mathbf{Q}^{\mathbf{H}} \mathbf{F}_{MN} \mathbf{F}_{MN}^{\mathbf{H}} \mathbf{Q} = \mathbf{F}_{MN}^{\mathbf{H}}, \tag{4.11}$$

and hence the condition (4.8) is satisfied. Therefore, the adaptive transmission system can be designed as shown in Fig. 4.4.

At the transmitter of the adaptive transmission, a sequence of data symbols $x[i]$, $i = 0, 1, ..., MN-1$ is converted to a vector $\mathbf{x}$ via S/P. After transforming $\mathbf{x}$ into the frequency-domain by FFT, the frequency-domain symbol vector is precoded by the eigenvector matrix $\mathbf{Q}$. After converting the frequency-domain precoded symbol vector to time-domain by IFFT and appending the cyclic prefix (CP), the data symbol frame is sent over the fast fading channel. At the receiver, after the CP removal and channel estimation, the

CSI is fed-back to the transmitter and the received signal is recovered by the MMSE equalisation. The recovered frequency-domain symbol vector can be expressed as

$$\mathbf{Y} = \mathbf{Q}^{\mathbf{H}}\mathbf{G}_v\mathbf{H}_v\mathbf{Q}\mathbf{X} + \mathbf{Q}^{\mathbf{H}}\mathbf{G}_v\mathbf{W}, \tag{4.12}$$

which indicates that the adaptive transmission system performs all the precoding, equalisation and decoding processes in the frequency-domain. Hence, the proposed adaptive transmission system is a kind of adaptive precoded OFDM system.

Since the output SNR of each data becomes the same with adaptive transmission, the BER can be simplified as

$$P_b = E_h\{\frac{2(1-2^{-k})}{k}Q(\sqrt{\frac{3}{4^k-1}\gamma^*_{out}})\}, \tag{4.13}$$

where the Q-function is defined as $Q(x) = \frac{1}{\sqrt{2\pi}}\int_x^\infty e^{-\frac{t^2}{2}}dt$ and 2^{2k} indicates the modulation level.

4.4.2 BER Bounds and Analysis

The performance bounds for the adaptive transmission scheme are obtained analytically in this section under some extreme channel conditions with respect to the number of multipaths and maximum Doppler frequency shift.

4.4.2.1 Lower Bound

The first extreme channel condition is set as a channel with a fixed Doppler frequency shift in every multipaths, which can be regarded as a slow fading channel after the Doppler frequency shift is compensated. For such a channel, the time-domain channel matrix is a circulant matrix and can be transformed into diagonal matrix in the frequency-domain by 2D FT, which can be expressed as

$$\mathbf{H}_v = \mathbf{F}^{\mathbf{H}}_{MN}\text{diag}\{\alpha_i\}\mathbf{F}_{MN}, \tag{4.14}$$

where α_i, $i = 0, 1, ..., MN-1$, denotes the fading coefficient at frequency bin i. Then, we can obtain

$$\Lambda = \text{diag}\{\lambda_i\} = \text{diag}\{\alpha_i\}^{\mathbf{H}}\text{diag}\{\alpha_i\} = \text{diag}\{|\alpha_i|^2\}. \tag{4.15}$$

Assuming that all multipaths are independent, α_i are zero-mean independent complex Gaussian variables. When P approaches infinity, $\lambda_i = |\alpha_i|^2$ obeys the Chi-square distribution with two degrees of freedom and the probability density function (PDF) $e^{-\rho}$. In this condition, the normalised noise power for the equalised data symbol in the adaptive transmission can be evaluated from (4.9) as

$$J_{low} = \int_0^{\infty} \frac{e^{-\rho}}{\gamma_{in}\rho + 1}\, d\rho = E_1(\frac{1}{\gamma_{in}})e^{\frac{1}{\gamma_{in}}}, \tag{4.16}$$

where $E_1\{\cdot\}$ is the exponential integral function, which is defined as

$$E_1(z) = \int_z^{\infty} \frac{e^{-t}}{t}\, dt. \tag{4.17}$$

The output SNR can be expressed as

$$\begin{aligned} \gamma_{low} &= \frac{1}{J_{low}} - 1 \\ &= \frac{\gamma_{in}}{E_1(\frac{1}{\gamma_{in}})e^{\frac{1}{\gamma_{in}}}} - 1, \end{aligned} \tag{4.18}$$

Thus, the lower bound of the BER performance can be obtained as

$$P_{b,low} = Q\left(\sqrt{\frac{\gamma_{in}}{E_1(\frac{1}{\gamma_{in}})e^{\frac{1}{\gamma_{in}}}} - 1}\right). \tag{4.19}$$

4.4.2.2 Upper Bound

The second extreme channel condition considers the case when Doppler frequencies are uniformly distributed over $[-K_{\max}, K_{\max}]$, and $K_{\max} \to \infty$. Supposing that there are a

large number of multipaths in the channel, the channel matrix in the frequency-domain $\mathbf{H}_v$ becomes a random matrix, whose entries obey independent Gaussian distribution with zero mean and unit variance. Therefore, the entries of the Hermitian matrix $\mathbf{H}_v^{\mathbf{H}}\mathbf{H}_v$ obey the complex Wishart distribution. The eigenvalues of $\mathbf{H}_v^{\mathbf{H}}\mathbf{H}_v$ have a PDF $\frac{1}{2\pi}\sqrt{\frac{4-\rho}{\rho}}$, $0 \leqslant \rho \leqslant 4$. Under this condition, the normalised noise power for the equalised data symbol under the adaptive transmission can be expressed as

$$\begin{aligned} J_{up} &= \int_0^4 \frac{\frac{1}{2\pi}\sqrt{\frac{4-\rho}{\rho}}}{\gamma_{in}\rho+1}\, d\rho \\ &= \frac{\sqrt{4\gamma_{in}+1}-1}{2\gamma_{in}}, \end{aligned} \tag{4.20}$$

and the output SNR can be expressed as

$$\begin{aligned} \gamma_{up} &= \frac{1}{J_{up}} - 1 \\ &= \frac{2\gamma_{in}}{\sqrt{4\gamma_{in}+1}-1} - 1. \end{aligned} \tag{4.21}$$

The upper bound of the BER performance can be obtained as

$$P_{b,up} = Q\left(\sqrt{\frac{2\gamma_{in}}{\sqrt{4\gamma_{in}+1}-1} - 1}\right). \tag{4.22}$$

It is known that the system performance and diversity orders in fast fading channels depend on the number of multipaths and the maximum Doppler frequency shift. For the OTFS modulation, it is hard to derive a closed-form expression of the BER performance based on MMSE equalisation given arbitrary numbers of multipaths and Doppler frequency shifts. However, for the proposed adaptive transmission, the theoretical BER bounds are available because the precoding $\mathbf{Q}$ matrix can simplify the channel matrix into a diagonal matrix. After applying an asymptotic method under the conditions that some system parameters are set to extreme values, the adaptive transmission can be adopted to verify the theoretical limits of a general precoded OFDM system with MMSE

equalisation in fast fading channels. The diversity analysis based on other detection methods and waveforms is out of the scope of this thesis and will be included in future work.

4.5 Simulation Results

4.5.1 Adaptive Transmission Performance and Comparison

Firstly, let us compare the performance of adaptive transmission with OTFS, named as Adaptive-long in the simulation, and other conventional modulations. Here, the TDL channel models recommended by ETSI are still adopted. All the parameters are listed in Table 2.1. Both short and long frame transmissions are compared. When adaptive transmission is applied with short frames, it is named as Adaptive-short in the simulation. For long-frame modulations, including OTFS and Adaptive-long, there are MN data symbols in one frame. For short-frame modulations, including OFDM, SC-FDE and Adaptive-short, there are M data symbols in one frame.

The performance comparison is made based on the simulated BERs for different modulations under the above described LOS and NLOS channel conditions with fast fading. For each realisation of the fast fading channel, a sufficient number of signal frames are generated with the specified modulation. After passing through the channel, the received signals are corrupted by AWGN according to a given SNR level. With perfect synchronisation and known CSI, frequency-domain MMSE equalisation is then performed using the equalisation matrix defined in (3.4). The detected information bits are compared with the transmitted ones and the number of error bits are recorded. After 1000 iterations of random channel realisations, the average BER is finally obtained.

Fig. 4.5 shows the BER performance in LOS channel with 4-QAM data symbol mapping. Note that OTFS and Adaptive-long demonstrate similar performance, achieving 10^{-7} BER at SNR around 17 dB. SC-FDE and Adaptive-short incur about 2 dB

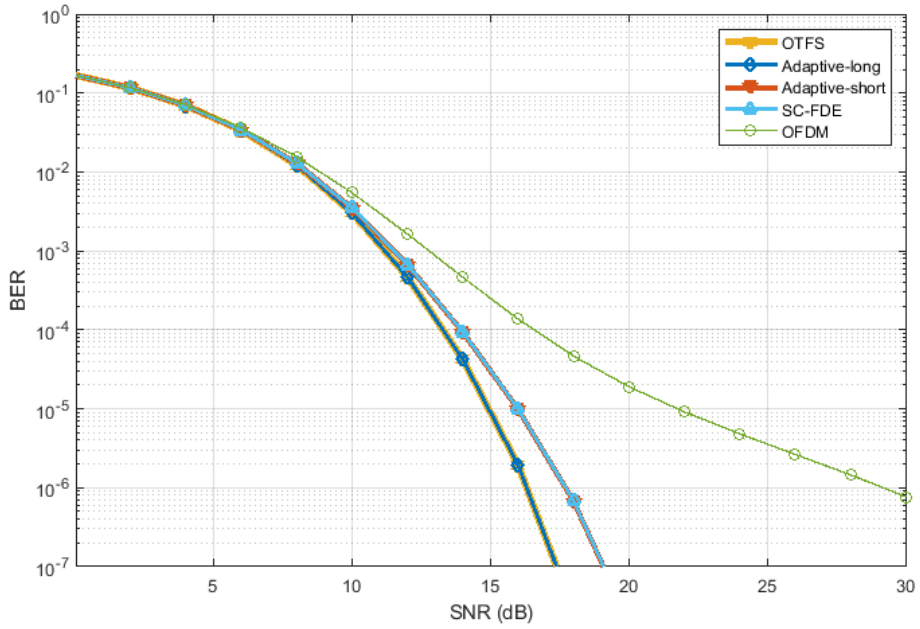

Figure 4.5: Comparison of various modulation schemes in LOS channels using 4-QAM.

degradation. OFDM shows the worst performance, lagging far behind others.

Fig. 4.6 shows the BER performance in NLOS channels with 4-QAM data symbol mapping. Let's first compare different modulations with perfectly known CSI (legends with prefix "P-"). It is seen that P-Adaptive-long demonstrates the best performance and achieves 10^{-7} BER at SNR about 24 dB, outperforming OTFS by about 4 dB. For the short frame modulations, although the P-Adaptive-short performs worse than long frame modulations, it can still achieve a BER of 10^{-7} at about 30 dB and is much better than SC-FDE and OFDM.

To prove that adaptive transmission is effective in practice, simulations are also conducted with CSI not perfectly known at the receiver (legends with prefix "I-"). In doing so, a random matrix obeying Gaussian distribution for each element is added into the estimated channel matrix [109]. Assuming the variance of channel error is inversely proportional to the SNR, both Adaptive-long and OTFS, denoted as I-Adaptive-long and I-OTFS, are simulated and the results are shown in Fig. 4.6. It is observed that the

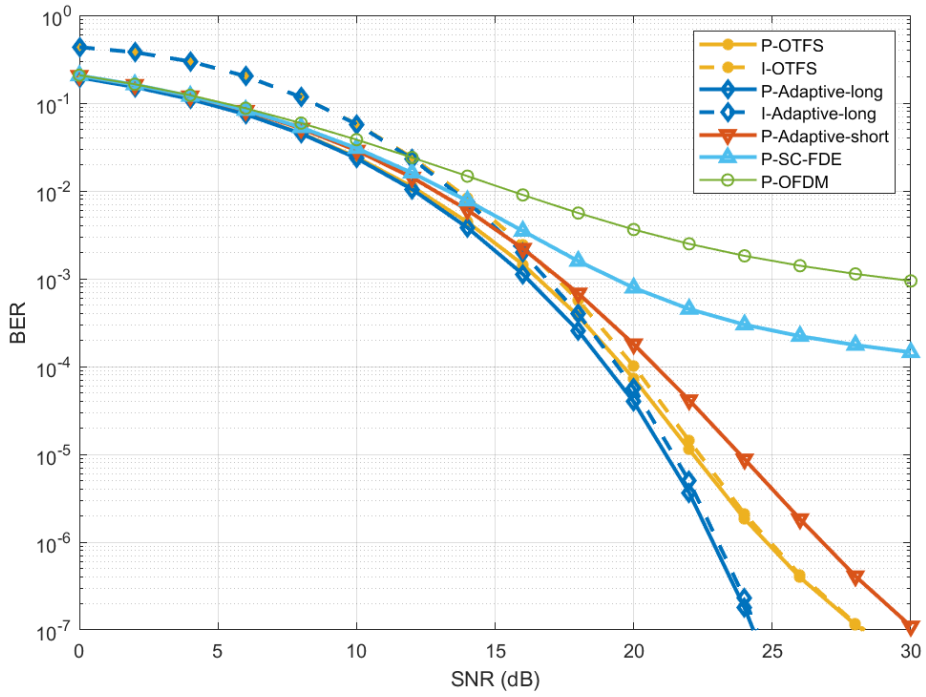

Figure 4.6: Comparison of various modulation schemes with and without channel estimation error in NLOS channels using 4-QAM.

impact of channel estimation error on the performance is significant in a lower SNR region but tends to be minor in a higher SNR region. Moreover, adaptive transmission keeps showing better performance than OTFS.

It is worthwhile noting that, in LOS channels, SC-FDE and Adaptive-short show very close performance to long-frame modulations. In NLOS channels, with the help of precoding, the short-frame adaptive transmission demonstrates much better performance than short-frame modulations, close to those of long-frame modulations. This result confirms that the adaptive precoding can indeed improve the performance of short-frame modulations, and the adaptive transmission with short frames provides a practical solution considering its low complexity and short delay in signal processing.

The results in Figs. 4.5 and 4.6 also show how the BER performance is impacted by diversities in different domains. Firstly, long-frame modulations can exploit both time

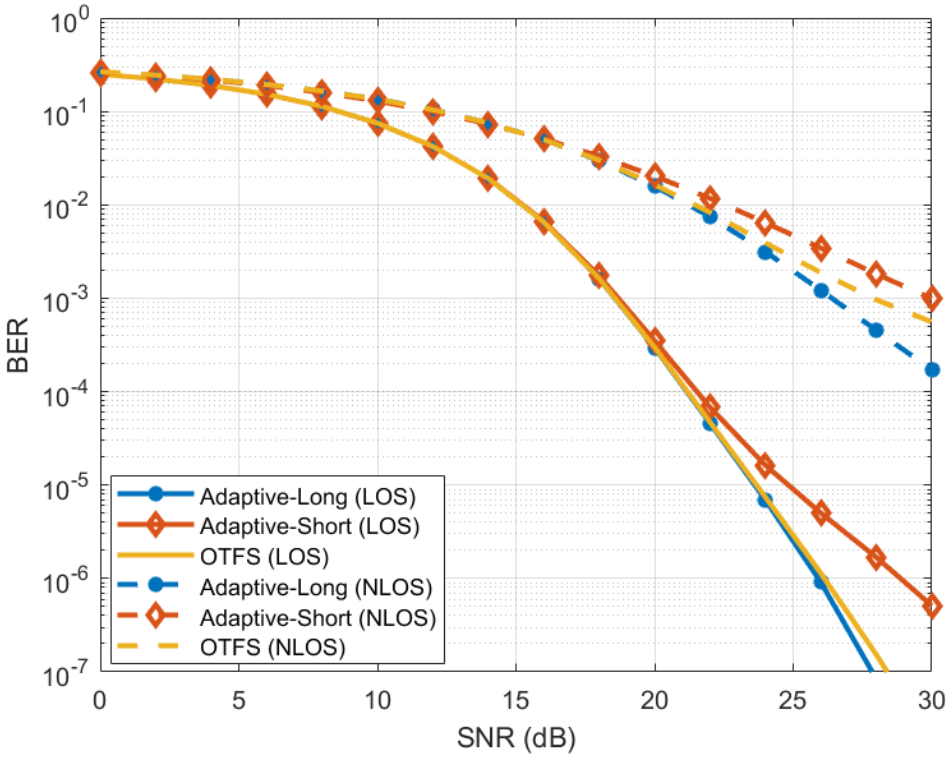

Figure 4.7: Comparison of various modulation schemes with 16-QAM under both LOS and NLOS channels.

and frequency diversity so that they achieve the best performance. Then, SC-FDE can exploit frequency diversity but only partially resolve the Doppler frequency so that it shows degraded performance. Finally, conventional OFDM without precoding can not exploit frequency diversity so that it shows the worst performance.

The BER performance for 16-QAM is also simulated to verify the effect of precoding. As shown in Fig. 4.7, the adaptive transmission and OTFS modulations with 16-QAM demonstrate similar trends to those with 4-QAM in both LOS and NLOS channels. Therefore, the proposed adaptive transmission is also an effective solution to combating fast fading channels for signals with higher order modulation levels.

The PAPRs of the OTFS with and without precoding are also simulated. The results show that the OTFS without precoding has lower PAPR than OFDM and the adaptive

transmission. The PAPRs of the adaptive transmission and OFDM are very similar, and are only about 0.5 dB higher than that of OTFS, when the probability of PAPR greater than a specified threshold is 10^{-5}. It proves that the impact of precoding on PAPR performance is negligible.

4.5.2 BER Bound Validation

After the performance of the adaptive transmission is verified, we now validate the BER upper and lower bounds using MMSE equalisation. The BER bounds between adaptive transmission and OTFS are compared under some extreme channel conditions. We adopt larger P or $K_{\max}$ in these simulations and assume that the channel has equal-power for each multipath, while other parameters remain the same as in Table 2.1. To consider more practical conditions, the ETSI channel models are used as described in Section 4.5.1, which have relatively smaller P.

Fig. 4.8 shows the BER performance comparison under varying multipath diversity orders. It is observed that the performance is improved as P increases. When $P \to \infty$, the performance of adaptive transmission converges towards the theoretical lower bound, which achieve 10^{-7} BER at SNR about 20.5 dB. The OTFS curves nearly overlap with those of the adaptive transmission when P is small, but gaps appear as P becomes large.

Fig. 4.9 shows the BER performance comparison under varying Doppler frequency shifts with $K_{\max} = 1, 4, 64$, and ∞ when P is set to MN. It is well-known that the diversity performance is represented by the slope of the BER performance curve when the SNR tends to infinity. After enlarging the SNR range, it can be seen from Fig. 4.10 that the diversity orders of adaptive transmission increase as $K_{\max}$ increases. However, this does not mean that the actual BERs will be reduced in a low SNR region as the diversity order increases. In fact, from Fig. 4.9, the BER performance under smaller Doppler diversity orders is superior to those with larger Doppler diversity orders in a low SNR region. Considering the more practical BER comparison in a low SNR region, the term upper

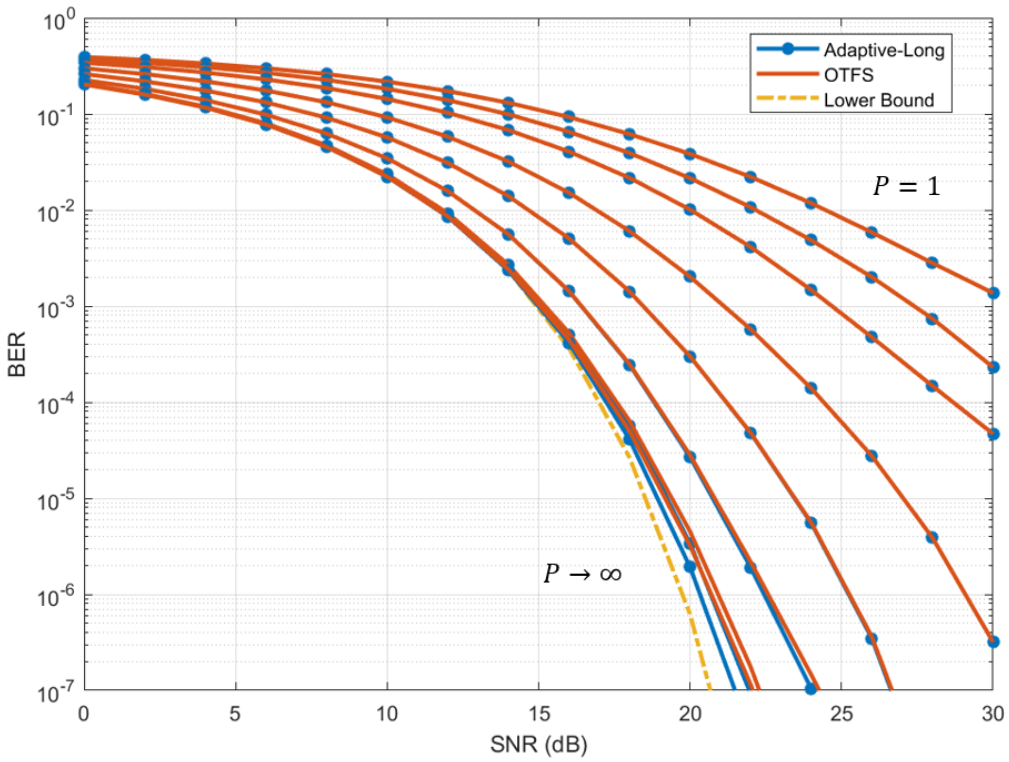

Figure 4.8: Lower bounds of MMSE equalisation performance under different multipath diversity orders without Doppler frequency shifts. The curves from right to left correspond to $P = 1, 2, 4, 8, 16, 32, 64, 128, 1024$, and asymptotic ∞.

bound is still used to describe the BER performance when $K_{\max} \to \infty$, though the Doppler diversity is not upper bounded by it. Above simulation results reveal a very interesting property of the adaptive transmission in terms of the relationship between Doppler diversity order and BER performance, which has never been found in the literature.

Note that in a practical channel condition the number of multipaths or the maximum Doppler frequency shift will not be infinite but the analytical performance bounds can serve as benchmarks for practical system design. In some application scenarios, the number of multipaths can be very large, such as in the urban macro (UMa) channel. In the emerging ISTNs which involve aircraft-to-aircraft and aircraft-to-ground communications, the Doppler frequency shift can also be very large. Therefore, the analysis of BER bounds is of great significance.

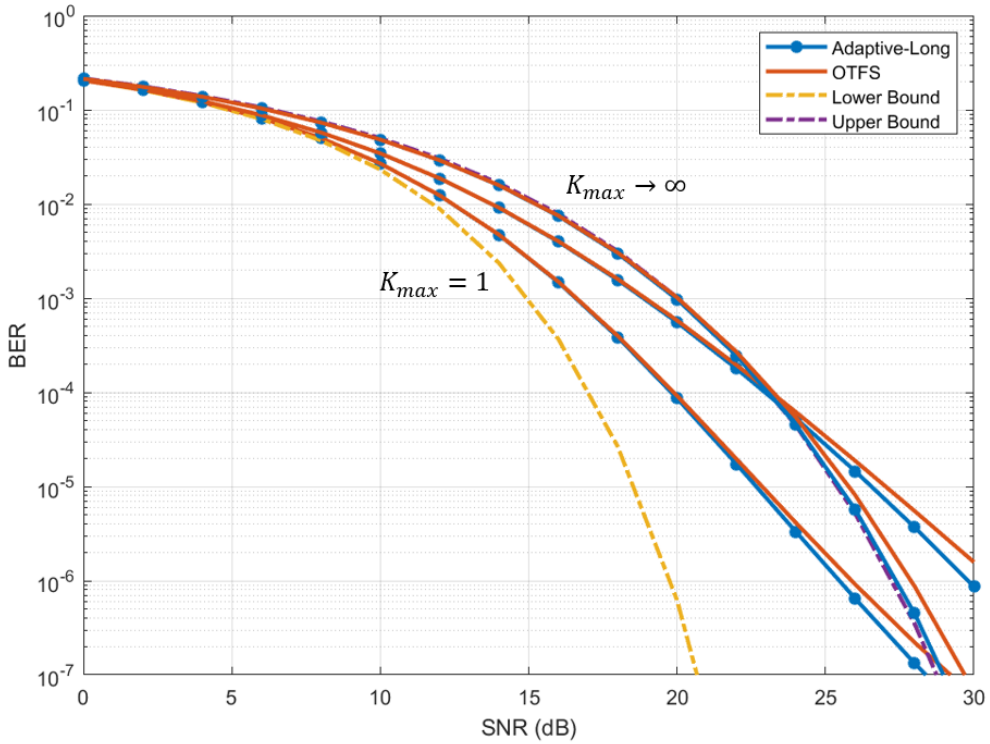

Figure 4.9: Upper bounds of MMSE equalisation performance under different Doppler frequency diversity orders with $P = M \times N$. The curves from left to right correspond to $K_{\max} = 1, 4, 64$, and asymptotic ∞.

Overall, although the performance of the two techniques are very close, the proposed adaptive transmission is superior to OTFS under all simulated conditions. It also proves that OTFS can achieve almost optimal performance in fast fading channels. Though the lower and upper bounds are derived for the proposed adaptive transmission, they can also serve as the performance benchmarks for OTFS systems.

4.6 Conclusions

In this chapter, OTFS is formulated as a precoded OFDM and frequency-domain channel models are applied to analyse its diversity performance in fast fading channels. With low complexity MMSE equalisation, an adaptive transmission scheme is proposed to optimise the diversity performance. Two BER bounds are derived by considering two

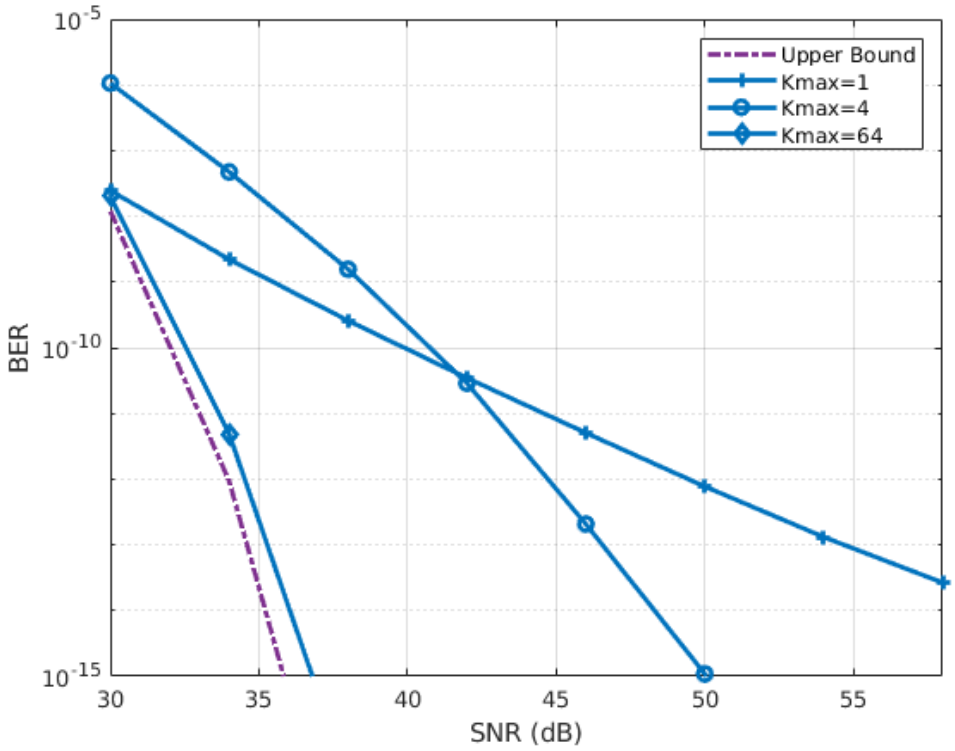

Figure 4.10: BER comparison under adaptive transmission when $K_{\max} = 1, 4, 16, 64$ in high SNR region.

extreme channel conditions. These bounds can serve as the benchmarks for OTFS and adaptive transmission systems. The simulation results show that the adaptive transmission achieves the best performance in fast fading channels. It is also demonstrated that the proposed adaptive transmission is very effective for short signal frames and is robust to channel estimation errors. The research conducted in this chapter provides an effect way to overcome the challenge of diversity performance analysis over fast fading channels for OTFS and general precoded OFDM systems.

CHAPTER 5

LOW-OVERHEAD OTFS TRANSMISSION WITH FREQUENCY OR TIME DOMAIN CHANNEL ESTIMATION

5.1 Introduction and Literature Review

5.1.1 Existing Channel Estimation techniques of OTFS

As a prerequisite for equalisation, an accurate channel estimation is very important to any transmission system. Current channel estimation techniques mainly adopt pilot-aided schemes to obtain the CSI at the receiver [5]. For OTFS transmission, an embedded pilot-aided channel estimation scheme is proposed in [91], by which pilot with surrounding zero guard symbols are embedded in the delay-Doppler domain. The overhead of this scheme is proportional to the product of the maximum normalised delay and Doppler shift in the channel. This scheme benefits from the sparse delay-Doppler channels but has some limitations in channels with multiple resolvable Doppler frequencies. Other works also use different pilot patterns and employ various techniques such as pseudo-random noise sequence pilots [94], sparse Bayesian learning algorithm [110], and MMSE method [111] to achieve a balance between performance and complexity. Based

on the embedded pilot-aided scheme [91], compressive sensing technique is adopted in [93] to simplify and solve the channel estimation problem for the MIMO OTFS system.

The channel estimation techniques mentioned above are based on the delay-Doppler domain pilot insertion because the original OTFS transmitted signal is conventionally considered as delay-Doppler modulated followed by ISFFT and time domain pulse shaping [38]. The channel estimation with delay-Doppler domain pilots is indeed accomplished effectively under sparse channel conditions. However, for a more general communication environment involving a large number of scattering objects, the delay-Doppler channel is no longer sparse and should be treated as a continuous-Doppler-spread channel (CDSC) [112]. Under such conditions, estimation techniques in other domains may achieve better overall performance, for which the existing study is very limited. Developing an effective and low-overhead channel estimation technique under more general channel scenarios is of significant importance for practical applications.

5.1.2 Chapter Structure

In this chapter, three variants are proposed to the conventional OTFS transmission, which enable lower signalling overhead and processing complexity, while achieving similar receiver performance. These variants are frequency-domain pilot aided (FD-PA) OTFS, time-domain pilot aided (TD-PA) OTFS, and time-domain training sequence (TD-TS) OTFS. They place pilots/training sequences and conduct channel estimation in either frequency or time domain, rather than in the conventional delay-Doppler domain for OTFS. Transmission frame construction methods and channel estimation algorithms for FD-PA-OTFS, TD-PA-OTFS, and TD-TS-OTFS are presented, followed by theoretical MSE analyses over fast fading channels. Finally, performance comparisons among different channel estimation schemes are provided.

5.2 OTFS Variants and Channel Estimation

In this section, the frequency and time domain pilot-aided OTFS variants, FD-PA-OTFS and TD-PA-OTFS, and their associated channel estimation methods are first proposed. To solve the PAPR problem with the time domain pilot-aided scheme, a time domain training sequence aided scheme, i.e., TD-TS-OTFS, is further proposed if time domain channel estimation is preferable for some applications.

5.2.1 Frequency-Domain Pilot-Aided Scheme

Let's start with frequency domain pilot design for FD-PA-OTFS transmission and then propose associated channel estimation method.

5.2.1.1 Pilot Design in Frequency Domain

With the maximum number of resolvable multipaths $L_{\max}$ and Doppler spread $K_{\max}$, $M_1 \geq L_{\max}+1$ pilot sections in the frequency domain must be inserted, each comprising $4K_{\max}+1$ frequency bins. The total number of frequency bins used for channel estimation is thus $M_1(4K_{\max}+1)$. Assuming that the length of frequency domain transmission frame is still MN, the number of precoded data symbols should be $MN - M_1(4K_{\max}+1)$, which can be represented by an M_1 by N_1 matrix $\mathbf{S}_{data}$ where $N_1 = MN/M_1 - (4K_{\max}+1)$.

The precoded data matrix $\mathbf{S}_{data}$ can be formed by reshaping the data vector of length M_1N_1 into an M_1 by N_1 matrix $\mathbf{X}_1$ and performing M_1-point column-wise DFT as the precoding process, i.e., $\mathbf{S}_{data} = \mathbf{F}_{M_1}\mathbf{X}_1$. Then, the method of frequency-domain pilot insertion can be illustrated in Fig. 5.1, where shaded patterns denote non-zero elements and blank circles denote zeros. $2K_{\max}$ guard intervals are added on both sides of each pilot respectively to prevent the frequency-domain channel information from being interfered by data symbols. Denoting the pilot vector as $\mathbf{P}_v = V_p\mathbf{1}_{1\times M_1}$, where V_p denotes the value of the pilot. The frequency-domain symbol matrix after pilot insertion

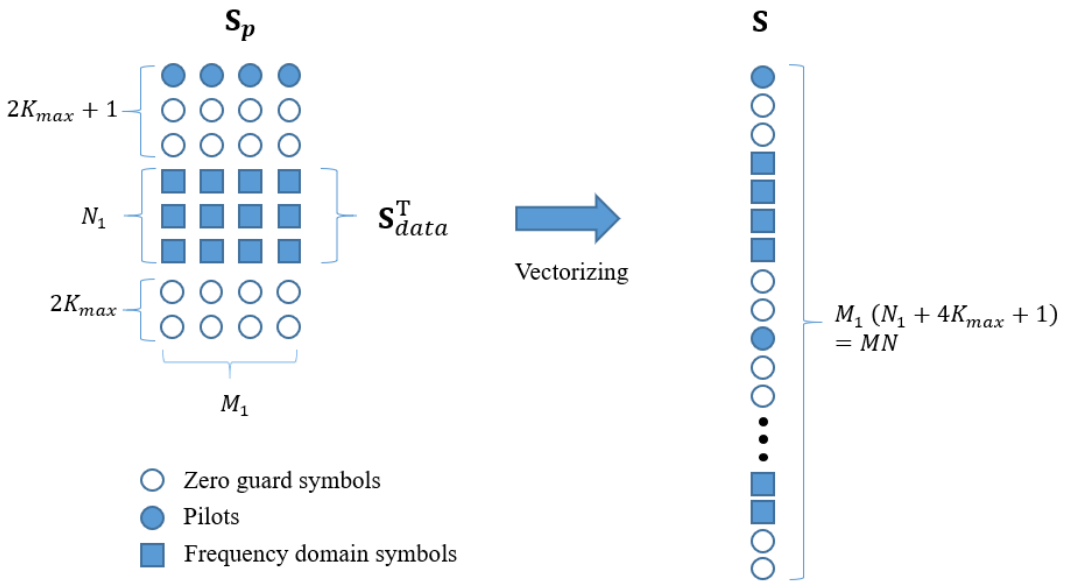

Figure 5.1: FD-PA-OTFS frequency-domain transmission frame construction with pilots.

can be expressed as $\mathbf{S_p} = [\mathbf{P}_v; \mathbf{0}_{2K_{\max}\times M_1}; \mathbf{S}_{data}^{\mathbf{T}}; \mathbf{0}_{2K_{\max}\times N_1}]$. $\mathbf{S_p}$ is then vectorised to form the frequency domain data vector $\mathbf{S} = \mathrm{vec}(\mathbf{S_p})$ which is finally transformed into the time domain through MN-point IDFT. A CP of length $L_{\max}$ will be inserted before transmission over the fast fading channel, and hence the total length of the transmission frame is $L_{\max}+MN$.

Assuming $M_1 = L_{\max}+1$, the overhead of frequency-domain pilots and time domain CP can be expressed as $(L_{\max}+(L_{\max}+1)(4K_{\max}+1))/(L_{\max}+MN)$, which is much less than the $(L_{\max}+(2L_{\max}+1)(4K_{\max}+1))/(L_{\max}+MN)$ (integer Doppler cases) and $(L_{\max}+(2L_{\max}+1)N)/(L_{\max}+MN)$ (fractional Doppler cases) in the popular delay-Doppler domain embedded pilot scheme [91].

5.2.1.2 Channel Estimation in Frequency Domain

Fig. 5.2 shows the process of frequency domain channel estimation. At the receiver, received signals are transformed into frequency domain first and then pilots are extracted. Since the stripe width of the frequency-domain channel matrix is $2K_{\max}+1$, only the

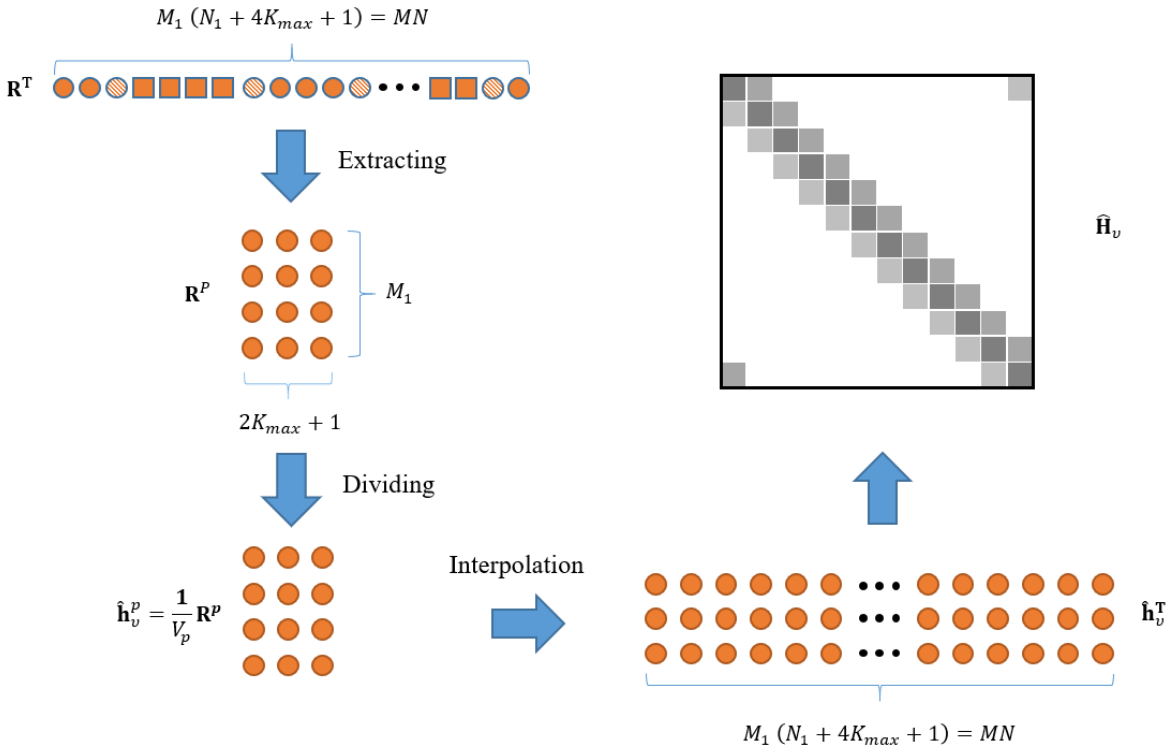

Figure 5.2: FD-PA-OTFS channel estimation process.

frequency bins at each transmitted pilot and adjacent $2K_{\max}$ bins on the both sides carry CSI. According to Fig. 5.2 and (2.22), extracted received signals for the k-th transmitted pilot can be expressed as

$$\begin{aligned}\mathbf{R}^{p,k} &= \mathbf{R}(\mathbf{j}_k) \\ &= \mathbf{H}_v(\mathbf{j}_k, (N_1 + 4K_{\max} + 1)k)V_p + \mathbf{W}(\mathbf{j}_k) \\ &= V_p \mathbf{h}_v^{p,k} + \mathbf{W}^{p,k}, \end{aligned} \tag{5.1}$$

where $k = 0, \ldots, M_1 - 1$, $\mathbf{j}_k = ((N_1 + 4K_{\max} + 1)k + [-K_{\max}; \ldots; K_{\max}])_{MN}$ is a vector containing the indices of frequency bins, $\mathbf{h}_v^{p,k} = \mathbf{H}_v(\mathbf{j}_k, (N_1 + 4K_{\max} + 1)k) = f_r H_v[(N_1 + 4K_{\max} + 1)k, \mathbf{j}_k]$, and $\mathbf{W}^{p,k} = \mathbf{W}(\mathbf{j}_k)$. Therefore, the extracted received signals for all pilots can be expressed as $\mathbf{R}^p = [\mathbf{R}^{p,0}; \mathbf{R}^{p,1}; \ldots; \mathbf{R}^{p,M_1-1}]$. Similarly, we denote $\mathbf{h}_v^p = [\mathbf{h}_v^{p,0}; \mathbf{h}_v^{p,1}; \ldots; \mathbf{h}_v^{p,M_1-1}]$ and $\mathbf{W}^p = [\mathbf{W}^{p,0}; \mathbf{W}^{p,1}; \ldots; \mathbf{W}^{p,M_1-1}]$.

From (5.1), the estimated frequency-Doppler domain channel representation sampled in the frequency domain at M_1 evenly spaced frequency bins can be obtained as

$$\hat{\mathbf{h}_v^p} = \frac{1}{V_p}\mathbf{R}^p. \tag{5.2}$$

For the M_1 by $(2K_{\max}+1)$ matrix $\hat{\mathbf{h}_v^p}$, the column dimension represents the frequency domain and the row dimension represents the Doppler domain. Finally, interpolation in frequency domain is applied to recover the whole frequency-Doppler domain channel $f_r H_v[i,j]$, which can be expressed as

$$\hat{\mathbf{h}_v} = \frac{1}{V_p}\mathbf{\Theta}\mathbf{R}^p, \tag{5.3}$$

where $\mathbf{\Theta}$ is an MN by N_1 interpolation matrix defined by

$$\mathbf{\Theta} = \mathbf{F}_{MN}\mathbf{\Omega}_1\mathbf{F}_{M_1}^{\mathbf{H}}\sqrt{\frac{MN}{M_1}}, \tag{5.4}$$

and $\mathbf{\Omega}_1 = [\mathbf{I}_{M_1}; \mathbf{0}_{M_1\times(MN-M_1)}]$ is used to pad zeros in time domain. Note that $\hat{\mathbf{h}_v}$ is the estimated $\mathbf{h}_v$ with only the $2K_{\max}+1$ non-zero columns.

Unlike the channel estimation techniques based on delay-Doppler domain embedded pilots, which consider the normalised Doppler frequencies in integer and fractional conditions because they produce different channel responses in this 2D delay-Doppler domain and thus different pilot-guard patterns are needed [91], the proposed frequency-domain estimation scheme works for both integer and fractional Doppler cases. This is because we effectively estimate the discrete frequency-Doppler channel representation which is valid for any Doppler shift from (2.20). As long as a suitable $K_{\max}$ is selected, the channel can be estimated with sufficient accuracy.

5.2.2 Time-Domain Pilot-Aided Scheme

The pilot design for TD-PA-OTFS transmission and associated channel estimation method are then presented as follows.

5.2.2.1 Pilot Design in Time Domain

With the same maximum number of resolvable multipaths $L_{\max}$ and Doppler spread $K_{\max}$ as in FD-PA-OTFS, $N_2 \geq 2K_{\max}+1$ pilot sections in the time domain must be inserted, each comprising $2L_{\max}+1$ time samples. The total number of time samples used for channel estimation is thus $N_2(2L_{\max}+1)$. Assuming that the length of time domain transmission frame is still MN, the number of precoded data symbols is $MN - N_2(2L_{\max}+1)$, which can be represented by an M_2 by N_2 matrix $\mathbf{s}_{data}$ where $M_2 = MN/N_2 - (2L_{\max}+1)$.

The original length M_2N_2 data vector can be reshaped into an M_2 by N_2 matrix $\mathbf{X}_2$. According to Fig. 4.3 and (4.2), $\mathbf{s}_{data}$ is obtained by performing N_2-point IDFT to each row in $\mathbf{X}_2$, i.e., $\mathbf{s}_{data} = \mathbf{X}_2\mathbf{F}_{N_2}^{\mathbf{H}}$. Fig. 5.3 (a) shows the method of time-domain pilot insertion. $L_{\max}$ guard intervals are added to both sides of each pilot. The pilot vector can be expressed as $\mathbf{P}_t = v_p\mathbf{1}_{1\times N_2}$, where v_p indicates the value of pilot in time domain. Accordingly, the time-domain symbols after pilot insertion can be expressed as $\mathbf{s}_p = [\mathbf{P_t}; \mathbf{0}_{L_{\max}\times N_2}; \mathbf{s}_{data}; \mathbf{0}_{L_{\max}\times N_2}]$.

5.2.2.2 Channel Estimation in Time Domain

Similarly, the extracted signals for the k-th pilot can be expressed as a column vector of length $L_{\max}+1$

$$\begin{aligned}\mathbf{r}^{p,k} &= \mathbf{r}((M_2+2L_{\max}+1)k + [0;\ldots;L_{\max}]) \\ &= \mathbf{H}_t((M_2+2L_{\max}+1)k + [0;\ldots;L_{\max}], (M_2+2L_{\max}+1)k)v_p \\ &+ \mathbf{w}((M_2+2L_{\max}+1)k + [0;\ldots;L_{\max}]) \\ &= v_p\mathbf{h}_t^{p,k} + \mathbf{w}^{p,k}, \end{aligned} \tag{5.5}$$

where $k = 0,\ldots,N_2-1$, $\mathbf{h}_t^{p,k} = \mathbf{H}_t((M_2+2L_{\max}+1)k + [0;\ldots;L_{\max}], (M_2+2L_{\max}+1)k) = d_r h_t[[0;\ldots;L_{\max}], (M_2+2L_{\max}+1)k + [0;\ldots;L_{\max}]]$, and $\mathbf{w}^{p,k} = \mathbf{w}((M_2+2L_{\max}+1)k + [0;\ldots;L_{\max}])$.

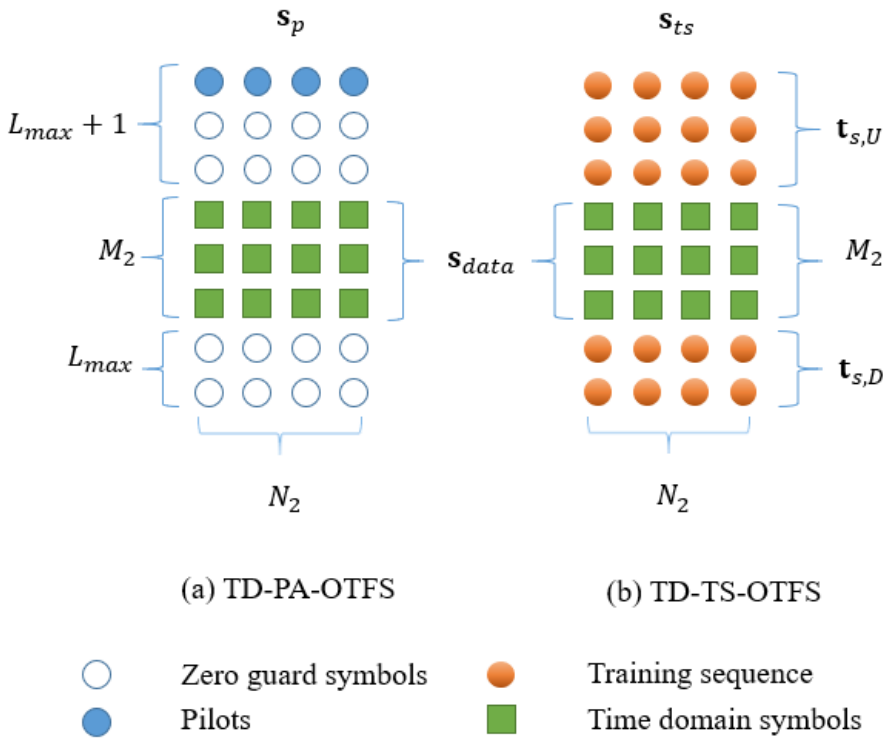

Figure 5.3: Time-domain transmission frame constructions of (a) TD-PA-OTFS and (b) TD-TS-OTFS.

Therefore, the extracted received signals for all pilots can be expressed as $\mathbf{r}^p = [\mathbf{r}^{p,0}, \mathbf{r}^{p,1}, ..., \mathbf{r}^{p,N_2-1}]$. Similarly, we denote $\mathbf{h}_t^p = [\mathbf{h}_t^{p,0}, \mathbf{h}_t^{p,1}, ..., \mathbf{h}_t^{p,N_2-1}]$ and $\mathbf{w}^p = [\mathbf{w}^{p,0}, \mathbf{w}^{p,1}, ..., \mathbf{w}^{p,N_2-1}]$.

From (5.5) and expressed as an $L_{\max}+1$ by N_2 matrix where the column dimension represents the delay domain and the row dimension represents the time domain, the estimated delay-time domain channel representation sampled in the time domain at N_2 evenly spaced samples but delayed by 0 to $L_{\max}$ samples for the $L_{\max}+1$ rows, respectively, can be expressed as

$$\hat{\mathbf{h}_t^p} = \frac{1}{v_p}\mathbf{r}^p. \tag{5.6}$$

Note that $\hat{\mathbf{h}_t^p}(:,j)$ for $j = 0,1,...,N_2-1$, are the estimates of $d_r h_t[i,(M_2+2L_{\max}+1)j+i]$

for $i = 0, 1, ..., L_{\max}$. Finally, interpolation in time domain is applied to recover the whole delay-time domain channel $d_r h_t[i, j]$, which can be expressed as

$$\hat{\mathbf{h}}_t = \frac{1}{v_p} \mathbf{r}^p \mathbf{\Psi}, \tag{5.7}$$

where $\mathbf{\Psi}$ denotes an N_2 by MN interpolation matrix expressed as

$$\mathbf{\Psi} = \mathbf{F}_{N_2} \mathbf{\Omega}_2 \odot \mathbf{\Phi} \mathbf{F}^{\mathbf{H}}_{MN} \sqrt{\frac{MN}{N_2}}, \tag{5.8}$$

$\mathbf{\Omega}_2$ is an $N_2 \times MN$ matrix used to pad zeros in Doppler domain with each element expressed as

$$\mathbf{\Omega}_2(i, j) = \begin{cases} 1, & i = j \ for \ i < N_2/2 \\ & \text{or } j = MN - N_2 + i \ for \ i \geq N_2/2, \\ 0, & otherwise, \end{cases} \tag{5.9}$$

and $\mathbf{\Phi}$ is an $L_{\max} + 1$ by MN Doppler domain phase shifting matrix[1] expressed as

$$\mathbf{\Phi} = \begin{bmatrix} 1 & 1 & \cdots & 1 \\ 1 & e^{-\mathbf{j}\frac{2\pi}{MN}} & \cdots & e^{-\mathbf{j}\frac{2\pi(MN-1)}{MN}} \\ \vdots & \vdots & \ddots & \vdots \\ 1 & e^{-\mathbf{j}\frac{2\pi}{MN}L_{\max}} & \cdots & e^{-\mathbf{j}\frac{2\pi(MN-1)}{MN}L_{\max}} \end{bmatrix}. \tag{5.10}$$

Note that no additional CP is necessary for the TD-PA-OTFS transmission frame as the first $L_{\max}$ zero guard symbols effectively serve as the CP. Apparently, the overhead of time domain pilots is $(2K_{\max}+1)(2L_{\max}+1)/MN$, which is similar to that of FD-PA-OTFS and still much less than that of the 2D embedded pilot-aided scheme [91].

5.2.3 Time-Domain Training Sequence Scheme

To maintain the same SNR in each pilot section as the average SNR of the transmitted signal, each time domain pilot must be transmitted with a power much higher than the average one of a transmission frame, leading to a high PAPR. To solve this problem, TD-TS-OTFS is proposed alternatively for time domain channel estimation.

[1]This matrix is introduced based on the DFT property, i.e., a time domain offset corresponds to a Doppler domain linear phase shifting.

5.2.3.1 Low PAPR Pilot Design

Fig. 5.3 (b) shows the frame construction of TD-TS-OTFS. Similar to TD-PA-OTFS, $N_2 \geq 2K_{\max}+1$ training sequence sections in the time domain must be inserted, each comprising $2L_{\max}+1$ time domain samples. The precoded data symbols can still be represented by $\mathbf{s}_{data}$. A partially repeated Zadoff Chu (ZC) sequence[2] is adopted for each training sequence, which can be expressed as

$$\begin{aligned}\mathbf{t}_{s,1} &= \mathbf{t}_{s,2} = ... = \mathbf{t}_{s,N_2} \\ &= v_t[\mathbf{z}(1),...,\mathbf{z}(L_{\max}),\mathbf{z}(0),\mathbf{z}(1),...,\mathbf{z}(L_{\max})]^{\mathbf{T}},\end{aligned} \tag{5.11}$$

where v_t determines the power of training sequences and $\mathbf{z}$ indicates the ZC sequence in vector form. All the training sequences can be expressed as $\mathbf{t}_s = [\mathbf{t}_{s,1},\mathbf{t}_{s,2},...,\mathbf{t}_{s,N_2}]$. The time-domain symbols after adding the training sequences can be expressed as $\mathbf{s}_{ts} = [\mathbf{t}_{s,D};\mathbf{s}_{data};\mathbf{t}_{s,U}]$, where $\mathbf{t}_{s,U}$ indicates the first $L_{\max}$ rows of $\mathbf{t}_s$ and $\mathbf{t}_{s,D}$ indicates the rest $L_{\max}+1$ rows of $\mathbf{t}_s$.

5.2.3.2 Associated Channel Estimation

Assume that the channel remains unchanged during one training sequence period. The extracted received signal resulting from the k-th training sequence can be expressed as

$$\begin{aligned}\mathbf{r}^{t,k} &= \mathbf{r}((M_2+2L_{\max}+1)k+[0;...;L_{\max}]) \\ &\approx \mathbf{q}\mathbf{H}_t((M_2+2L_{\max}+1)k+[0;...;L_{\max}],(M_2+2L_{\max})k) \\ &+ \mathbf{w}((M_2+2L_{\max}+)k+[0;...;L_{\max}])\end{aligned} \tag{5.12}$$

[2]Any other sequence can be used as long as it satisfies some desired properties as shown in Appendix.

where $k = 0, ..., N_2 - 1$, and $\mathbf{q}$ is a toeplitz-form matrix composed of the ZC sequence

$$\mathbf{q} = v_t \begin{bmatrix} \mathbf{z}(0) & \mathbf{z}(L_{\max}) & \cdots & \mathbf{z}(1) \\ \mathbf{z}(1) & \mathbf{z}(0) & \cdots & \mathbf{z}(2) \\ \vdots & \vdots & \ddots & \vdots \\ \mathbf{z}(L_{\max}) & \mathbf{z}(L_{\max}-1) & \cdots & \mathbf{z}(0) \end{bmatrix}. \tag{5.13}$$

Denote the extracted received signals resulting from all training sequences as $\mathbf{r}^t = [\mathbf{r}^{t,0}, \mathbf{r}^{t,1}, ..., \mathbf{r}^{t,N_2-1}]$. Then, the estimated delay-time domain channel representation can be expressed as

$$\hat{\mathbf{h}}_t^t = \mathbf{q}^{-1}\mathbf{r}^t. \tag{5.14}$$

Through the same interpolating matrix as that used in TD-PA-OTFS, the estimated delay-time channel representation can be expressed as

$$\hat{\mathbf{h}}_t = \mathbf{q}^{-1}\mathbf{r}^t\mathbf{\Psi}. \tag{5.15}$$

Note that since TD-PA-OTFS and TD-TS-OTFS share the same frame structure, the overhead of TD-TS-OTFS is the same as that of TD-PA-OTFS, but the training sequence can significantly reduce the PAPR of the time domain signal if the power of the training sequence is set to the average power of the transmitted signal.

5.3 Performance Analysis

In this section, the MSE analyses for channel estimations in FD-PA-OTFS, TD-PA-OTFS, and TD-TS-OTFS are performed against the exact delay-Doppler domain channel matrix. Assume that the time delays of all multipaths are within $d_r L_{\max}$ and channel gains are independent of each other. Each path has an associated Doppler frequency shift which is uniformly distributed in $[-f_r K_{\max}, f_r K_{\max}]$. Note that proper $d_{\max}$ and $f_{\max}$ considering allowed leakage power are assumed in the analysis. As such, the performance analysis can also be applied for the off-grid situation with fractional delay and Doppler shift.

Denote the delay-Doppler domain channel matrix as $\mathbf{h}$, where the column dimension indicates delay domain and the row dimension indicates Doppler domain. Note that the size of $\mathbf{h}$ may be different in different schemes.

5.3.1 MSE Analysis for FD-PA-OTFS

According to (5.2) and [113], the estimated channel with FD-PA-OTFS can be linked to the M_1 by $2K_{\max}+1$ delay-Doppler domain channel matrix $\mathbf{h}$ as

$$\begin{aligned}\hat{\mathbf{h}}_{FP} &= \frac{1}{\sqrt{M_1}}\mathbf{F}_{M_1}^{\mathbf{H}}\hat{\mathbf{h}_v^p} \\ &= \frac{1}{\sqrt{M_1}}\mathbf{F}_{M_1}^{\mathbf{H}}\frac{1}{V_p}\mathbf{R}^p \\ &= \frac{1}{\sqrt{M_1}}\mathbf{F}_{M_1}^{\mathbf{H}}\frac{1}{V_p}(V_p\mathbf{h}_v^p+\mathbf{W}^p) \\ &= \frac{1}{\sqrt{M_1}}\mathbf{F}_{M_1}^{\mathbf{H}}\frac{1}{V_p}(V_p\sqrt{M_1}\mathbf{F}_{M_1}\mathbf{h}+\mathbf{W}^p) \\ &= \mathbf{h}+\mathbf{F}_{M_1}^{\mathbf{H}}\frac{1}{\sqrt{M_1}V_p}\mathbf{W}^p. \end{aligned} \tag{5.16}$$

To keep the signal power constant, we set $V_p=\sqrt{(4K_{\max}+1)\sigma_{\mathbf{S}}^2}$, where $\sigma_{\mathbf{S}}^2$ denotes the average signal power in frequency domain. Therefore, the MSE of FD-PA-OTFS can be expressed as

$$\begin{aligned}\mathbf{MSE}_{FP} &= E\{\mathrm{tr}\{(\hat{\mathbf{h}}_{FP}-\mathbf{h})(\hat{\mathbf{h}}_{FP}-\mathbf{h})^H\}\} \\ &= \frac{1}{V_p^2}\mathrm{tr}\{E\{\mathbf{W}^p(\mathbf{W}^p)^{\mathbf{H}}\}\} \\ &= \frac{2K_{\max}+1}{(4K_{\max}+1)\gamma}, \end{aligned} \tag{5.17}$$

where $\gamma=\sigma_{\mathbf{S}}^2/\sigma_{\mathbf{W}}^2$ is the SNR and $\sigma_{\mathbf{W}}^2$ denotes the frequency domain noise power.

5.3.2 MSE Analysis for TD-PA-OTFS

According to (5.6), the estimated channel with TD-PA-OTFS can be linked to the $L_{\max}+1$ by N_2 delay-Doppler domain channel matrix $\mathbf{h}$ as

$$\begin{aligned}\hat{\mathbf{h}}_{TP} &= \frac{1}{\sqrt{N_2}}\hat{\mathbf{h}_t^p}\mathbf{F}_{N_2}\odot\mathbf{E}^* \\ &= \frac{1}{\sqrt{N_2}v_p}\mathbf{r}^p\mathbf{F}_{N_2}\odot\mathbf{E}^* \\ &= \frac{1}{\sqrt{N_2}v_p}(v_p\mathbf{h}_t^p+\mathbf{w}^p)\mathbf{F}_{N_2}\odot\mathbf{E}^* \\ &= \frac{1}{\sqrt{N_2}v_p}(v_p\mathbf{h}\odot\mathbf{E}\mathbf{F}_{N_2}^{\mathbf{H}}\sqrt{N_2}+\mathbf{w}^p)\mathbf{F}_{N_2}\odot\mathbf{E}^* \\ &= \mathbf{h}+\frac{1}{\sqrt{N_2}v_p}\mathbf{w}^p\mathbf{F}_{N_2}\odot\mathbf{E}^*, \end{aligned} \tag{5.18}$$

where $\mathbf{E}=[\mathbf{\Phi}(:,0),...,\mathbf{\Phi}(:,N_2/2-1),\mathbf{\Phi}(:,MN-N_2/2),..,\mathbf{\Phi}(:,MN-1)]$ is an $L_{\max}+1$ by N_2 Doppler domain phase shifting matrix. To keep the signal power constant, we set $v_p=\sqrt{(2L_{\max}+1)\sigma_{\mathbf{s}}^2}$ where $\sigma_{\mathbf{s}}^2$ denotes the average signal power in time domain. Accordingly, the MSE of TD-PA-OTFS can be expressed as

$$\begin{aligned}\mathbf{MSE}_{TP} &= E\{\mathrm{tr}\{(\hat{\mathbf{h}}_{TP}-\mathbf{h})(\hat{\mathbf{h}}_{TP}-\mathbf{h})^H\}\} \\ &= \frac{1}{(v_p)^2}\mathrm{tr}\{E\{\mathbf{w}^p(\mathbf{w}^p)^{\mathbf{H}}\}\} \\ &= \frac{(L_{\max}+1)}{(2L_{\max}+1)\gamma}, \end{aligned} \tag{5.19}$$

where $\gamma=\sigma_{\mathbf{s}}^2/\sigma_{\mathbf{w}}^2$ is the SNR which is the same as that evaluated in the frequency domain and $\sigma_{\mathbf{w}}^2$ denotes the time domain noise power.

5.3.3 MSE Analysis for TD-TS-OTFS

According to (5.14), the linkage between the estimated channel with TD-TS-OTFS and $\mathbf{h}$ in delay-Doppler domain can be expressed as

$$\begin{aligned}\hat{\mathbf{h}}_{TS} &= \frac{1}{\sqrt{N_2}}\hat{\mathbf{h}_t^t}\mathbf{F}_{N_2}\odot\mathbf{E}^* \\ &= \frac{1}{\sqrt{N_2}}\mathbf{q}^{-1}\mathbf{r}^t\mathbf{F}_{N_2}\odot\mathbf{E}^*. \end{aligned} \tag{5.20}$$

Denote the $L_{\max}+1$ by MN delay-time domain channel representation in matrix form as $\mathbf{h}_t$. For the k-th training sequence, part of $\mathbf{h}_t$ will be involved to produce the extracted received signal $\mathbf{r}^{t,k}$ as in (5.12), which can be expressed as

$$\mathbf{h}_t^k = [\mathbf{h}_t(:,K), \mathbf{h}_t(:,K+1), ..., \mathbf{h}_t(:,K+L_{\max})], \tag{5.21}$$

where $K = (M_2 + 2L_{\max} + 1)k$. Then, $\mathbf{r}^t$ can be expressed as

$$\begin{aligned} \mathbf{r}^t &= \mathbb{Q} \begin{bmatrix} \mathbf{h}_t^1(:,0) & \cdots & \mathbf{h}_t^{N_2}(:,0) \\ \mathbf{h}_t^1(:,1) & \cdots & \mathbf{h}_t^{N_2}(:,1) \\ \vdots & \ddots & \vdots \\ \mathbf{h}_t^1(:,L_{\max}) & \cdots & \mathbf{h}_t^{N_2}(:,L_{\max}) \end{bmatrix} + \mathbf{w}^t \\ &= \mathbb{Q} \begin{bmatrix} \mathbf{h}\mathbf{E}_0\mathbf{F}_{N_2}^{\mathbf{H}} \\ \mathbf{h}\mathbf{E}_1\mathbf{F}_{N_2}^{\mathbf{H}} \\ \vdots \\ \mathbf{h}\mathbf{E}_{L_{\max}}\mathbf{F}_{N_2}^{\mathbf{H}} \end{bmatrix} \sqrt{N_2} + \mathbf{w}^t \end{aligned} \tag{5.22}$$

where $\mathbf{h}$ is an $L_{\max}+1$ by N_2 delay-Doppler domain channel matrix, $\mathbb{Q} = \text{diag}\{\mathbf{q}(0,:), \mathbf{q}(1,:), ..., \mathbf{q}(L_{\max},:)\}$, $\mathbf{E}_k$ is an N_2 by N_2 diagonal Doppler domain phase shifting matrix defined as

$$\mathbf{E}_k = \text{diag}\{\mathbf{E}(k,:)\}. \tag{5.23}$$

Substituting $\mathbf{r}^t$ into (5.20), the estimated channel can be expressed as

$$\begin{aligned} \hat{\mathbf{h}}_{TS} &= \mathbf{q}^{-1}\mathbf{r}^t\mathbf{F}_{N_2} \odot \mathbf{E}^* \\ &= \mathbf{q}^{-1}\mathbb{Q} \begin{bmatrix} \mathbf{h}\mathbf{E}_0 \\ \mathbf{h}\mathbf{E}_1 \\ \vdots \\ \mathbf{h}\mathbf{E}_{L_{\max}} \end{bmatrix} \odot \mathbf{E}^* + \frac{1}{\sqrt{N_2}}\mathbf{q}^{-1}\mathbf{w}^t\mathbf{F}_{N_2} \odot \mathbf{E}^*. \end{aligned} \tag{5.24}$$

With the $L_{\max}+1$ by N_2 delay-Doppler domain channel matrix $\mathbf{h}$, we assume that the path gains h_i at delay index i are independent of each other for all $i = 0, 1, ..., L_{\max}$, and the Doppler frequency shifts obey uniform distribution for each path. Therefore, we can focus on only one given element in $\mathbf{h}$ to evaluate its MSE and then sum up the MSEs for

all elements and average over all possible Doppler shifts. Letting $\mathbf{h}(i,j) = h_i$ for any j and according to (5.24), the MSE of TD-TS-OTFS for the normalised delay i and normalised Doppler shift j can be derived in Appendix. Finally, assuming $v_t = \sigma_{\mathbf{s}}$ to keep the same transmitted training sequence power and averaging over all $2K_{\max}+1$ Doppler shifts, the total MSE can be expressed as

$$\mathbf{MSE}_{TS} = \frac{1}{2K_{\max}+1} \sum_{i=0}^{L_{\max}} \sum_{j=0}^{N_2-1} \mathbf{MSE}_{TS}^{(i,j)} + \frac{1}{\gamma}, \tag{5.25}$$

where $\mathbf{MSE}_{TS}^{(i,j)}$ is expressed in (5.28).

Compared with TD-PA-OTFS, TD-TS-OTFS has an additional term in its MSE expression which is related to the channel conditions rather than the SNR. The impact of this additional term will be investigated in the next section.

5.4 Simulation Results

In this section, simulations are performed to show the channel estimation MSE and BER performance of FD-PA-OTFS, TD-PA-OTFS and TD-TS-OTFS for uncoded data information. MMSE equalisation in respective frequency or time domain is adopted to recover the data information [74, 113]. The simulation parameters are listed in Table 2.1, in which the maximum delay time $d_{\max}$ is selected as 3.82 μs according to LOS TDL-D urban macro (UMa) channels [73]. The channel power delay profile is shown in Fig. 2.6. The first path is Rician distributed with K factor 13.3 dB and all the other paths are Rayleigh distributed. Note that the parameters M and N are also referred to as the number of subcarriers and the number of OFDM symbols respectively in the literature as an OTFS system is often compared with an OFDM system for performance evaluation with OTFS transmission frame length equivalent to N OFDM frames of length M. Based on the above settings, the overhead of FD-PA-OTFS, TD-PA-OTFS and TD-TS-OTFS are evaluated as shown in Table 5.1, in which the overheads of the embedded pilot-aided

Table 5.1: Overhead of Different Transmission Schemes

Transmission Scheme	Overhead
FD-PA-OTFS	$\frac{L_{\max}+(L_{\max}+1)(4K_{\max}+1)}{L_{\max}+MN}$ =5.4%
TD-PA-OTFS	$\frac{(2K_{\max}+1)(2L_{\max}+1)}{MN}$ = 6.1%
TD-TS-OTFS	$\frac{(2K_{\max}+1)(2L_{\max}+1)}{MN}$ =6.1%
Embedded delay-Doppler Domain Pilot-Aided Scheme	$\frac{L_{\max}+(2L_{\max}+1)(4K_{\max}+1)}{L_{\max}+MN}$ =10.3 % (integer Doppler case) $\frac{L_{\max}+(2L_{\max}+1)N}{L_{\max}+MN}$ = 24.9% (fractional Doppler case)

delay-Doppler domain method are also provided for comparison. With the benefit of ZC sequences and under above parameter settings, the PAPR of TD-TS-OTFS is about 5 dB, which is much smaller than TD-PA-OTFS's 17 dB.

Fig. 5.4 shows the MSE comparison among the proposed schemes. Note that the theoretical MSEs have been calculated according to the parameters set in Table 2.1 and Fig. 2.6, and have been verified to match the respective simulation results. Therefore, Fig. 5.4 omits the theoretical MSEs and shows only the simulated MSEs. Here the SNR range is extended to 0-60 dB to show the performance in high SNR region. It is seen that the channel estimation MSEs of FD-PA-OTFS and TD-PA-OTFS are almost the same as theoretically proved in (5.17) and (5.19). For TD-TS-OTFS, the channel estimation MSEs have about 3 dB degradation compared with that of FD-PA-OTFS or TD-PA-OTFS in the low SNR region and show different error floors over fast fading channels with non-zero movement speeds in the high SNR region. This has been verified in Section 5.3 as the channel estimation MSE expression for TD-TS-OTFS has an SNR independent term which is determined by the channel multipath power profile and Doppler spread.

Fig. 5.5 shows the BER performance of FD-PA-OTFS, TD-PA-OTFS and TD-TS-OTFS with channel estimation performed over each transmission frame. The 4-QAM is adopted and the pilot values $V_P = 4K_{\max} + 1$ and $v_P = 2L_{\max} + 1$ are selected with unit signal

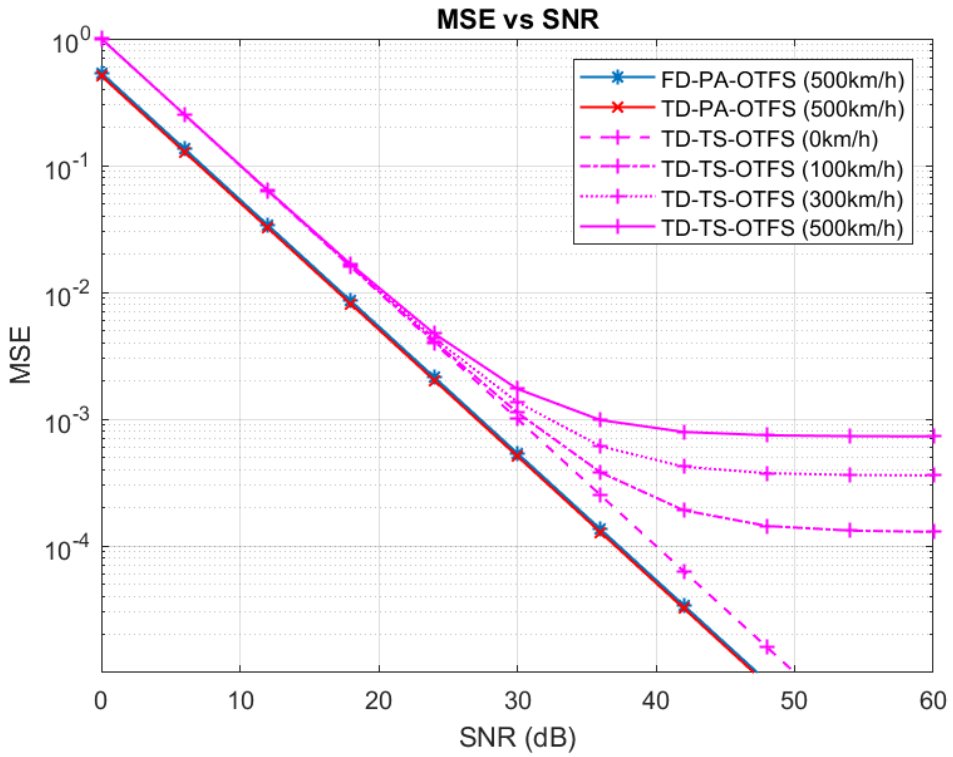

Figure 5.4: Channel estimation performance comparison among FD-PA-OTFS, TD-PA-OTFS and TD-TS-OTFS.

power. It is noticed that all of these schemes work well over the fast fading channels. FD-PA-OTFS and TD-PA-OTFS achieve similar performance and TD-TS-OTFS shows a degradation of about 3 dB due to the larger channel estimation error as shown in Fig. 5.4.

To verify that the proposed OTFS variants do not compromise in performance with the pilot or training sequence insertion, performance comparison between conventional OTFS system and FD-PA-OTFS systems is presented in Fig. 5.6. It is assumed that both systems transmit the same number of data and have perfectly known CSI. With the same equalisation algorithm, the simulation shows that the FD-PA-OTFS system can achieve similar performance to the original OTFS system. The same conclusion can be drawn for TD-PA-OTFS. The performance of FD-PA-OTFS with estimated CSI is also shown, which indicates a 1 to 3 dB degradation.

vs TD.PNG

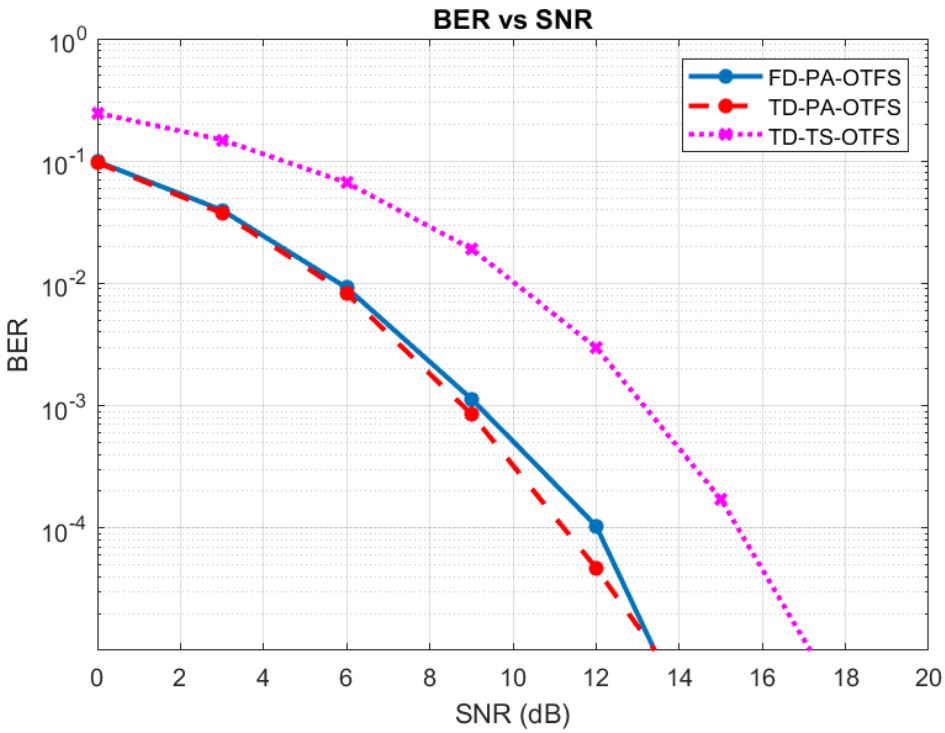

Figure 5.5: BER performance comparison among FD-PA-OTFS, TD-PA-OTFS and TD-TS-OTFS with estimated CSIs.

The BER performance of FD-PA-OTFS under different maximum speeds is shown in Fig. 5.7. With the same system parameter settings, the BER performance improves slightly as the maximum speed in the channel increases. This confirms with the finding reported in [113], that is, when the frame structure is fixed, a higher maximum Doppler shift can contribute to a better diversity performance as the time diversity due to Doppler shift is exploited by OTFS.

The same improved diversity performance at higher speed is observed for TD-TS-OTFS as shown in Fig. 5.7. Note that, when performing channel estimation using training sequence, it is assumed that the CSI remains unchanged over a training sequence period, and this approximation has demonstrated an MSE floor in the high SNR region as shown in Fig. 5.4. From Fig. 5.7, it is also noticed that the BER has already reached 10^{-5} at around 18 dB SNR, which is far behind the high SNR region where the MSE starts to

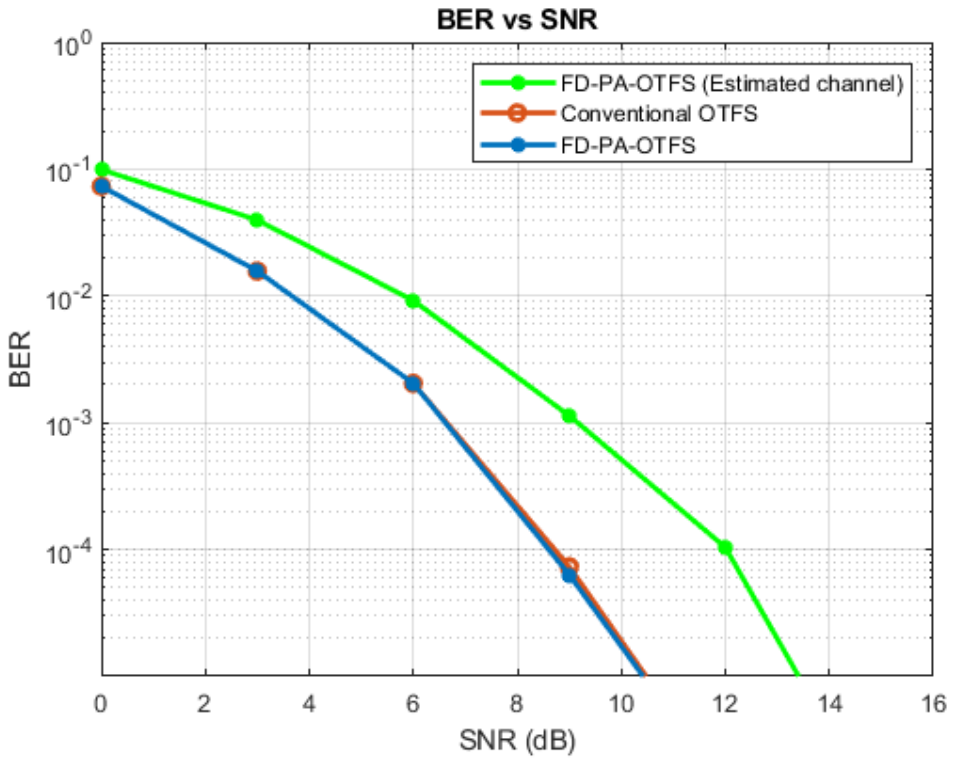

Figure 5.6: BER performance comparison between FD-PA-OTFS and original OTFS.

demonstrate the error floor. Therefore, the impact of the MSE error floor can be neglected and TD-TS-OTFS has the same ability to gain diversity over fast fading channels.

5.5 Conclusions

In this chapter, with the OTFS system being reformulated as a precoded OFDM system, traditional frequency domain pilot aided channel estimation can be easily implemented in FD-PA-OTFS system. The principle can be similarly applied to time domain channel estimation, resulting in two additional OTFS variants, TD-PA-OTFS and TD-TS-OTFS. Compared with conventional delay-Doppler domain embedded pilot-aided scheme for channel estimation, the proposed schemes have much lower signalling overhead without compromising the diversity performance. Closed-form theoretical MSE expressions are also derived and verified by simulation results. Among the proposed OTFS variants,

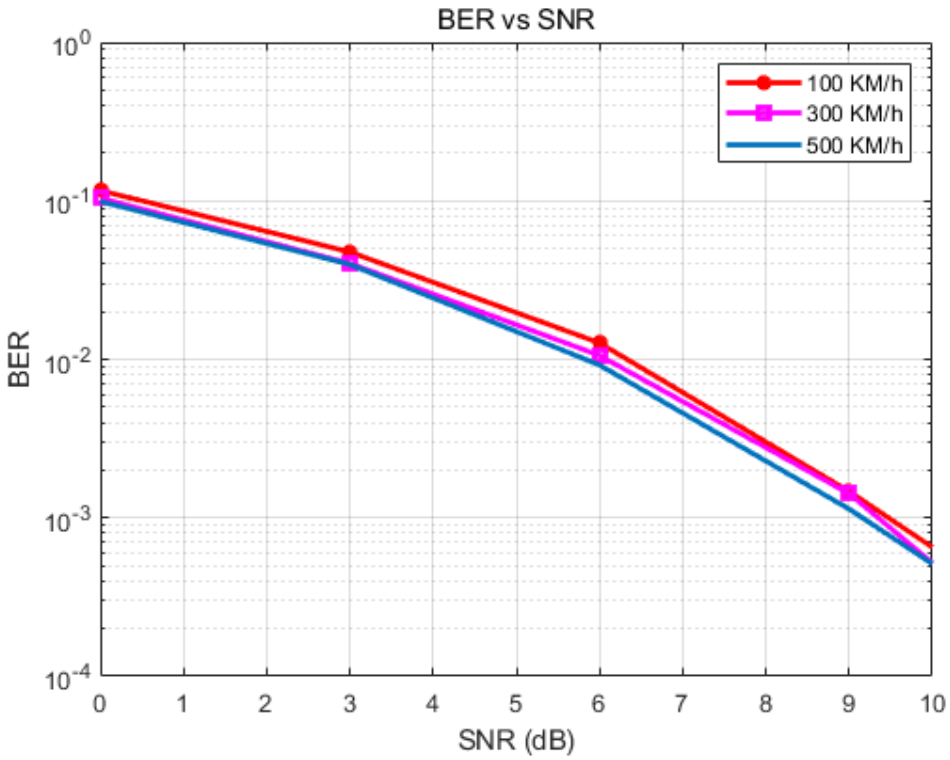

Figure 5.7: BER performance of FD-PA-OTFS under different maximum speeds.

FD-PA-OTFS is the most efficient one for high mobility wireless communications as it can achieve the expected performance without sacrificing any power efficiency. The OTFS variants proposed in this chapter effectively overcome the challenges of high system overhead for OTFS channel estimation and will be more suitable for practical applications.

5.6 Appendix

Denoting $\mathbf{A}$ and $\mathbf{B}$ as the first and second terms on the right-hand-side (RHS) of (5.24), respectively, the MSE can be expressed as

$$\begin{aligned}\mathbf{MSE}_{TS} &= E\{\mathrm{tr}\{(\mathbf{A}+\mathbf{B}-\mathbf{h})(\mathbf{A}+\mathbf{B}-\mathbf{h})^H\}\} \\ &= E\{\mathrm{tr}\{(\mathbf{A}-\mathbf{h})(\mathbf{A}-\mathbf{h})^H\}\} + E\{\mathrm{tr}\{\mathbf{B}\mathbf{B}^{\mathbf{H}}\}\}. \end{aligned} \tag{5.26}$$

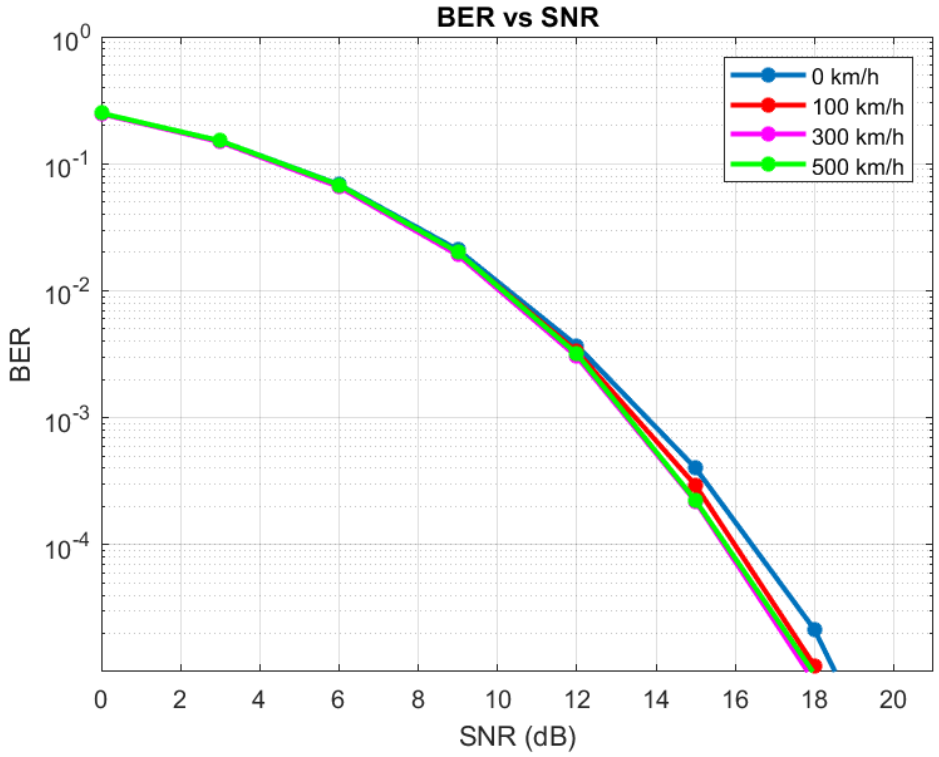

Figure 5.8: BER performance of TD-TS-OTFS under different maximum speeds.

With $\mathbf{h}(i,j) = h_i$ at the i-th delay and any Doppler index j, $\mathbf{A}$ can be simplified as

$$\begin{aligned}\mathbf{A} &= \mathbf{q}^{-1}[\mathbf{Z}_1, \begin{bmatrix} \mathbf{q}(0,i)h_i\mathbf{E}(0,j) \\ \mathbf{q}(1,i)h_i\mathbf{E}(1,j) \\ \vdots \\ \mathbf{q}(L_{\max},i)h_i\mathbf{E}(L_{\max},j) \end{bmatrix}, \mathbf{Z}_2] \odot \mathbf{E}^* \\ &= [\mathbf{Z}_1, \begin{bmatrix} \sum_{k=0}^{L_{\max}} \mathbf{q}^{-1}(0,k)\mathbf{q}(k,i)h_i\mathbf{E}(k,j) \\ \sum_{k=0}^{L_{\max}} \mathbf{q}^{-1}(1,k)\mathbf{q}(k,i)h_i\mathbf{E}(k,j) \\ \vdots \\ \sum_{k=0}^{L_{\max}} \mathbf{q}^{-1}(L_{\max},k)\mathbf{q}(k,i)h_i\mathbf{E}(k,j) \end{bmatrix}, \mathbf{Z}_2] \odot \mathbf{E}^*,\end{aligned} \tag{5.27}$$

where $\mathbf{Z}_1 = \mathbf{0}_{(L_{\max}+1)\times i}$, $\mathbf{Z}_2 = \mathbf{0}_{(L_{\max}+1)\times(N_2-i-1)}$.

The first term on the RHS of (5.26) can be obtained by summing up the MSEs of all non-zero elements in $(\mathbf{A}-\mathbf{h})$ for the path at the i-th delay index and any Doppler index j,

i.e.,

$$\begin{aligned}\mathbf{MSE}_{TS}(i,j) &= E\left\{\mathrm{tr}\left\{(\mathbf{A}-\mathbf{h})(\mathbf{A}-\mathbf{h})^H\right\}\right\} \\ &= \sum_{l=0}^{L_{\max}}\left|\sum_{k=0}^{L_{\max}}\mathbf{q}^{-1(l,k)}\mathbf{q}^{(k,i)}\mathbf{E}(k,j)\right|^2\sigma_{h_i}^2-\sigma_{h_i}^2,\end{aligned} \tag{5.28}$$

where $\sigma_{h_i}^2 = E\left\{|h_i|^2\right\}$, for $i = 0,1,...,L_{\max}$, which is also referred to as the channel multi-path power delay profile.

Assuming that all the elements in $\mathbf{w}^t$ are independent and identically Gaussian distributed, the second term on the RHS of (5.26) can be obtained directly as

$$\begin{aligned}\mathbf{MSE}_{TS}^{noise} &= E\left\{\mathrm{tr}\left\{\mathbf{B}\mathbf{B}^{\mathbf{H}}\right\}\right\} \\ &= E\left\{\mathrm{tr}\left\{\frac{1}{N_2}\mathbf{q}^{-1}\mathbf{w}^t\mathbf{w}^{t\mathbf{H}}(\mathbf{q}^{-1})^{\mathbf{H}}\right\}\right\} \\ &= \mathrm{tr}\left\{\frac{1}{N_2}(\mathbf{q}^{-1})^{\mathbf{H}}\mathbf{q}^{-1}N_2\sigma_{\mathbf{w}}^2\mathbf{I}_{L_{\max}+1}\right\} \\ &= \frac{1}{\gamma},\end{aligned} \tag{5.29}$$

where the matrix $\mathbf{q}$ satisfies $\mathbf{q}^{\mathbf{H}}\mathbf{q} = (L_{\max}+1)\mathbf{I}_{L_{\max}+1}$ with properly designed training sequence. Therefore, the total MSE can be expressed as shown in (5.25).

CHAPTER 6

CONCLUSIONS AND FUTURE WORK

6.1 Summary of Contributions

This thesis aims to investigate how to improve the equalisation and channel estimation performance for novel modulations such as OTFS and conventional modulations such as OFDM and SC-FDE over fast fading channels. The thesis also aims to design more efficient OTFS-type schemes in terms of diversity performance, signalling overhead, computational complexity, and power efficiency. The main contributions are summarised as follows.

1. Low-complexity linear equalisation over fast fading channels

Explicit received signal models in discrete time and frequency domains are derived, enabling frequency domain channel matrix with more concise structure to be adopted in the high-mobility systems other than the conventional delay-Doppler and time domain OTFS system models. They allow low-complexity linear equalisation to be adopted in systems with long frame modulations such as OTFS, which can fully resolve the Doppler spread. The signal models and equalisation methods for systems with short signal frames are also derived, such as OFDM and SC-FDE, which can partially resolve the Doppler

spread. These models and methods can be used to improve the performance of these short-frame systems in fast fading channels without requiring any change in signalling protocol. They allow the proposed equalisation techniques to be applied directly to the existing practical systems and greatly save the cost. Extensive simulation results are provided, which verify the effectiveness of the proposed models and methods. These results include the simulation of the proposed equalisation schemes under various channel conditions and with imperfect channel estimation, which demonstrate the suitability of the proposed technique for practical applications.

2. Diversity performance analysis for OTFS system

Based on the system models and input-output relationships, the diversity performance analysis is performed for OTFS under ML equalisations, proving that OTFS has the potential to achieve full diversity in both time and frequency domains. The theoretical performance for OTFS under MMSE equalisation is also derived via channel matrix eigenvalue decomposition, which provides a new tool for better analysing and understanding the impact of channel and signal modulation on system performance. Meanwhile, it is proved that OTFS is equivalent to a general precoded OFDM scheme as many other conventional modulations are. This allows well-established receiver design and performance analysis techniques for precoded OFDM to be applied to OTFS.

3. Adaptive transmission over fast fading channels

Based on the relationship between output SNR and channel matrix, an adaptive transmission scheme is proposed to optimise the system performance with the knowledge of CSI. This scheme extracts the characteristics in CSI as the precoding matrix to achieve a better performance compared with that of OTFS. It also simplifies the evaluation of output SNR and enables the performance bound analysis. Even with imperfect channel estimation, the adaptive transmission still outperforms OTFS under the same MMSE equalisation. This method also achieves significant improvement over conventional

OFDM and SC-FDE, which use shorter transmission frames than those of OTFS. Closed-form lower and upper performance bounds are derived for the adaptive transmission to show the theoretical limits of the MMSE equalisation over fast fading channels. These bounds provide guidelines for transmission system design and also set up the benchmarks for OTFS system performance evaluation.

4. Low-overhead time and frequency domain channel estimation schemes for OTFS variants

Three OTFS variants that modulate data information directly in frequency or time domain with DFT or IDFT precoding are proposed. They allow 1D frequency or time domain channel estimation to be adopted instead of 2D delay-Doppler domain channel estimation. It is demonstrated that, with the proposed frequency or time domain precoding, the same diversity performance as that of the original OTFS can be achieved over fast fading channels. Theoretical closed-form MSE expressions are also derived for the proposed frequency or time domain channel estimation methods respectively for the channel estimation performance evaluation. It is proved that the performance of channel estimation with time domain training sequence depends on the Doppler conditions in addition to SNR. The signalling overhead of the proposed schemes is shown to be much lower than that of the conventional delay-Doppler domain embedded pilot-aided scheme. Considering power efficiency together, FD-PA-OTFS is shown to be the most efficient scheme among the three OTFS variants.

6.2 Future Work

With the advance of communication technologies, the following research directions may be the focus for the future work.

6.2.1 Extension to MIMO Systems

The next generation wireless communication systems require much higher throughput and reliability than conventional communication systems. As the high-mobility channel is a typical application scenario in the future, achieving high data capacity under large Doppler frequency shifts will be a great challenge. Recently massive MIMO systems based on large antenna arrays have been proposed to improve the spectrum and energy efficiency in multi-user wireless systems [114]. Although the equalisation and channel estimation techniques proposed in this thesis have been proved to achieve low complexity and overhead in SISO systems, the performance in the MIMO systems still needs to be further verified. Meanwhile, there are more challenges, including inter Doppler interference (IDI), inter antenna interference (IAI), and precoding process, when applying SISO techniques to MIMO system. Therefore, it is necessary to design high-efficient and low-complexity algorithms in MIMO systems over fast fading channels.

6.2.2 Application in Joint Radar Communication (JRC)

Aimed at improving power and spectral efficiency and reducing hardware costs, radar sensing and communication have shown closer connections than before [115]. Since OTFS operates on the delay-Doppler domain, which is also important in radar signal processing, the potential relationship between OTFS and JRC has attracted more and more research attention. A JRC system shares the same tasks of estimating the delay and Doppler frequency shift for target, range, and velocity detection as an OTFS system does for communication [116]. Meanwhile, the JRC system also suffers from the high PAPR and ICI problems caused by the conventional OFDM waveform. Some researchers are starting to verify the feasibility to adopt OTFS in JRC systems but how to balance the complexity and performance is still very challenging [116–120]. Therefore, how to exploit and extend the advantages of OTFS in delay and Doppler domains to JRC still

requires significant efforts.

6.2.3 Further System Complexity Reduction

Next generation wireless network requires higher signal processing capability to satisfy the large amount of data throughput in real time. For tens of Gbps digital modem implemented in network devices, the sampling rate can be in order of Gbps for each band and/or multiple simultaneously occupied bands [121]. Considering the symbol length of OTFS is much longer than conventional modulations, even the linear equalisation such as MMSE can impose a large computational complexity to the practical system due to the matrix inversion. Therefore, further technical development on lower complexity equaliser is needed to achieve the real-time OTFS operation in practice.

BIBLIOGRAPHY

[1] A. Dogra, R. K. Jha, and S. Jain, "A survey on beyond 5G network with the advent of 6G: Architecture and emerging technologies," *IEEE Access*, vol. 9, pp. 67512–67547, 2021.

[2] A. F. M. Shahen Shah, "A survey from 1G to 5G including the advent of 6G: Architectures, multiple access techniques, and emerging technologies," in *2022 IEEE 12th Annual Computing and Communication Workshop and Conference (CCWC)*, pp. 1117–1123, 2022.

[3] S. Yang and L. Hanzo, "Fifty years of MIMO detection: The road to large-scale MIMOs," *IEEE Communications Surveys and Tutorials*, vol. 17, no. 4, pp. 1941–1988, 2015.

[4] J. G. Andrews, S. Buzzi, W. Choi, S. V. Hanly, A. Lozano, A. C. K. Soong, and J. C. Zhang, "What will 5G be?," *IEEE Journal on Selected Areas in Communications*, vol. 32, no. 6, pp. 1065–1082, 2014.

[5] M. Agiwal, A. Roy, and N. Saxena, "Next generation 5G wireless networks: A comprehensive survey," *IEEE Communications Surveys Tutorials*, vol. 18, no. 3, pp. 1617–1655, 2016.

[6] W. Saad, M. Bennis, and M. Chen, "A vision of 6G wireless systems: Applications, trends, technologies, and open research problems," *IEEE Network*, vol. 34, no. 3, pp. 134–142, 2020.

[7] T. S. Rappaport, Y. Xing, O. Kanhere, S. Ju, A. Madanayake, S. Mandal, A. Alkhateeb, and G. C. Trichopoulos, "Wireless communications and applications above 100 GHz: Opportunities and challenges for 6G and beyond," *IEEE Access*, vol. 7, pp. 78729–78757, 2019.

[8] Z. Zhang, Y. Xiao, Z. Ma, M. Xiao, Z. Ding, X. Lei, G. K. Karagiannidis, and P. Fan, "6G wireless networks: Vision, requirements, architecture, and key technologies," *IEEE Vehicular Technology Magazine*, vol. 14, no. 3, pp. 28–41, 2019.

[9] A. Gupta and R. K. Jha, "A survey of 5G network: Architecture and emerging technologies," *IEEE Access*, vol. 3, pp. 1206–1232, 2015.

[10] P. Popovski, K. F. Trillingsgaard, O. Simeone, and G. Durisi, "5G wireless network slicing for eMBB, URLLC, and mMTC: A communication-theoretic view," *IEEE Access*, vol. 6, pp. 55765–55779, 2018.

[11] G. A. Akpakwu, B. J. Silva, G. P. Hancke, and A. M. Abu-Mahfouz, "A survey on 5G networks for the internet of things: Communication technologies and challenges," *IEEE Access*, vol. 6, pp. 3619–3647, 2018.

[12] M. Erel-Ozcevik and B. Canberk, "Road to 5G reduced-latency: A software defined handover model for eMBB services," *IEEE Transactions on Vehicular Technology*, vol. 68, no. 8, pp. 8133–8144, 2019.

[13] A. A. Esswie and K. I. Pedersen, "Opportunistic spatial preemptive scheduling for URLLC and eMBB coexistence in multi-user 5G networks," *IEEE Access*, vol. 6, pp. 38451–38463, 2018.

[14] X. Zhang, Y. Niu, S. Mao, Y. Cai, R. He, B. Ai, Z. Zhong, and Y. Liu, "Resource allocation for millimeter-wave train-ground communications in high-speed

railway scenarios," *IEEE Transactions on Vehicular Technology*, vol. 70, no. 5, pp. 4823–4838, 2021.

[15] B. Ai, X. Cheng, T. Kurner, Z.-D. Zhong, K. Guan, R.-S. He, L. Xiong, D. W. Matolak, D. G. Michelson, and C. Briso-Rodriguez, "Challenges toward wireless communications for high-speed railway," *IEEE Transactions on Intelligent Transportation Systems*, vol. 15, no. 5, pp. 2143–2158, 2014.

[16] G. Karagiannis, O. Altintas, E. Ekici, G. Heijenk, B. Jarupan, K. Lin, and T. Weil, "Vehicular networking: A survey and tutorial on requirements, architectures, challenges, standards and solutions," *IEEE Communications Surveys and Tutorials*, vol. 13, no. 4, pp. 584–616, 2011.

[17] C. Tunc and S. S. Panwar, "Mitigating the impact of blockages in millimeter-wave vehicular networks through vehicular relays," *IEEE Open Journal of Intelligent Transportation Systems*, vol. 2, pp. 225–239, 2021.

[18] C. Liu, K. T. Chau, D. Wu, and S. Gao, "Opportunities and challenges of vehicle-to-home, vehicle-to-vehicle, and vehicle-to-grid technologies," *Proceedings of the IEEE*, vol. 101, no. 11, pp. 2409–2427, 2013.

[19] S. Chen, J. Hu, Y. Shi, Y. Peng, J. Fang, R. Zhao, and L. Zhao, "Vehicle-to-everything (v2x) services supported by lte-based systems and 5G," *IEEE Communications Standards Magazine*, vol. 1, no. 2, pp. 70–76, 2017.

[20] C. Bockelmann, N. Pratas, H. Nikopour, K. Au, T. Svensson, C. Stefanovic, P. Popovski, and A. Dekorsy, "Massive machine-type communications in 5G: physical and mac-layer solutions," *IEEE Communications Magazine*, vol. 54, no. 9, pp. 59–65, 2016.

[21] X. Chen, D. W. K. Ng, W. Yu, E. G. Larsson, N. Al-Dhahir, and R. Schober, "Massive access for 5G and beyond," *IEEE Journal on Selected Areas in Communications*, vol. 39, no. 3, pp. 615–637, 2021.

[22] J. Wang, J. Liu, and N. Kato, "Networking and communications in autonomous driving: A survey," *IEEE Communications Surveys Tutorials*, vol. 21, no. 2, pp. 1243–1274, 2019.

[23] F. Jameel, S. Wyne, S. J. Nawaz, and Z. Chang, "Propagation channels for mmWave vehicular communications: State-of-the-art and future research directions," *IEEE Wireless Communications*, vol. 26, no. 1, pp. 144–150, 2019.

[24] D. Jiang and L. Delgrossi, "IEEE 802.11p: Towards an international standard for wireless access in vehicular environments," in *VTC Spring 2008 - IEEE Vehicular Technology Conference*, pp. 2036–2040, 2008.

[25] K. Chelli and T. Herfet, "Doppler shift compensation in vehicular communication systems," in *2016 2nd IEEE International Conference on Computer and Communications (ICCC)*, pp. 2188–2192, 2016.

[26] N. Lu, N. Cheng, N. Zhang, X. Shen, and J. W. Mark, "Connected vehicles: Solutions and challenges," *IEEE Internet of Things Journal*, vol. 1, no. 4, pp. 289–299, 2014.

[27] A. Tassi, M. Egan, R. J. Piechocki, and A. Nix, "Modeling and design of millimeter-wave networks for highway vehicular communication," *IEEE Transactions on Vehicular Technology*, vol. 66, no. 12, pp. 10676–10691, 2017.

[28] D. Ghozlani, A. Omri, S. Bouallegue, H. Chamkhia, and R. Bouallegue, "Stochastic geometry-based analysis of joint radar and communication-enabled cooperative detection systems," in *2021 17th International Conference on Wireless and*

Mobile Computing, Networking and Communications (WiMob), pp. 325–330, 2021.

[29] J. Fang, Y. Xiang, Y. Huang, Y. Cui, and W. Wang, "A vehicle control model to alleviate traffic instability," *IEEE Transactions on Vehicular Technology*, vol. 70, no. 10, pp. 9863–9876, 2021.

[30] B. Zhao, C. Fei, X. Mao, W. Yu, and C. Wu, "Networking in space terrestrial integrated networks," in *2019 18th International Conference on Optical Communications and Networks (ICOCN)*, pp. 1–3, 2019.

[31] A. Behnaam, *et al*, "Key drivers and research challenges for 6G ubiquitous wireless intelligence (white paper)," in *First 6G Wireless Summit*, September 2019. Available at `http://jultika.oulu.fi/files/isbn9789526223544.pdf`.

[32] X. Huang, J. A. Zhang, R. P. Liu, Y. J. Guo, and L. Hanzo, "Airplane-aided integrated networking for 6G wireless: Will it work?," *IEEE Vehicular Technology Magazine*, vol. 14, pp. 84–91, Sep. 2019.

[33] J. Liu, Y. Shi, Z. M. Fadlullah, and N. Kato, "Space-air-ground integrated network: A survey," *IEEE Communications Surveys Tutorials*, vol. 20, pp. 2714–2741, Fourthquarter 2018.

[34] Y. Pei, S. Miao, and F. Li, "Challenges and opportunities for terrestrial network operators in the air-space-ground integrated network," in *2020 IEEE Intl Conf on Parallel Distributed Processing with Applications, Big Data Cloud Computing, Sustainable Computing Communications, Social Computing Networking (ISPA/BDCloud/SocialCom/SustainCom)*, pp. 1400–1404, 2020.

[35] Y. Bi, G. Han, S. Xu, X. Wang, C. Lin, Z. Yu, and P. Sun, "Software defined space-terrestrial integrated networks: Architecture, challenges, and solutions," *IEEE Network*, vol. 33, no. 1, pp. 22–28, 2019.

[36] M. Shafi, A. F. Molisch, P. J. Smith, T. Haustein, P. Zhu, P. De Silva, F. Tufvesson, A. Benjebbour, and G. Wunder, "5G: A tutorial overview of standards, trials, challenges, deployment, and practice," *IEEE Journal on Selected Areas in Communications*, vol. 35, no. 6, pp. 1201–1221, 2017.

[37] H. Tataria, M. Shafi, A. F. Molisch, M. Dohler, H. Sjoland, and F. Tufvesson, "6G wireless systems: Vision, requirements, challenges, insights, and opportunities," *Proceedings of the IEEE*, vol. 109, no. 7, pp. 1166–1199, 2021.

[38] R. Hadani, S. Rakib, M. Tsatsanis, A. Monk, A. J. Goldsmith, A. F. Molisch, and R. Calderbank, "Orthogonal time frequency space modulation," in *2017 IEEE Wireless Communications and Networking Conference (WCNC)*, pp. 1–6, March 2017.

[39] P. Cheng, Z. Chen, Y. Rui, Y. J. Guo, L. Gui, M. Tao, and Q. T. Zhang, "Channel estimation for ofdm systems over doubly selective channels: A distributed compressive sensing based approach," *IEEE Transactions on Communications*, vol. 61, pp. 4173–4185, October 2013.

[40] K. Xu, Z. Shen, Y. Wang, and X. Xia, "Location-aided mMIMO channel tracking and hybrid beamforming for high-speed railway communications: An angle-domain approach," *IEEE Systems Journal*, vol. 14, no. 1, pp. 93–104, 2020.

[41] X. Ma, F. Yang, S. Liu, W. Ding, and J. Song, "Structured compressive sensing-based channel estimation for time frequency training OFDM systems over doubly selective channel," *IEEE Wireless Communications Letters*, vol. 6, no. 2, pp. 266–269, 2017.

[42] W. Yuan, N. Wu, H. Wang, and J. Kuang, "Variational inference-based frequency-domain equalization for faster-than-nyquist signaling in doubly selective channels," *IEEE Signal Processing Letters*, vol. 23, no. 9, pp. 1270–1274, 2016.

[43] L. Zhang, Z. Hong, L. Thibault, R. Boudreau, and Y. Wu, "A low-complexity robust ofdm receiver for fast fading channels," *IEEE Transactions on Broadcasting*, vol. 60, pp. 347–357, June 2014.

[44] H. Abdzadeh-Ziabari, W.-P. Zhu, and M. N. S. Swamy, "Joint carrier frequency offset and doubly selective channel estimation for MIMO-OFDMA uplink with kalman and particle filtering," *IEEE Transactions on Signal Processing*, vol. 66, no. 15, pp. 4001–4012, 2018.

[45] T. Jiang and Y. Wu, "An overview: Peak-to-average power ratio reduction techniques for OFDM signals," *IEEE Transactions on Broadcasting*, vol. 54, no. 2, pp. 257–268, 2008.

[46] Y. Rahmatallah and S. Mohan, "Peak-to-average power ratio reduction in OFDM systems: A survey and taxonomy," *IEEE Communications Surveys Tutorials*, vol. 15, no. 4, pp. 1567–1592, 2013.

[47] G. Fettweis, M. Krondorf, and S. Bittner, "GFDM - generalized frequency division multiplexing," in *VTC Spring 2009 - IEEE 69th Vehicular Technology Conference*, pp. 1–4, 2009.

[48] D. Na and K. Choi, "Low PAPR FBMC," *IEEE Transactions on Wireless Communications*, vol. 17, no. 1, pp. 182–193, 2018.

[49] A. M. Jaradat, J. M. Hamamreh, and H. Arslan, "Modulation options for OFDM-based waveforms: Classification, comparison, and future directions," *IEEE Access*, vol. 7, pp. 17263–17278, 2019.

[50] D. Falconer, S. Ariyavisitakul, A. Benyamin-Seeyar, and B. Eidson, "Frequency domain equalization for single-carrier broadband wireless systems," *IEEE Communications Magazine*, vol. 40, no. 4, pp. 58–66, 2002.

[51] X. Zhang, E. Chen, and X. Mu, "Single-carrier frequency-domain equalization based on frequency-domain oversampling," *IEEE Communications Letters*, vol. 16, no. 1, pp. 24–26, 2012.

[52] H. G. Myung, J. Lim, and D. J. Goodman, "Peak-to-average power ratio of single carrier fdma signals with pulse shaping," in *2006 IEEE 17th International Symposium on Personal, Indoor and Mobile Radio Communications*, pp. 1–5, 2006.

[53] P. Raviteja, K. T. Phan, Y. Hong, and E. Viterbo, "Interference cancellation and iterative detection for orthogonal time frequency space modulation," *IEEE Transactions on Wireless Communications*, vol. 17, pp. 6501–6515, Oct 2018.

[54] P. Raviteja, K. T. Phan, Q. Jin, Y. Hong, and E. Viterbo, "Low-complexity iterative detection for orthogonal time frequency space modulation," in *2018 IEEE Wireless Communications and Networking Conference (WCNC)*, (Barcelona, Spain), April 2018.

[55] P. Raviteja, Y. Hong, E. Viterbo, and E. Biglieri, "Practical pulse-shaping waveforms for reduced-cyclic-prefix OTFS," *IEEE Transactions on Vehicular Technology*, vol. 68, pp. 957–961, Jan 2019.

[56] V. Khammammetti and S. K. Mohammed, "OTFS-based multiple-access in high Doppler and delay spread wireless channels," *IEEE Wireless Communications Letters*, vol. 8, pp. 528–531, April 2019.

[57] B. Li, S. Zhou, M. Stojanovic, L. Freitag, and P. Willett, "Multicarrier communication over underwater acoustic channels with nonuniform doppler shifts," *IEEE Journal of Oceanic Engineering*, vol. 33, no. 2, pp. 198–209, 2008.

[58] B. S. Sharif, J. Neasham, O. R. Hinton, and A. E. Adams, "A computationally efficient Doppler compensation system for underwater acoustic communications," *IEEE Journal of Oceanic Engineering*, vol. 25, pp. 52–61, Jan 2000.

[59] M. Morelli and U. Mengali, "An improved frequency offset estimator for OFDM applications," *IEEE Communications Letters*, vol. 3, no. 3, pp. 75–77, 1999.

[60] L. Cheng, B. E. Henty, D. D. Stancil, F. Bai, and P. Mudalige, "Mobile vehicle-to-vehicle narrow-band channel measurement and characterization of the 5.9 GHz dedicated short range communication (DSRC) frequency band," *IEEE Journal on Selected Areas in Communications*, vol. 25, no. 8, pp. 1501–1516, 2007.

[61] S. Daoud and A. Ghrayeb, "Using resampling to combat Doppler scaling in UWA channels with single-carrier modulation and frequency-domain equalization," *IEEE Transactions on Vehicular Technology*, vol. 65, pp. 1261–1270, March 2016.

[62] C. F. Mecklenbrauker, A. F. Molisch, J. Karedal, F. Tufvesson, A. Paier, L. Bernado, T. Zemen, O. Klemp, and N. Czink, "Vehicular channel characterization and its implications for wireless system design and performance," *Proceedings of the IEEE*, vol. 99, no. 7, pp. 1189–1212, 2011.

[63] D. Cox, "Delay Doppler characteristics of multipath propagation at 910 MHz in a suburban mobile radio environment," *IEEE Transactions on Antennas and Propagation*, vol. 20, no. 5, pp. 625–635, 1972.

[64] B. Li, Z. Fei, and Y. Zhang, "UAV communications for 5G and beyond: Recent advances and future trends," *IEEE Internet of Things Journal*, vol. 6, no. 2, pp. 2241–2263, 2019.

[65] J. Wu and P. Fan, "A survey on high mobility wireless communications: Challenges, opportunities and solutions," *IEEE Access*, vol. 4, pp. 450–476, 2016.

[66] C.-X. Wang, F. Haider, X. Gao, X.-H. You, Y. Yang, D. Yuan, H. M. Aggoune, H. Haas, S. Fletcher, and E. Hepsaydir, "Cellular architecture and key technologies for 5G wireless communication networks," *IEEE Communications Magazine*, vol. 52, no. 2, pp. 122–130, 2014.

[67] S. Tiwari, S. S. Das, and V. Rangamgari, "Low complexity LMMSE receiver for OTFS," *IEEE Communications Letters*, vol. 23, no. 12, pp. 2205–2209, 2019.

[68] G. D. Surabhi, R. M. Augustine, and A. Chockalingam, "On the diversity of uncoded OTFS modulation in doubly-dispersive channels," *IEEE Transactions on Wireless Communications*, vol. 18, pp. 3049–3063, June 2019.

[69] P. Raviteja, E. Viterbo, and Y. Hong, "OTFS performance on static multipath channels," *IEEE Wireless Communications Letters*, vol. 8, pp. 745–748, June 2019.

[70] E. Biglieri, P. Raviteja, and Y. Hong, "Error performance of orthogonal time frequency space (OTFS) modulation," in *2019 IEEE International Conference on Communications Workshops (ICC Workshops)*, (Shanghai, China), May 2019.

[71] S. Ahmed, M. Sellathurai, S. Lambotharan, and J. A. Chambers, "Low-complexity iterative method of equalization for single carrier with cyclic prefix in doubly selective channels," *IEEE Signal Processing Letters*, vol. 13, pp. 5–8, Jan 2006.

[72] F. Hlawatsch and G. Matz, *Wireless Communications Over Rapidly Time-Varying Channels*. Orlando, FL, USA: Academic Press, Inc., 1st ed., 2011.

[73] ETSI, "Study on channel model for frequencies from 0.5 to 100 GHz," *ETSI TR 138 901 V15.0.0*, July 2018.

[74] H. Zhang, X. Huang, and J. A. Zhang, "Comparison of OTFS diversity performance over slow and fast fading channels," in *2019 IEEE/CIC International Conference on Communications in China (ICCC)*, pp. 828–833, Aug 2019.

[75] L. Dai, Z. Wang, and Z. Yang, "Time-frequency training OFDM with high spectral efficiency and reliable performance in high speed environments," *IEEE Journal on Selected Areas in Communications*, vol. 30, no. 4, pp. 695–707, 2012.

[76] Y. Zhou, Z. Pan, J. Hu, J. Shi, and X. Mo, "Broadband wireless communications on high speed trains," in *2011 20th Annual Wireless and Optical Communications Conference (WOCC)*, pp. 1–6, 2011.

[77] Yuping Zhao and S. . Haggman, "Intercarrier interference self-cancellation scheme for OFDM mobile communication systems," *IEEE Transactions on Communications*, vol. 49, pp. 1185–1191, July 2001.

[78] K. Lin, H. Lin, and M. Tseng, "An equivalent channel time variation mitigation scheme for ICI reduction in high-mobility OFDM systems," *IEEE Transactions on Broadcasting*, vol. 58, pp. 472–479, Sep. 2012.

[79] X. Gao, L. Dai, Y. Zhang, T. Xie, X. Dai, and Z. Wang, "Fast channel tracking for terahertz beamspace massive MIMO systems," *IEEE Transactions on Vehicular Technology*, vol. 66, pp. 5689–5696, July 2017.

[80] W. Wang and S. S. Abeysekera, "Data aided phase tracking and symbol detection for CPM in frequency-flat fading channel," in *2011 IEEE International Conference*

on Acoustics, Speech and Signal Processing (ICASSP), pp. 3500–3503, May 2011.

[81] S. Stefanatos and A. K. Katsaggelos, "Joint data detection and channel tracking for OFDM systems with phase noise," *IEEE Transactions on Signal Processing*, vol. 56, pp. 4230–4243, Sep. 2008.

[82] H. Nguyen-Le and T. Le-Ngoc, "Pilot-aided joint CFO and doubly-selective channel estimation for OFDM transmissions," *IEEE Transactions on Broadcasting*, vol. 56, pp. 514–522, Dec 2010.

[83] H. Nguyen-Le, T. Le-Ngoc, and N. H. Tran, "Iterative receiver design with joint doubly selective channel and CFO estimation for coded MIMO-OFDM transmissions," *IEEE Transactions on Vehicular Technology*, vol. 60, pp. 4052–4057, Oct 2011.

[84] W. Chin, "Nondata-aided Doppler frequency estimation for OFDM systems over doubly selective fading channels," *IEEE Transactions on Communications*, vol. 66, pp. 4211–4221, Sep. 2018.

[85] E. P. Simon and M. A. Khalighi, "Iterative soft-Kalman channel estimation for fast time-varying MIMO-OFDM channels," *IEEE Wireless Communications Letters*, vol. 2, pp. 599–602, December 2013.

[86] R. Hadani, S. Rakib, A. F. Molisch, C. Ibars, A. Monk, M. Tsatsanis, J. Delfeld, A. Goldsmith, and R. Calderbank, "Orthogonal time frequency space (OTFS) modulation for millimeter-wave communications systems," in *2017 IEEE MTT-S International Microwave Symposium (IMS)*, pp. 681–683, 2017.

[87] F. Wiffen, L. Sayer, M. Z. Bocus, A. Doufexi, and A. Nix, "Comparison of OTFS and OFDM in ray launched sub-6 GHz and mmWave line-of-sight mobility

channels," in *2018 IEEE 29th Annual International Symposium on Personal, Indoor and Mobile Radio Communications (PIMRC)*, pp. 73–79, Sep. 2018.

[88] A. Farhang, A. RezazadehReyhani, L. E. Doyle, and B. Farhang-Boroujeny, "Low complexity modem structure for OFDM-based orthogonal time frequency space modulation," *IEEE Wireless Communications Letters*, vol. 7, pp. 344–347, June 2018.

[89] A. RezazadehReyhani, A. Farhang, M. Ji, R. R. Chen, and B. Farhang-Boroujeny, "Analysis of discrete-time MIMO OFDM-based orthogonal time frequency space modulation," in *2018 IEEE International Conference on Communications (ICC)*, pp. 1–6, May 2018.

[90] P. Raviteja, Y. Hong, E. Viterbo, and E. Biglieri, "Effective diversity of OTFS modulation," *IEEE Wireless Communications Letters*, vol. 9, pp. 249–253, Feb 2020.

[91] P. Raviteja, K. T. Phan, and Y. Hong, "Embedded pilot-aided channel estimation for OTFS in Delay Doppler channels," *IEEE Transactions on Vehicular Technology*, vol. 68, no. 5, pp. 4906–4917, 2019.

[92] W. Shen, L. Dai, S. Han, I. Chih-Lin, and R. W. Heath, "Channel estimation for orthogonal time frequency space (OTFS) massive MIMO," in *ICC 2019 - 2019 IEEE International Conference on Communications (ICC)*, pp. 1–6, 2019.

[93] W. Shen, L. Dai, J. An, P. Fan, and R. W. Heath, "Channel estimation for orthogonal time frequency space (OTFS) massive MIMO," *IEEE Transactions on Signal Processing*, vol. 67, no. 16, pp. 4204–4217, 2019.

[94] K. R. Murali and A. Chockalingam, "On OTFS modulation for high-Doppler fading channels," in *2018 Information Theory and Applications Workshop (ITA)*, pp. 1–10, 2018.

[95] F. Long, K. Niu, C. Dong, and J. Lin, "Low complexity iterative LMMSE-PIC equalizer for OTFS," in *ICC 2019 - 2019 IEEE International Conference on Communications (ICC)*, pp. 1–6, May 2019.

[96] Xiaojing Huang, "Diversity performance of precoded OFDM with MMSE equalization," in *2007 International Symposium on Communications and Information Technologies*, pp. 802–807, Oct 2007.

[97] R. Ran and T. Huang, "An inversion algorithm for a banded matrix," *Computers and Mathematics with Applications*, vol. 58, no. 9, pp. 1699–1710, 2009.

[98] T. Thaj and E. Viterbo, "Low complexity iterative rake decision feedback equalizer for zero-padded OTFS systems," *IEEE Transactions on Vehicular Technology*, vol. 69, no. 12, pp. 15606–15622, 2020.

[99] X. Huang, "Multipath diversity of precoded OFDM with linear equalization," in *2008 IEEE International Conference on Communications*, pp. 1307–1311, May 2008.

[100] J. Proakis and M. Salehi, *Digital Communications*. McGraw-Hill, 5th ed.

[101] F. Hlawatsch and G. Matz, *Wireless communications over rapidly time-varying channels*. Academic Press, 2011.

[102] H. Bishi, S. H. Alshepane, K. F. Alhaddar, and S. E. Alnour, "Investigation and study of the performance of a DVB over satellite link using m-ary PSK," in *2022 IEEE 2nd International Maghreb Meeting of the Conference on Sciences*

and Techniques of Automatic Control and Computer Engineering (MI-STA), pp. 335–339, 2022.

[103] M. A. F. Chakiki, I. G. P. Astawa, and A. Budikarso, "Performance analysis of DVB-T2 system based on MIMO using low density parity check (LDPC) code technique and maximum likelihood (ML) detection," in *2020 International Electronics Symposium (IES)*, pp. 169–173, 2020.

[104] A. Gunturu, A. R. Godala, A. K. Sahoo, and A. K. R. Chavva, "Performance analysis of OTFS waveform for 5G NR mmWave communication system," in *2021 IEEE Wireless Communications and Networking Conference (WCNC)*, pp. 1–6, 2021.

[105] T. Blazek and D. Radovic, "Performance evaluation of OTFS over measured V2V channels at 60 GHz," in *2020 IEEE MTT-S International Conference on Microwaves for Intelligent Mobility (ICMIM)*, pp. 1–4, 2020.

[106] X. Feng, H. Esmaiel, J. Wang, J. Qi, M. Zhou, Z. A. H. Qasem, H. Sun, and Y. Gu, "Underwater acoustic communications based on OTFS," in *2020 15th IEEE International Conference on Signal Processing (ICSP)*, vol. 1, pp. 439–444, 2020.

[107] C. Liu, S. Liu, Z. Mao, Y. Huang, and H. Wang, "Low-complexity parameter learning for OTFS modulation based automotive radar," in *ICASSP 2021 - 2021 IEEE International Conference on Acoustics, Speech and Signal Processing (ICASSP)*, pp. 8208–8212, 2021.

[108] A. Grover, "ML and MMSE equalizers in frequency selective and flat fading channels," in *2013 1st International Conference on Artificial Intelligence, Modelling and Simulation*, pp. 413–415, 2013.

[109] S. Sharma, K. Deka, and B. BeferullLozano, "Low-complexity detection for uplink massive MIMO SCMA systems," *IET Communications*, no. 15(1), pp. 51–59, 2020.

[110] L. Zhao, W. Gao, and W. Guo, "Sparse Bayesian learning of Delay-Doppler channel for OTFS system," *IEEE Communications Letters*, vol. 24, no. 12, pp. 2766–2769, 2020.

[111] H. Qu, G. Liu, L. Zhang, M. A. Imran, and S. Wen, "Low-dimensional subspace estimation of continuous-Doppler-spread channel in OTFS systems," *IEEE Transactions on Communications*, pp. 1–1, 2021.

[112] *Study LTE-Based V2X Services*. Document TR 36.885 (V14.0.0) Release 14, 3GPP, 2016.

[113] H. Zhang, X. Huang, and J. A. Zhang, "Adaptive transmission with frequency-domain precoding and linear equalization over fast fading channels," *IEEE Transactions on Wireless Communications*, vol. 20, no. 11, pp. 7420–7430, 2021.

[114] B. C. Pandey, S. K. Mohammed, P. Raviteja, Y. Hong, and E. Viterbo, "Low complexity precoding and detection in multi-user massive MIMO OTFS downlink," *IEEE Transactions on Vehicular Technology*, vol. 70, no. 5, pp. 4389–4405, 2021.

[115] L. Gaudio, M. Kobayashi, G. Caire, and G. Colavolpe, "On the effectiveness of OTFS for joint radar parameter estimation and communication," *IEEE Transactions on Wireless Communications*, vol. 19, no. 9, pp. 5951–5965, 2020.

[116] A. S. Bondre and C. D. Richmond, "Dual-use of OTFS architecture for pulse Doppler radar processing," in *2022 IEEE Radar Conference (RadarConf22)*, pp. 1–6, 2022.

[117] P. Raviteja, K. T. Phan, Y. Hong, and E. Viterbo, "Orthogonal time frequency space (OTFS) modulation based radar system," in *2019 IEEE Radar Conference (RadarConf)*, pp. 1–6, 2019.

[118] M. F. Keskin, H. Wymeersch, and A. Alvarado, "Radar sensing with OTFS: Embracing ISI and ICI to surpass the ambiguity barrier," in *2021 IEEE International Conference on Communications Workshops (ICC Workshops)*, pp. 1–6, 2021.

[119] H. Zhang, T. Zhang, and Y. Shen, "Modulation symbol cancellation for OTFS-based joint radar and communication," in *2021 IEEE International Conference on Communications Workshops (ICC Workshops)*, pp. 1–6, 2021.

[120] L. Gaudio, M. Kobayashi, G. Caire, and G. Colavolpe, "Joint radar target detection and parameter estimation with MIMO OTFS," in *2020 IEEE Radar Conference (RadarConf20)*, pp. 1–6, 2020.

[121] H. Zhang, X. Huang, T. Zhang, J. A. Zhang, and Y. Jay Guo, "A 30 Gbps low-complexity and real-time digital modem for wireless communications at 0.325 THz," in *2019 19th International Symposium on Communications and Information Technologies (ISCIT)*, pp. 260–264, 2019.

Appendix A

Let us consider the number of complex multiplications and/or divisions involved in calculating the inverse of an $MN \times MN$ circular stripe diagonal matrix with stripe width $1+2k$. Using the Gaussian elimination method, the inversion can be carried out as follows.

(1) Let's start with the initial footprint of the circular stripe diagonal matrix as shown on the left side of Fig. 1. For the first row, all the elements are divided in the row by the first element and cancel the first elements of the other $2k$ rows with non-zero first elements respectively, which has complexity of $(1+2k)$ (divisions) + $2k(1+2k)$ (multiplications). This process is repeated from the first to $(MN-2k)$-th rows.

(2) For the last $2k$ rows, the complexity for cancelling all non-zero elements can be expressed as $(2k)^2+(2k-1)^2+...+1$ to obtain an upper-triangular matrix with footprint as shown on the right side of Fig. 1.

(3) Let's then continue to perform the back substitution to turn the upper-triangular matrix to a diagonal matrix. For the first k columns, the complexity can be expressed as $(MN-1)+(MN-2)+...+(MN-k)$.

(4) For the $(k+1)$-th to $(MN-k)$-th columns, the complexity can be expressed as $k(MN-2k)$.

(5) For the last k columns, the complexity can be expressed as $(k-1)+(k-2)+...+1$.

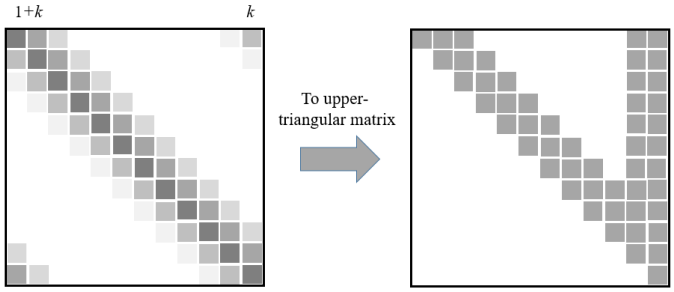

Figure 1: Illustration of Gaussian elimination.

The total computational complexity of matrix inversion is

$$\begin{aligned} C_{total} &= (1+2k)^2(MN-2k) + \sum_{n=1}^{2k} n^2 + \sum_{n=1}^{k}(MN-n) + k(MN-2k) + \sum_{n=1}^{2k} n^2 \\ &= (1+2k)^2(MN-2k) + \frac{1}{6}2k(2k+1)(4k+1) + 2kMN - 2k^2 - k, \end{aligned} \tag{1}$$

which has the complexity of $O((1+2k)^2MN)$ approximately. In this thesis, the matrix $\mathbf{H}_v$ has a stripe width of $1+2\times K_{max}$, and hence the matrix $(\mathbf{H}_v\mathbf{H}_v^{\mathbf{H}} + (1/\gamma_{in})\mathbf{I})$ has a stripe width of $1+4\times K_{max}$. Therefore, the complexity of the frequency domain MMSE equalisation is $O((1+4K_{max})^2MN)$.

Appendix B

From (2.1) and (2.4), the received signal can be expressed as

$$r(t) = \int_{-\infty}^{+\infty} h_t(\tau,t)s(t-\tau)d\tau + w(t). \tag{2}$$

In the discrete-time domain, it becomes

$$r[i] = \sum_{j=-\infty}^{+\infty} h_t[j,i]s[i-j] + w[i], \tag{3}$$

where $h_t[j,i]$ and $w[i]$ are the discrete-time versions of the delay-time channel representation $h_t(\tau,t)$ and noise $w(t)$, respectively, sampled at $t = id_r$ and $\tau = jd_r$. It is assumed that the transmitted data symbols $s[0], s[1], ..., s[MN-1]$ are independent with equal

power σ_s^2 and the noise power is σ_w^2. After OTFS demodulation, i.e., Wigner transform followed by SFFT, the $(m'M+m)$-th recovered signal can be expressed as

$$y[m'M+m] = \sum_{n=0}^{N-1} r[nM+m] e^{-\mathbf{j}\frac{2\pi}{N}nm'}, \tag{4}$$

for $m' = 0,...,N-1$, $m = 0,...,M-1$. To calculate the output SNR, the power of $y[m'M+m]$ can be expressed as

$$\begin{aligned}
&\mathbf{E}\{|y[m'M+m]|^2\} \\
&= \mathbf{E}\{\sum_{n=0}^{N-1} r[nM+m] e^{-\mathbf{j}\frac{2\pi}{N}nm'} \sum_{n'=0}^{N-1} r^*[n'M+m] e^{\mathbf{j}\frac{2\pi}{N}n'm'}\} \\
&= \sum_{n=0}^{N-1}\sum_{n'=0}^{N-1} \mathbf{E}\{r[nM+m] r^*[n'M+m]\} e^{\mathbf{j}\frac{2\pi}{N}(n'-n)m'},
\end{aligned} \tag{5}$$

where $(\cdot)^*$ denotes the complex conjugation. Supposing that $M > L$ where L is the maximum multipath delay, Eq. (5) can be simplified as

$$\begin{aligned}
&\mathbf{E}\{|y[m'M+m]|^2\} \\
&= \sum_{n=0}^{N-1} \mathbf{E}\{|r[nM+m]|^2\} \\
&= \sum_{n=0}^{N-1}\sum_{l=0}^{L-1} |h_t[l,nM+m]|^2\sigma_s^2 + \sigma_w^2 \\
&= \frac{1}{d_r^2}\sum_{n=0}^{N-1}\sum_{l=0}^{L-1}\sum_{k=-K_{max}}^{K_{max}}\sum_{k'=-K_{max}}^{K_{max}} h[l,k] e^{\mathbf{j}\frac{2\pi}{MN}k(nM+m)} h^*[l,k'] e^{-\mathbf{j}\frac{2\pi}{MN}k'(nM+m)}\sigma_s^2 + \sigma_w^2 \\
&= \frac{N}{d_r^2}\sum_{l=0}^{L-1}\sum_{k=-K_{max}}^{K_{max}} |h[l,k]|^2\sigma_s^2 + \sigma_w^2,
\end{aligned} \tag{6}$$

since $\mathbf{E}\{r[nM+m]r^*[n'M+m]\} = 0$, for $n \neq n'$. In deriving (4.27), it has been assumed that the relationship between $h_t[l,j]$ and $h[l,k]$ is

$$h_t[l,j] = \frac{1}{d_r}\sum_{k=-K_{max}}^{K_{max}} h[l,k] e^{\mathbf{j}\frac{2\pi}{MN}kj} \tag{7}$$

based on Eq. (2.4) and Fig. 2.5.

From (6) and ignoring any scaling factor, the output SNR can be expressed as shown in (4.7).